

RWTH AACHEN UNIVERSITY

MASTER OF SCIENCE IN GEORESOURCES MANAGEMENT

MASTER THESIS

---

# **Bayesian Decision Theory in Structural Geological Modeling**

## **How Reducing Uncertainties Affects Reservoir Value Estimations**

---

November 29, 2017

**Author:**  
Fabian Antonio Stamm

**Examiners:**  
Prof. Florian Wellmann, Ph.D.  
Prof. Dr. Janos Urai

**Supervisor:**  
Miguel de la Varga, M.Sc.

submitted to the  
Institute of Computational Geoscience and Reservoir Engineering

Faculty of Georesources and Material Engineering · RWTH Aachen University

Printed in Aachen, Germany

# Eidesstattliche Versicherung

## Statutory Declaration in Lieu of an Oath

Stamm, Fabian Antonio

---

Name, Vorname/Last Name, First Name

Matrikelnummer (freiwillige Angabe)

Matriculation No. (optional)

Ich versichere hiermit an Eides Statt, dass ich die vorliegende Arbeit/Bachelorarbeit/  
Masterarbeit\* mit dem Titel

I hereby declare in lieu of an oath that I have completed the present paper/Bachelor thesis/Master thesis\* entitled

Bayesian Decision Theory in Structural Geological Modeling - How Reducing Uncertainties Affects Reservoir Value Estimations

---

---

selbstständig und ohne unzulässige fremde Hilfe erbracht habe. Ich habe keine anderen als die angegebenen Quellen und Hilfsmittel benutzt. Für den Fall, dass die Arbeit zusätzlich auf einem Datenträger eingereicht wird, erkläre ich, dass die schriftliche und die elektronische Form vollständig übereinstimmen. Die Arbeit hat in gleicher oder ähnlicher Form noch keiner Prüfungsbehörde vorgelegen.

independently and without illegitimate assistance from third parties. I have used no other than the specified sources and aids. In case that the thesis is additionally submitted in an electronic format, I declare that the written and electronic versions are fully identical. The thesis has not been submitted to any examination body in this, or similar, form.

---

Ort, Datum/City, Date

---

Unterschrift/Signature

\*Nichtzutreffendes bitte streichen

\*Please delete as appropriate

**Belehrung:**

Official Notification:

**§ 156 StGB: Falsche Versicherung an Eides Statt**

Wer vor einer zur Abnahme einer Versicherung an Eides Statt zuständigen Behörde eine solche Versicherung falsch abgibt oder unter Berufung auf eine solche Versicherung falsch aussagt, wird mit Freiheitsstrafe bis zu drei Jahren oder mit Geldstrafe bestraft.

**Para. 156 StGB (German Criminal Code): False Statutory Declarations**

Whoever before a public authority competent to administer statutory declarations falsely makes such a declaration or falsely testifies while referring to such a declaration shall be liable to imprisonment not exceeding three years or a fine.

**§ 161 StGB: Fahrlässiger Falscheid; fahrlässige falsche Versicherung an Eides Statt**

(1) Wenn eine der in den §§ 154 bis 156 bezeichneten Handlungen aus Fahrlässigkeit begangen worden ist, so tritt Freiheitsstrafe bis zu einem Jahr oder Geldstrafe ein.

(2) Straflosigkeit tritt ein, wenn der Täter die falsche Angabe rechtzeitig berichtigt. Die Vorschriften des § 158 Abs. 2 und 3 gelten entsprechend.

**Para. 161 StGB (German Criminal Code): False Statutory Declarations Due to Negligence**

(1) If a person commits one of the offences listed in sections 154 through 156 negligently the penalty shall be imprisonment not exceeding one year or a fine.

(2) The offender shall be exempt from liability if he or she corrects their false testimony in time. The provisions of section 158 (2) and (3) shall apply accordingly.

Die vorstehende Belehrung habe ich zur Kenntnis genommen:

I have read and understood the above official notification:

---

Ort, Datum/City, Date

Unterschrift/Signature



---

## Abstract

Bayesian decision theory is applicable to a wide spectrum of problems. Hydrocarbon exploration and production is a high-risk, high-reward sector in which good decision making is indispensable. Actors in this field are faced by numerous uncertainties that have to be considered. Structural geological modeling is of central importance for the assessment of uncertain hydrocarbon accumulations in potential reservoirs. By regarding such modeling as a Bayesian inference problem, additional geological information can be incorporated as likelihood functions linked to prior parameters in a probabilistic framework. Markov chain Monte Carlo sampling is used to approximate posterior models of reduced uncertainty. Here, synthetic geological models are constructed to represent potential hydrocarbon systems. Algorithms for automatic trap recognition are developed to enable the reservoir valuation of prior and posterior models. These serve as a base for true value estimation by respective optimization of a case-specific loss function. This function is customized to reflect the decision making of differently risk-affine actors. Results from conducting this for several inference cases show that the various Bayes estimators shift according to the characteristics of the underlying value distribution. While bimodality and overall uncertainty leads to separation, risk-averse and risk-friendly decisions converge and decrease in expected loss given narrower unimodal distributions. The degree of decision convergence is considered a measure for the state of knowledge and its inherent uncertainty at the moment of decision making. This decisive uncertainty does not change aligned with model uncertainty but depends on alterations of critical parameters and respective interdependencies, in particular relating to seal reliability. Additionally, actors are affected differently by one set of information, as defined by their risk affinity. For good decision making, it appears to be most important to recognize for which parameters reduction of uncertainty leads to changes in decisions.



---

# Acknowledgements

First and foremost, I wish to express my greatest thanks to Miguel de la Varga, whose outstanding support I have received since he was my tutor in Numerical Reservoir Engineering. He encouraged me to challenge myself and to pursue a path into a research field that, not long ago, was very much unfamiliar to me. I am grateful for the continuous motivation, constant positive feedback and especially the immense patience he showed as my supervisor and mentor.

Furthermore, I want to voice my gratitude to Professor Florian Wellmann, for welcoming me as a part of his research group and thus showing me how exciting and inspiring it can be to participate in a free and forward-thinking academic environment. With his interest, openness and positive attitude, he encouraged me to contribute to his group's work and to develop my own scientific ideas.

I also wish to thank Professor Janos Urai, for years of fascinating lectures on structural geology, hydrocarbon exploration and production, as well as related risk analysis. His courses provided me with many insights and served as sources of inspiration and information that I was able to include in this project.

In general, I am grateful to my friends and fellow researchers from the CGRE group, especially for creating such a pleasant working atmosphere. Special thanks go to the modeling team. To Alexander Schaaf, for helping me with GemPy when Miguel could not be found and reminding me to take a break now and then. To Marco van Veen, for endless inciting and exhilarating discussions, but also for the many shared adventures during our geoscientific studies.

And of course, I owe my deepest gratitude to my family, for a lifetime of unconditional support. To my parents, for raising me to be curious, for enabling me to attain such excellent education and for providing me with the freedom to follow my individual interests and aspirations.



---

# Table of Contents

<b>Abstract</b>	v
<b>Acknowledgements</b>	vii
<b>Acronyms</b>	xix
<b>1 Introduction</b>	1
<b>2 Methods</b>	3
2-1 Bayesian analysis and decision theory . . . . .	3
2-1-1 Basic elements . . . . .	4
2-1-2 Bayesian inference . . . . .	4
2-1-3 Estimation . . . . .	4
2-1-4 Expected loss and loss functions . . . . .	5
2-2 Application in structural geological modeling . . . . .	7
2-2-1 Markov chain Monte Carlo sampling (MCMC) . . . . .	9
2-2-2 Structural geological forward modeling . . . . .	11
2-2-3 Numerical computational implementation . . . . .	12
2-3 Model evaluation . . . . .	13
2-3-1 Visualizing uncertainty . . . . .	14
2-3-2 Economic significance of structural geological models as hydrocarbon systems	16
2-3-3 Original oil-in-place and recoverable volumes as value measures . . . . .	20
2-4 Designing a case-specific loss function . . . . .	21
2-4-1 Including different risk affinities in the loss function . . . . .	25
2-5 1D geological reservoir model . . . . .	25
2-5-1 Construction of the uncertain 1D geological model . . . . .	26
2-5-2 Abstract valuation of the 1D geological model . . . . .	27

2-6	3D geological reservoir model . . . . .	28
2-6-1	Design of the 3D geological reservoir model . . . . .	29
2-6-2	Construction of the uncertain 3D geological reservoir model . . . . .	29
2-6-3	Determination of the maximum trap volume . . . . .	30
2-6-4	Finding the decisive spill or leak point of a trap . . . . .	31
2-6-5	Checking for juxtapositions and possible fault sealing . . . . .	35
2-6-6	Calculating the maximum trap volume . . . . .	36
2-6-7	Implementation of reservoir-related likelihoods in the 3D model . . . . .	36
2-6-8	Bayesian analysis and evaluation for the 3D geological model . . . . .	37
<b>3</b>	<b>Results</b>	<b>39</b>
3-1	1D geological reservoir model results . . . . .	39
3-1-1	Scoring . . . . .	39
3-1-2	Bayesian inference using thickness likelihood functions . . . . .	40
1D - Inference case I: Moderately reinforcing information . . . . .	42	
1D - Inference case II: Likely reliable seal . . . . .	43	
1D - Inference case III: Safe seal but likely subpar reservoir thickness . . . . .	45	
3-2	3D geological reservoir model results . . . . .	46
3-2-1	3D - Prior model . . . . .	46
3-2-2	3D - Posterior model I: Seal and reservoir likely thick . . . . .	48
3-2-3	3D - Posterior model II: Likely thin reservoir formation . . . . .	50
3-2-4	3D - Posterior model III: Likely thin seal . . . . .	51
3-2-5	3D - Posterior model IV: SSF likelihood reinforcing trap reliability . . . . .	53
3-2-6	3D - Posterior model V: Controversial information about the Shale Smear Factor . . . . .	55
<b>4</b>	<b>Discussion</b>	<b>57</b>
	State of knowledge, decision uncertainty and consequent decision making via loss function optimization . . . . .	57
	Impact of additional information on decision making . . . . .	58
	Value distribution modes as possible model scenarios and potential decision options . . . . .	60
	Comparison to common practices and research in the hydrocarbon sector . . . . .	61
	Representativity and limitations of this methodology . . . . .	62
	Possibilities for future research and extensions . . . . .	62
	<b>Bibliography</b>	<b>65</b>
<b>A</b>	<b>Appendix</b>	<b>71</b>
A-1	Code availability . . . . .	71
A-2	Additional tables and figures . . . . .	72

---

## List of Figures

2-1	Realizations of loss based on the absolute-error loss function (blue) and the squared-error loss function (red) for a determined true value $\theta = 0$ . . . . .	6
2-2	Expected loss for estimates of the true value and Bayes actions based on the standard absolute-error loss (A) and squared-loss function (B). In this example, the probability distribution of the true value is normal around zero ( $\mu = 0$ ; $\sigma = 500$ ; shown in light blue). . . . .	7
2-3	Example visualization of a 2D joint probability space generated by two random parameters $\theta$ (from De la Varga and Wellmann (2016)). . . . .	9
2-4	Illustration of the concept of interpolating to attain a potential field. The original data is depicted in (a), with contact points as dots and orientation measurements indicated by arrows. Colors represent respective assignments to different formations. An accordingly calculated potential field is shown in (b) (from Calcagno et al. (2008)). . . . .	12
2-5	Illustrations depicting the concept of Shannon entropy to visualize uncertainties in spatial applications. In (a), a map composed of uncertain units is subdivided into a regular grid of equally sized cells. The probabilities of possible outcomes regarding each unit is estimated for each cell in (b). From this results a map of cell Shannon entropies (c), with the highest values where all units can occur equally frequent, and lowest for cells where no uncertainty is given and entropy is zero (from Wellmann and Regenauer-Lieb (2012)). . . . .	15
2-6	Conceptual examples of a dome-shaped four-way-closure (a) and a simple fault trap (b) from top view (relief contour) and cross section perspective (modified from Dolson (2016a)). . . . .	17

2-7 In (a), a structural trap resulting from the combination of 4-way anticlinal closure and a simple normal fault is illustrated. The two reservoir layers in both sides are juxtaposed, so that the hydrocarbon accumulation potential is controlled by three points of possible leak pathways: (1) the anticlinal spill point, (2) leakage upwards along the fault and (3) leakage across the fault enabled by the juxtaposition. Possibilities (2) and (3) depend on the transport properties of the fault zone, i.e. potential fault sealing. Given leakage along the fault (2), that size volume would be reduced to a small relatively small volume solely defined by the 4-way closure down to maximum contact of the reservoir-seal boundary with the fault plane. In case (b), the reservoirs are not juxtaposed and thus laterally sealed. Fault-related leakage can thus only occur along the plane. Leakage along and across the fault is enabled by the juxtaposition in (c) (modified from van der Zee et al. (2003)). . . . .	18
2-8 Conceptual fault section illustrating the Shale Smear Factor approach to assess shale smear potential (modified from Vrolijk et al. (2016).) . . . . .	19
2-9 Single steps (I-IV) of customizing the loss function applied to an exemplary normal distribution ( $\mu = 0; \sigma = 500$ ; illustrated n light blue). The median (in this case also mean and average) is returned for the Bayes action, when using the standard symmetric absolute-error loss function (I). Assigning a stronger weight on overestimation steepens the curve on the right hand side and shifts the minimum to the left, i.e. to a lower estimate (II). Steepening is significantly reinforced by the introduction of fatal overestimation in (III). This affects only the positive side of estimates and leads to a jump at zero, where signs change. Due to a similar condition, the same effect is observed on the negative side of estimate values, where the curve is also steepened, after including fatal underestimation (IV). Due to this, the Bayes action is shifted back to the zero estimate. The final custom loss function is represented by the curve in (IV). . . . .	23
2-10 Loss based on the customized loss function (Equation 2-20) for determined true scores of -750, 0 and 750. This plot is meant to clarify the way real losses are incurred for each guess, relative to a given true score value. The expected loss, as seen in Figure 2-9, is acquired by arithmetically averaging such deterministic loss realizations based on the true score probability distribution by using Equation 2-6.	24
2-11 Plotting of expected loss realizations after including the risk factor $r$ in the loss function (Equation 2-21) for actors with risk affinities ranging from risk-averse ( $r = 0.5$ and $0.75$ ), over risk-neutral ( $r = 1$ ), to risk-friendly ( $r = 1.25$ and $r = 1.5$ ). The loss function was applied the same normal distribution ( $\mu = 0; \sigma = 500$ ) as in Figure 2-9. . . . .	26
2-12 Probability distributions for positions of layer boundaries in the subsurface and a respective representation using lines. These normal distributions are determined by the following values: Seal top: $\mu = 2000$ m, $\sigma = 7$ m; reservoir top: $\mu = 2050$ m, $\sigma = 25$ m; reservoir bottom: $\mu = 2200$ m, $\sigma = 45$ m. . . . .	27
2-13 Probability distributions for the three factors used in the score-based reservoir valuation as formulated in Equation 2-22: (A) reservoir thickness $h_{res}$ , (B) reservoir top depth $d_{res}$ and (C) seal thickness $h_{seal}$ . These are deduced from the 1D model input parameters and are thus uncertain. Here, we show a comparison between the three factors as deduced from prior parameters in Figure 2-12 and as determined from exemplary posterior parameter distributions. . . . .	28

2-14 Illustration of the design and construction of the 3D structural geological model. A 2D cross section through the middle of the model, perpendicular to the normal fault, is shown in (A). A 3D representation of the model, highlighting the reservoir and seal formations as voxels, is visualized in (B). In (C) and (D), the inclusion of parameter uncertainties is presented. Colors indicate certain layer bottoms (i.e. boundaries) which are assigned a shared normal distribution on which their z-positional uncertainties are based (C). All points in the hanging wall are additionally assigned a fault offset uncertainty based on a skew normal distribution (D). Thicknesses of the three middle layers are defined by the distances of boundary points (E) and are thus directly dependent on (C). These thicknesses are to be defined as likelihoods. . . . .	30
2-15 Illustration of the process of trap recognition, i.e. the conditions that have to be met by a model voxel, to be accepted as belonging to a valid trap. A voxel has to be labeled as part of the target reservoir formation (1) and positioned in the footwall (2). Trap closure is defined by the seal shape and the normal fault (3). Consequently, the maximum trap fill is defined by either the anticlinal spill point (3;a) or a point of leakage across the fault, depending on juxtapositions with layers underlying (3;b) or overlying the seal (3;c). The latter is only relevant if the critical Shale Smear Factor is exceeded, as determined over $D$ and $T$ in (4). In this example, assuming sealing of the fault due to clay smearing, the fill horizon is determined by the spill point in (4). Subsequently, only trap section 1 is isolated from the model borders in (4) and can thus be considered a closed trap. . . . .	32
2-16 Saddle point (red dot) between two maxima. In a geological setting, these surface maxima may be interpreted as two dome-shaped four-way closure traps. Spill-related migration between the two structures would take place over the saddle point, i.e. the spill point. . . . .	34
2-17 Surface and saddle point (red dot) generated by the function $z = x^2 - y^2$ . Maxima in direction $y$ is marked by a red, minima in direction $x$ by a white dashed line. Considering the surface as a seal, consequent buoyant flow directions are indicated by arrows. Such flow would be directed away from minima and towards maxima, with the saddle point indicating a junction and divide, i.e. a possible spill point. . . . .	35
2-18 Illustration of our probabilistic model (3D) as a hierarchical Bayesian network after Koller and Friedman (2009). <i>Stochastic</i> nodes are represented by ellipses (blue for priors, yellow for likelihoods). <i>Deterministic</i> functions are depicted as triangles in red. Arrows indicate direct connections from parent to child nodes. We included the most important functions that contribute to the automatic trap recognition and volumetric calculation in our structural geological model. . . . .	38
3-1 Posterior probability distributions from modeling scores using two (A) and three parameters (B) (reservoir thickness, reservoir top depth and seal thickness with a safety threshold of 20 m). . . . .	39
3-2 Plotting of expected loss realizations after including the risk factor $r$ in the loss function for actors with risk-affinities ranging from risk-averse ( $r = 0.5$ and $0.75$ ), over risk-neutral ( $r = 1$ ), to risk-friendly ( $r = 1.25$ and $r = 1.5$ ), based on the application of the custom loss function (Equation 2-21) on a prior score distribution (see Figure 3-1 (B)) from simple Monte Carlo error propagation. . . . .	40

3-3	Prior (A1) and posterior distributions (A2) of the layer boundary positions in depth and respective representations (A2, B2). Bayesian inference was conducted using likelihoods defined as follows: Seal thickness: $\mu = 25 \text{ m}; \sigma = 20 \text{ m}$ ; reservoir thickness: $\mu = 180 \text{ m}; \sigma = 40 \text{ m}$ . From (A1) to (B1), the distributions are slightly narrowed. Seal top and reservoir top distributions are still overlapping in (B1). A moderate reduction in uncertainty is also indicated by the representation in (B2), compared to (A2).	41
3-4	1D - Inference case I. Reservoir score distributions (A) and change in the realizations of expected loss for several risk parameters (B1, B2) before and after Bayesian updating based on likelihoods defined as follows: Seal thickness: $\mu = 25 \text{ m}; \sigma = 20 \text{ m}$ ; reservoir thickness: $\mu = 180 \text{ m}; \sigma = 40 \text{ m}$ .	43
3-5	1D - Inference case II. Reservoir score distributions (A) and change in the realizations of expected loss for several risk parameters (B1, B2) before and after Bayesian updating based on likelihoods defined as follows: Seal thickness: $\mu = 50 \text{ m}; \sigma = 20 \text{ m}$ ; reservoir thickness: $\mu = 180 \text{ m}; \sigma = 40 \text{ m}$ .	44
3-6	1D - Inference case III. Reservoir score distributions (A) and change in the realizations of expected loss for several risk parameters (B1, B2) before and after Bayesian updating based on likelihoods defined as follows: Seal thickness: $\mu = 70 \text{ m}; \sigma = 10 \text{ m}$ ; reservoir thickness: $\mu = 100 \text{ m}; \sigma = 30 \text{ m}$ .	45
3-7	Recoverable oil volumes probability distribution for the prior 3D model (a) and respective realization of the custom loss function (b).	48
3-8	Summary of results from evaluating posterior model I (3D). Shannon entropies in prior (a) and posterior (b) are compared. So are the mechanisms of maximum trap volume control (c). Prior and posterior ROV probability distributions are shown in (d). Respective loss function and Bayes actions are plotted in (e).	49
3-9	Summary of results from evaluating posterior model III (3D). Shannon entropies in prior (a) and posterior (b) are compared. So are the mechanisms of maximum trap volume control (c). Prior and posterior ROV probability distributions are shown in (d). Respective loss function and Bayes actions are plotted in (e).	52
3-10	Summary of results from evaluating posterior model IV. Shannon entropies in prior (a) and posterior (b) are compared. So are the mechanisms of maximum trap volume control (c). Prior and posterior ROV probability distributions are shown in (d). Respective loss function and Bayes actions are plotted in (e).	54
3-11	Summary of results from evaluating posterior model V. Shannon entropies in prior (a) and posterior (b) are compared. So are the mechanisms of maximum trap volume control (c). Prior and posterior ROV probability distributions are shown in (d). Respective loss function and Bayes actions are plotted in (e).	56
4-1	ROV distribution of the prior model subdivided by modes into scenarios which could pose decision options (boundaries marked by green lines). Red lines indicate a discretization of decision options according to fixed scales of resource allocations for a project. For both cases, zero equals the option to "take no action", i.e. to allocate no resources.	60
A-1	Prior (A1) and posterior distributions (B1) of the layer boundary positions in depth and respective representations (A2, B2) for 1D inference case II.	72
A-2	Prior (A1) and posterior distributions (B1) of the layer boundary positions in depth and respective representations (A2, B2) for 1D inference case III.	72
A-3	3D model construction input data (1): point-positional values for layer interfaces and the fault surface.	73

---

A-4	3D model construction input data (2): point-positional values for layer interfaces and the fault surface. . . . .	74
A-5	3D model construction input data (3): dip-related values for layer interfaces and the fault surface. . . . .	74
A-6	Summary of results from evaluating posterior model II (3D). Shannon entropies in prior (a) and posterior (b) are compared. So are the mechanisms of maximum trap volume control (c). Prior and posterior ROV probability distributions are shown in (d). Respective loss function and Bayes actions are plotted in (e). . . . .	75
A-7	3D posterior model I: Geweke convergence analysis (a) and plotted traces (b) for uncertain priors. In (a), the standard deviation between the mean value of one trace interval and the following is represented by the Z-score. Scores in the range between -2 and 2 indicate convergence of the MCMC sampling process. . . . .	76
A-8	3D posterior model II: Geweke convergence analysis (a) and plotted traces (b) for uncertain priors. In (a), the standard deviation between the mean value of one trace interval and the following is represented by the Z-score. Scores in the range between -2 and 2 indicate convergence of the MCMC sampling process. . . . .	77
A-9	3D posterior model III: Geweke convergence analysis (a) and plotted traces (b) for uncertain priors. In (a), the standard deviation between the mean value of one trace interval and the following is represented by the Z-score. Scores in the range between -2 and 2 indicate convergence of the MCMC sampling process. . . . .	78
A-10	3D posterior model IV: Geweke convergence analysis (a) and plotted traces (b) for uncertain priors. In (a), the standard deviation between the mean value of one trace interval and the following is represented by the Z-score. Scores in the range between -2 and 2 indicate convergence of the MCMC sampling process. . . . .	79
A-11	3D posterior model V: Geweke convergence analysis (a) and plotted traces (b) for uncertain priors. In (a), the standard deviation between the mean value of one trace interval and the following is represented by the Z-score. Scores in the range between -2 and 2 indicate convergence of the MCMC sampling process. . . . .	80



---

## List of Tables

3-1	Thickness likelihoods defined by normal distributions, as used for the three inference cases of the 1D model. . . . .	42
3-2	Prior parameter uncertainties defined by distributions with respective means $\mu$ , standard deviations $\sigma$ and shape factor $\alpha$ , as used in all model simulations (3D). Points belonging to the same layer interface share the same normal distribution (a). The offset uncertainty (b) is based on a skew normal distribution that affects all positional points in the hanging wall. . . . .	47
3-3	Layer thickness likelihoods determined by normal distributions as used for posterior model I (3D). . . . .	50
3-4	Layer thickness likelihoods determined by normal distributions as used for posterior model II (3D). . . . .	50
3-5	Layer thickness likelihoods determined by normal distributions as used for posterior model III (3D). . . . .	51
3-6	Layer thickness likelihoods and SSF likelihood determined by normal distributions as used for posterior model IV (3D). . . . .	53
3-7	SSF likelihood determined by a normal distributions as used for posterior model V (3D). . . . .	55



---

## **Acronyms**

**MAP** Maximum a posteriori

**MCMC** Markov chain Monte Carlo

**NPV** Net present value

**OOIP** Original oil-in-place

**ROV** Recoverable oil volumes

**SSF** Shale Smear Factor



---

# Chapter 1

---

## Introduction

Bayesian methods are an intuitive approach to inference, naturally inherent in human thinking patterns and closely tied to processes of decision making (Berger, 2013; Davidson-Pilon, 2015; Jaynes, 1986). Individuals are constantly faced with situations in which a decision has to be made, but only incomplete information is available. Such a problem necessitates an approach based on plausible reasoning, one which is intuitively structured in four stages (Jaynes, 1986):

1. Identify uncertainties and attempt to consider all possibilities that might arise.
2. Based on all the information and past experience available, evaluate how likely every possibility is.
3. Assess the probable consequences of single possible actions.
4. Based on the foregone steps, make a decision (Jaynes, 1986).

This concept can be related to a vast variety of problems, ranging from casual every-day situations to complex scenarios in large-scale economic decision making: As a private person, should I take an umbrella with me today? As a company, should we invest in the development and realization of a certain project? Following this process of plausible reasoning, the quality of a decision is to be measured based on the preceding state of knowledge and reasonable expectations, not on the subsequent actual consequences (Jaynes, 1986). In other words: A decision is optimal, as long as it is the best action given the information available to the decision maker before making the decision, no matter if actual loss was incurred afterwards. Bayesian decision theory and the related concepts of expected loss and loss functions have found increasingly common application in several economic sectors and fields of research, such as medicine (Ashby and Smith, 2000; Ashby, 2006; Moyé, 2006) and machine learning (Barber, 2012; Theodoridis, 2015). Probabilistic approaches to decision making have also become prevalent in hydrocarbon exploration and production (Murtha et al., 1997; Mudford et al., 2000; Bratvold and Begg, 2010). However, in this sector, the methods are mainly limited to conducting simple Monte Carlo simulations and results are often interpreted considering only percentiles and single values, such as the mean. Bayesian inference and Markov chain Monte

Carlo methods (MCMC) have only recently received more attention by researchers in this field (see [Wadsley et al. \(2005\)](#), [Ma et al. \(2006\)](#) and [Liu et al. \(2010\)](#)).

In general geosciences, Bayesian inference has prominently found use in the context of geo-physical inversion problems (see [Tarantola and Valette \(1982\)](#); [Mosegaard et al. \(2002\)](#) and [Sambridge and Mosegaard \(2002\)](#)). Recent developments have transferred this probabilistic approach to address uncertainties in the field of structural geological modeling. [Caumon \(2010\)](#), [Jessell et al. \(2010\)](#) and [Wellmann et al. \(2010\)](#) developed methods of geologically based inversion by considering secondary geological observations to constrain uncertain models. Advancements in this field have been enabled by progressing developments regarding implicit modeling functions based on interpolation and the possibility of fully automated model reconstruction in particular ([Hillier et al., 2014](#); [Mallet, 1992](#); [Lajaunie et al., 1997](#)). [De la Varga and Wellmann \(2016\)](#) regarded geological modeling as a Bayesian inference problem by relating additional geological information to prior model parameters in the form of likelihood functions, linking them in a non-parametric Bayesian network. Using Markov chain Monte Carlo sampling to explore resulting probability spaces, they attained posterior model suites with reduced uncertainties.

This work builds upon their concept, exploring the potential significance their findings might have in the context of decision making. For this, we include Bayesian decision theory in the step of model evaluation. This is achieved by assigning an economic meaning to the structural model and designing a case-specific custom loss function to find decisions which are optimal related to the state of knowledge and the preferences of actors with different risk affinities. More specifically, the models are designed to represent potential hydrocarbon reservoir systems. The development of algorithms for automatic structural trap recognition and volumetric calculation represents a central part of this work.

The main hypothesis of this work is that Bayesian inference and resulting changes in uncertainties in a geological setting have a significant effect on reservoir value estimation and decision making. We furthermore postulate that loss functions can be customized to appropriately represent preferences of actors in the hydrocarbon sector and moreover illustrate the nature of decisions such actors might make depending on their individual attitudes towards risk and in the face of different types of uncertainties. Changes in their respective decisions are treated as a suitable measure to assess the effect of updating model parameters with additional geological information.

---

# Chapter 2

---

## Methods

In the following chapter, we present the methodology utilized in this work. Bayesian analysis and decision theory are introduced in Section 2-1. Focus is laid on Bayesian inference, estimation of uncertain values and the use of loss functions. We apply these methods in the context of structural geological modeling. Respective approaches to computational modeling, specifically in a probabilistic framework, are described in Section 2-2. Regarding numerical implementation, GemPy and PyMC are presented as central tools used in a Python environment. In Section 2-3, we outline our methods to evaluate consequent modeling results. Particularly the potential for valuation from an economic perspective is elaborated and basic principles of subsurface hydrocarbon systems are introduced. Considering the respective setting in the economic sector of petroleum exploration and production, the development of an according case-specific custom loss function is described in Section 2-4. We first apply these methods to a conceptual 1D geological model (see Section 2-5), subsequently on a full 3D structural geological model. Design, construction and methods to identify hydrocarbon trap features in such a 3D model are explained in Section 2-6.

### 2-1 Bayesian analysis and decision theory

As implied by the name, the problems and reasoning behind decision making are examined in the field of decision theory (Berger, 2013). Such decision problems are commonly influenced by parameters that are uncertain. In statistical decision theory, available statistical knowledge is used to gain information on the nature of these uncertainties. Such uncertain parameters can be considered as numerical quantities. In order to find the best decision to a problem, it is possible to combine sample information with other aspects such as the possible consequences of decision making and the availability of prior information on our uncertainties. Decision consequences are expressed as gains in economic decision theory and as losses, which equal negative gains, in statistics (Berger, 2013). Prior information might be given for example based on experience from previous similar problems or from expert knowledge (Bratvold and Begg, 2010). The approach of utilizing priors is known as Bayesian analysis, which is explained in the following.

### 2-1-1 Basic elements

First, some basic elements are to be defined. The unknown (uncertain) quantity influencing decision making is usually denominated as the state of nature  $\theta$  (Berger, 2013). Given statistical information on  $\theta$  in the form of probability distributions,  $\theta$  is called the parameter. Decisions are also referred to as actions  $a$ . The outcome of statistical tests in form of information or statistical evidence is denoted as  $y$ . Loss is defined as  $L(\theta, a)$ , so  $L(\theta_1, a_1)$  is the actual loss incurred when action  $a_1$  is taken while the true state of nature is  $\theta_1$  (Berger, 2013). Loss, expected loss and loss functions are explained in detail further below.

### 2-1-2 Bayesian inference

The principles of Bayesian inference have been presented and discussed extensively in literature (see Jaynes (2003), Box and Tiao (2011), Harney (2013), Gelman et al. (2014) and Davidson-Pilon (2015)). It is most importantly characterized by its preservation of uncertainty, in contrast to standard statistical inference. The Bayesian approach is widely seen as intuitive and inherent in the natural human perspective. Probability is seen as a measure of belief for an event to occur. These beliefs can be assigned to individuals. Thus, different and even contradicting beliefs about the probability of an event might be held by different individuals, based on variations and disparities in the information available to each one individual.

The initial belief or guess about an event  $\theta$  can be denoted as  $p(\theta)$ . This is used as the so-called prior probability on which Bayesian updating is based. The beliefs about the occurrence of an event are revalued in the presence of additional information, i.e. the observation of new evidence  $y$ . These observations are included as likelihoods  $p(y|\theta)$ . By conducting this process of inference, a posterior probability  $p(\theta|y)$  is attained. It is important to note that the prior is not simply discarded but re-weighted by Bayesian inference. By utilizing an uncertain prior, the potential for wrongfulness of the initial guess is already included. This means that Bayesian updating is about reducing uncertainty in a belief and reaching a guess that is less wrong. Bayesian inference is defined by and conducted via the following equation, called the Bayes' Theorem (Jaynes, 2003; Gelman et al., 2014; Box and Tiao, 2011; Harney, 2013; Davidson-Pilon, 2015):

$$p(\theta|y) = \frac{p(y|\theta)p(\theta)}{p(y)} \propto p(y|\theta)p(\theta). \quad (2-1)$$

### 2-1-3 Estimation

The resulting posterior distribution can be used to acquire point estimates for the true state of nature  $\theta$ . Common and simple examples for such estimators are the mode (i.e. the generalized maximum likelihood estimate), the mean and the median of a distribution (Berger, 2013). The presentation of a point estimate should usually come with a measure for its estimation error. According to Berger (2013), the posterior variance is most commonly used as an indication for estimate accuracy. However, it is argued by Davidson-Pilon (2015) that by using pure accuracy metrics, while this technique is objective, it ignores the original intention of conducting the statistical inference in cases, in which payoffs of decisions are valued more

than their accuracies. A more appropriate approach can be seen in the introduction of loss and the use of loss functions ([Davidson-Pilon, 2015](#)).

#### 2-1-4 Expected loss and loss functions

Loss is a statistical measure of how "bad" an estimate is, i.e. how much is lost by making a certain decision. Gains are considered by statisticians as negative losses. The magnitude of incurred loss related to an estimate is defined by a loss function, which is a function of the estimate of the parameter and the true value of the parameter ([Wald, 1950](#); [Davidson-Pilon, 2015](#)):

$$L(\theta, \hat{\theta}) = f(\theta, \hat{\theta}). \quad (2-2)$$

So, how "bad" a current estimate is, depends on the way a loss function weights accuracy errors and returns respective losses. Two standard loss functions are the absolute-error and the squared-error loss function. Both are simple to understand and commonly used ([Davidson-Pilon, 2015](#); [Hennig and Kutlukaya, 2007](#)).

As implied by its name, the absolute-error loss function returns loss as the absolute error, i.e. the difference between the estimate and the true parameter:

$$L(\theta, \hat{\theta}) = |\theta - \hat{\theta}|. \quad (2-3)$$

Accordingly, losses increasing linearly with the distance to the true value are returned for respective estimates. This means that all differences between relative errors are weighted equally, no matter whether they are found in the realm of relatively small or relatively large errors ([Hennig and Kutlukaya, 2007](#)).

Using the squared-error loss function returns losses that increase quadratically with distance of the estimator to the true parameter value ([Davidson-Pilon, 2015](#); [Moyé, 2006](#)):

$$L(\theta, \hat{\theta}) = |\theta - \hat{\theta}|^2. \quad (2-4)$$

This exponential growth of loss also means that large errors are weighted much stronger than small errors. This might come with over-valuation of distant outliers and misrepresentation of magnitudes in distance. Regarding this, the absolute-error loss function can be seen as more robust ([Davidson-Pilon, 2015](#)).

Both of these standard loss functions are symmetric and can be described as objectively aiming at a high precision in estimating the true parameter value (see Figure 2-1). [Davidson-Pilon \(2015\)](#) and [Hennig and Kutlukaya \(2007\)](#) propose that it might be useful to move away from these type of objective loss functions to the design of customized loss functions that specifically reflect an individual's (i.e. the decision maker's) objectives, preferences and outcomes. [Hennig and Kutlukaya \(2007\)](#) argue that choosing and designing a loss function involves the translation of informal aims and interests into mathematical terms. This process naturally implies the integration of subjective decisions and subjective elements. According to [Hennig and Kutlukaya \(2007\)](#), this is not necessarily unfavorable or "less objective", as it may better reflect an expert's perspective on the situation and contribute to a productive scientific discussion.

The standard loss functions defined above are symmetric, but can easily be adapted to be asymmetric, for example by weighting errors on the negative side stronger than those on the positive side. Preference over estimates larger than the true value (i.e. overestimation) is thus

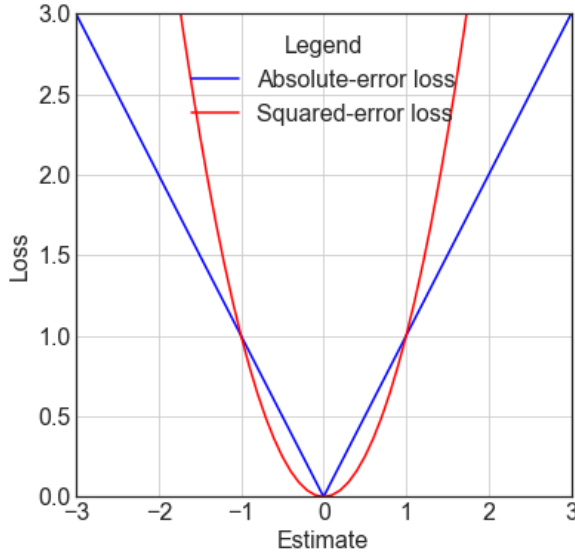


**Figure 2-1:** Realizations of loss based on the absolute-error loss function (blue) and the squared-error loss function (red) for a determined true value  $\theta = 0$ .

incorporated in an uncomplicated way (Davidson-Pilon, 2015; Hennig and Kutlukaya, 2007). Much more complicated designs of loss functions are possible, depending on purpose, objective and application. A case-specific loss functions is designed in Section 2-4 of this work. The presence of uncertainty during decision making implies that the true parameter is unknown and thus the truly incurred loss  $L(\theta, a)$  cannot be known at the time of making the decision. The Bayesian perspective considers unknown parameters as random variables and samples that are drawn from the posterior distribution as possible realizations of the unknown parameter, i.e. all possible true values are represented by this distribution. A probabilistic alternative to the actual loss is to consider each decision's expected loss and to make a decision that is optimal in relation to this expected loss (Berger, 2013; Davidson-Pilon, 2015). Given a posterior distribution  $p(\theta|y)$ , the expected loss of choosing an estimate  $\hat{\theta}$  over the true parameter  $\theta$  (after evidence  $y$  has been observed) is defined by the function below (Davidson-Pilon, 2015):

$$l(\hat{\theta}) = E_{\theta}[L(\theta, \hat{\theta})]. \quad (2-5)$$

The expectation symbol  $E$  is subscripted with  $\theta$ , by which it is indicated that  $\theta$  is the respective unknown variable. This expected loss  $l$  is also referred to as the Bayes risk of estimate  $\hat{\theta}$  (Berger, 2013; Davidson-Pilon, 2015).

By the Law of Large Numbers, the expected loss of  $\hat{\theta}$  can be approximated drawing a large sample size  $N$  from the posterior distribution, respectively applying a loss function  $L$  and averaging over the number of samples (Davidson-Pilon, 2015):

$$\frac{1}{N} \sum_{i=1}^N L(\theta_i, \hat{\theta}) \approx E_{\theta}[L(\theta, \hat{\theta})] = l(\hat{\theta}). \quad (2-6)$$

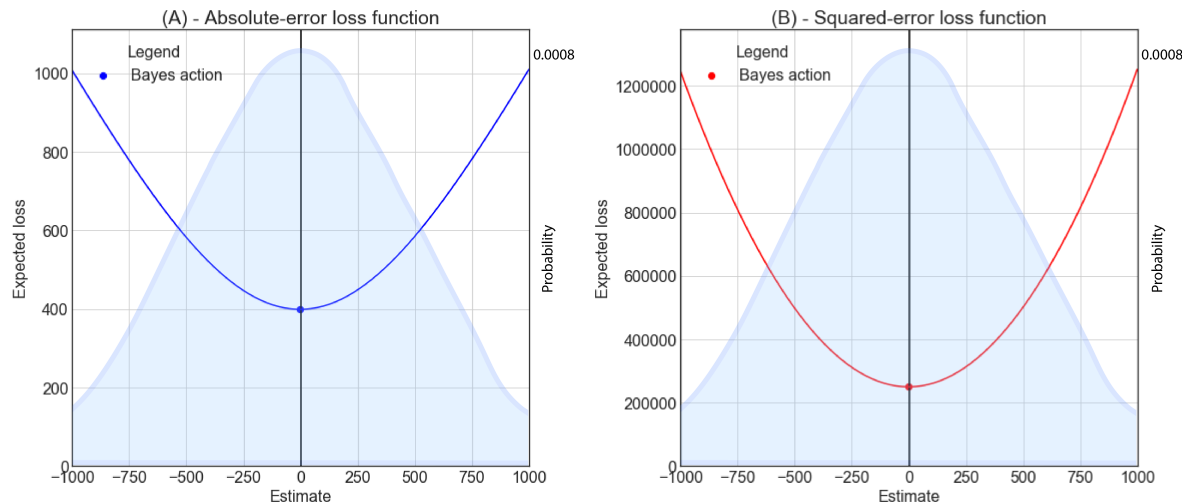


**Figure 2-2:** Expected loss for estimates of the true value and Bayes actions based on the standard absolute-error loss (A) and squared-loss function (B). In this example, the probability distribution of the true value is normal around zero ( $\mu = 0$ ;  $\sigma = 500$ ; shown in light blue).

Minimization of a loss function returns a Bayesian point estimate known as Bayes action or Bayesian estimator  $\delta^p(y)$ , which is the estimate, action or decision with the least expected loss according to the loss function (Berger, 2013; Moyé, 2006). For a unimodal and symmetric absolute-error loss function, the Bayes action is simply the median of the posterior distribution, while using squared-error loss it is the mean. The MAP (maximum a posteriori) estimate is the minimizing solution for the posterior using zero-one loss. The possibility of more than one minimum also implies that several Bayes actions can exist for one problem (Davidson-Pilon, 2015; Berger, 2013). Exemplary realizations of expected loss and Bayes actions according to both standard loss functions are plotted in Figure 2-2.

Davidson-Pilon (2015) implemented different risk affinities by simply introducing a risk parameter into the loss function. By using different values for this parameter, it can be represented how comfortable an individual is with being wrong and furthermore which "side of wrong" is preferred by this decision maker (Davidson-Pilon, 2015). This approach to expressing risk affinities is used for the design of the custom loss functions in Section 2-4.

## 2-2 Application in structural geological modeling

In this work, we apply these methods of Bayesian analysis and decision theory in the field of geological structural modeling. The fundamental approach follows closely the research conducted by De la Varga and Wellmann (2016) and builds upon their findings.

According to them, structural geological modeling can be regarded as a statistical problem and the elements of Bayesian inference can be specified in this context as follows:

1. **Mathematical forward model ( $M$ ):** The connections between parameters  $\theta$  and observed data  $y$  are defined in such mathematical models. According to Wellmann et al. (2010) and De la Varga and Wellmann (2016), the realization of a geological

model  $M$  can be regarded as a direct function of a set of input parameters:

$$M = f(\vec{x}, \phi_i, k_j, \alpha_k, \beta_l), \quad (2-7)$$

where  $\phi_i$  is a function of position  $\vec{x}$ , more precisely an interpolation function, to which respective additional interpolation parameters are given by  $\alpha_k$ . Available primary geological information, such as positions and dips of layer interfaces, is represented by  $k_j$ . A topological description, such as the relationships between faults and layer surfaces, is given by  $\beta_l$ . An essential aspect of this function is that it allows for a full automation of the modeling step, so that the consequences of a change in an input parameter are realized directly without the need for any further manual inspection or interaction (Wellmann et al., 2017; De la Varga and Wellmann, 2016). The modeling step and the respective interpolation method used in this work are presented in Section 2-2-2 below.

2. **Model parameters ( $\theta$ ):** These model-defining parameters can be deterministic or stochastic. In the latter case, they are uncertain parameters to which a probability distribution is assigned. Regarding Equation 2-7 above, these can be any of the factors  $\vec{x}$ ,  $k_j$ ,  $\alpha_k$  and  $\beta_l$ , which define the realization of the forward model over  $\phi_i$ .
3. **Observed data ( $y$ ):** This is any type of additional information that can be related to the forward modeling results or to the parameters and their combinations, and might possibly be used to reduce uncertainty. This comprises mostly secondary data that can not be incorporated directly as input parameters, such as geophysical measurements (gravity and magnetics), information from well-log analysis or simply geological rules.
4. **Likelihood functions  $p(y|\theta)$ :** Links between the previous parameters  $\theta$  and the additional data  $y$  are established by these functions in a way that they reflect the likelihood of the parameter states given the observations. They are mathematically defined in the same way as probability functions, but are a function of the data  $y$ , instead of the parameters  $\theta$  (MacKay, 2003; Patil et al., 2010; De la Varga and Wellmann, 2016).

A fundamental sequence of the inference process was proposed by Gelman et al. (2014), adapted by De la Varga and Wellmann (2016) and is subsequently adjusted for the application in this work as follows:

1. **Setting up a full probability model:** A multi-dimensional joint probability space is to be generated, taking into account the probability distributions of every model parameter  $\theta$ . A 2D example is illustrated in Figure 2-3.
2. **Conditioning on observed data:** Subsequently, an appropriate posterior distribution  $p(\theta|y)$  is to be calculated by conditioning the parameters  $\theta$  on the observed data  $y$  given the likelihood  $p(y|\theta)$ . This is the step of Bayesian updating of the belief about the parameter uncertainty given new information. In a chosen model ( $M$ ), this is achieved by linking parameters and data through deterministic operations to the likelihood functions. It is pointed out by De la Varga and Wellmann (2016) that any combination of parameter-observation connections is allowed, i.e. not all parameters need to be necessarily connected to all observed data. After all conditional probabilities have been set up, the Bayes Theorem (Equation 2-1) is applied to attain the posterior (De la Varga and Wellmann, 2016). However, due to the multi-dimensionality given in geological

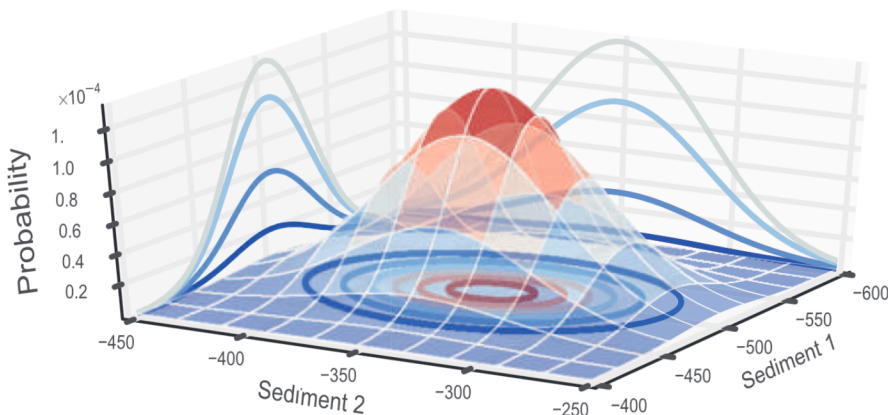


**Figure 2-3:** Example visualization of a 2D joint probability space generated by two random parameters  $\theta$  (from [De la Varga and Wellmann \(2016\)](#)).

problems, the use of Markov chain Monte Carlo methods is advised to achieve this as described in Section 2-2-1 below.

3. **Evaluation of the posterior model:** Depending on the aim of the study, a post-processing analysis can be conducted accordingly. [De la Varga and Wellmann \(2016\)](#) focused on the examination of the posterior distributions of the parameters  $\theta$  and the generated models, particularly regarding Shannon entropy which is explained here in Section 2-3-1. In this work, the geological models are additionally assigned an economic meaning by declaring them potential petroleum reservoirs and introducing customized loss functions to reflect the economic interest of decision makers in developing respective resource extraction projects (see Section 2-1-4). Changes in Bayes actions are considered a measure for the influence of Bayesian inference on decision making and the significance of additional observations for different decision makers.

### 2-2-1 Markov chain Monte Carlo sampling (MCMC)

Despite the apparent simplicity of the Bayes Theorem, a direct analytical calculation and exact inference of the posterior distribution  $p(\theta|y)$  is rarely possible in non-idealized cases, due to intractability in multi-dimensional spaces ([Hoffman and Gelman, 2014](#); [De la Varga and Wellmann, 2016](#)). Thereby arises the necessity to resort to methods of statistical inference approximation. Markov chain Monte Carlo (MCMC) sampling has proven to be a generally applicable and reliable method for exploring multi-dimensional parameter spaces in an intelligent way ([Hoffman and Gelman, 2014](#); [Davidson-Pilon, 2015](#)). [Gilks \(2005\)](#) has emphasized the significance of MCMC for the application in Bayesian statistics in particular.

In the ordinary Monte Carlo approach, random independent samples are drawn from a target distribution in order to approximate its shape ([Gilks, 2005](#); [De la Varga and Wellmann, 2016](#)). High-dimensional parameter spaces as found in Bayesian applications lead to vast spaces of likelihood and often make independent sampling infeasible ([Gilks, 2005](#)). This can be solved by extending the Monte Carlo principle with a Markov chain, in which every sample iteration of the parameter  $\theta^{(t+1)}$  is dependent uniquely on the previous value  $\theta^{(t)}$  ([Gilks, 2005](#); [De la](#)

[Varga and Wellmann, 2016](#)).

The general principle of MCMC can be described as follows: Drawing representative samples from a target distribution of unknown shape is based on the conduction of a so-called random walk on the parameter distribution space.  $T$  sampling steps are to be performed. The first sampling location is chosen at random. With each subsequent step, a new position is proposed. The new sample value is then related to the previous step. According to a weight defined by the scaled-up candidate density of the value, the proposed step is then accepted or rejected. In the case of acceptance, the value is added to the sample trace and the process is continued from the current location. In the case of rejection, sampling is reverted to the previous accepted step ([Schaaf, 2017](#); [De la Varga and Wellmann, 2016](#)). After performing the complete number of  $T$  iterations, all accepted sampling locations (i.e. the trace) are returned. The intention behind this concept it to achieve convergence of the sampling algorithm towards areas of high probability ([Davidson-Pilon, 2015](#)).

Variations in the way of how new sample steps are proposed and in the acceptance-rejection condition result in different single MCMC sampling methods ([Schaaf, 2017](#); [De la Varga and Wellmann, 2016](#)). Various algorithms for random MCMC walks have been developed for over more than six decades and advancements have still been made in recent years. Common examples for such algorithms are the Metropolis-Hastings samplers as devised by [Metropolis et al. \(1953\)](#) and generalized by [Hastings \(1970\)](#). The Gibbs sampler ([Geman and Geman, 1984](#)) is another well-known method. For the purpose of this work, an adaptive Metropolis-Hastings sampler is used.

In Metropolis-Hastings methods, each sampling step at iteration  $t$  is determined by a candidate probability distribution  $q(\theta, \theta')$ , from which a proposed sample  $\theta'$  is drawn. The acceptance-rejection condition is defined by the acceptance ratio  $a(\theta', \theta)$  ([Haario et al., 2001](#)):

$$a(\theta', \theta) = \frac{p(\theta')p(y|\theta')}{p(\theta)p(y|\theta)}. \quad (2-8)$$

To ensure a thorough exploration of the probability space, the transition to higher probability densities should not be enforced in every case but selectively. This is assured by relating the acceptance ratio from Equation 2-8 to a random value  $u$  from a Uniform distribution  $U(0, 1)$  as follows:

$$\theta^{(t+1)} = \begin{cases} \theta' & \text{if } a(\theta', \theta) > U(0, 1) \\ \theta^t & \text{otherwise} \end{cases}. \quad (2-9)$$

Thereby, the algorithm assigns high probabilities to high-density points and low probabilities to low-density points, so that the chain state is moved accordingly ([De la Varga and Wellmann, 2016](#)).

Metropolis methods are furthermore defined by the step size scale factor that is chosen. While large steps are good for exploration of the space and mixture in the chain, acceptance rates are low. Small steps have better acceptance rates, but lead to slower exploration and convergence of the algorithm ([De la Varga and Wellmann, 2016](#)).

For the iterative sampling in this work, Adaptive Metropolis (AM) by [Haario et al. \(2001\)](#) is used. It adapts the traditional Metropolis-Hastings by incorporating the ability of continuous step-size tuning during convergence, by taking into account the full information saved along

the process. This is achieved by generating a covariance matrix that is updated every iteration. The adaptive nature of the process enables fast convergence for non-linear distributions while maintaining ergodicity (Haario et al., 2001; De la Varga and Wellmann, 2016). Its suitability for multi-dimensional distribution spaces make it an excellent method for dealing with complex models such as structural geological models (Schaaf, 2017).

For sampling, a large enough number of iterations  $T$  has to be chosen, so that a reliable and statistically significant exploration of the parameter space is assured. This is primarily dependent on the rate of convergence towards the true distribution. Considering empirical Bayes methods, in which either priors or likelihoods stem from empirical data, as is assumed for the models in this work, convergence can be expected to be reached almost immediately (De la Varga and Wellmann, 2016). However, for high dimensional problems more iterations are required, in order to ensure an accurate representation of posterior distributions (Wellmann et al., 2017). Different realizations of the full 3D geological model are then constructed on the basis of the approximated posterior distributions, using an implicit modeling step described in the following.

## 2-2-2 Structural geological forward modeling

Performing forward modeling in the context of structural geology requires the use of a suitable modeling step  $M$  (see Equation 2-7). For the application in a probabilistic setting, the method should enable fully automatic reconstruction of the model, when parameters are changed. The application in this work follows the example of Wellmann et al. (2010) and De la Varga and Wellmann (2016), and relies on the use of implicit interpolation for geological modeling, a method developed and elaborated by Lajaunie et al. (1997) and Calcagno et al. (2008).

This implicit method relies on the interpolation of a potential field scalar function  $T(\vec{x})$  of any point  $\vec{x}$  in a 3D space, and thus reflects the geometry of geological structures (Calcagno et al., 2008). Modeling  $T(\vec{x})$  is achieved by cokriging two forms of data: (i) contact points on geological interfaces through increments of the potential field  $T(\vec{x}) - T(\vec{x}')$  and (ii) orientation data as gradients, i.e. partial derivatives of the potential field  $\delta T(\vec{x}) / \delta u_\beta$  in each direction  $u$  (Calcagno et al., 2008). The respective estimator is defined as follows:

$$T(\vec{x}) - T(\vec{x}_0) = \sum_{\alpha=1}^M \mu_\alpha (T\vec{x}_\alpha - T(\vec{x}'_\alpha)) + \sum_{\beta=1}^N \nu_\beta \frac{\delta T}{\delta u_\beta}(\vec{x}_\beta), \quad (2-10)$$

where  $\vec{x}_0$  is an arbitrary origin,  $M$  and  $N$  are the total number of data points and partial derivatives respectively, and their relative contributions are weighted by the factors  $\mu_\alpha$  and  $\nu_\beta$ . Furthermore,  $T$  is assumed to be a random function defined by polynomial drift and a stationary covariance  $K(h)$  (Calcagno et al., 2008). The use of a cubic covariance model is suggested by Calcagno et al. (2008), based on the results from studies conducted by Aug (2004) and Chilès et al. (2004).

Resulting potential fields can be used to describe geological interfaces as iso-surfaces in any kind of 3D geometry (Calcagno et al., 2008). A conceptual illustration is depicted in Figure 2-4. Fault geometries can be interpolated analogously. These can be infinite in the 3D space, interrelated in a fault network or finite. To account for the effect of faults on geological layers, discontinuous potential fields are created by applying discontinuous drift functions in the cokriging system. Additionally, geological rules allow for the representation of several

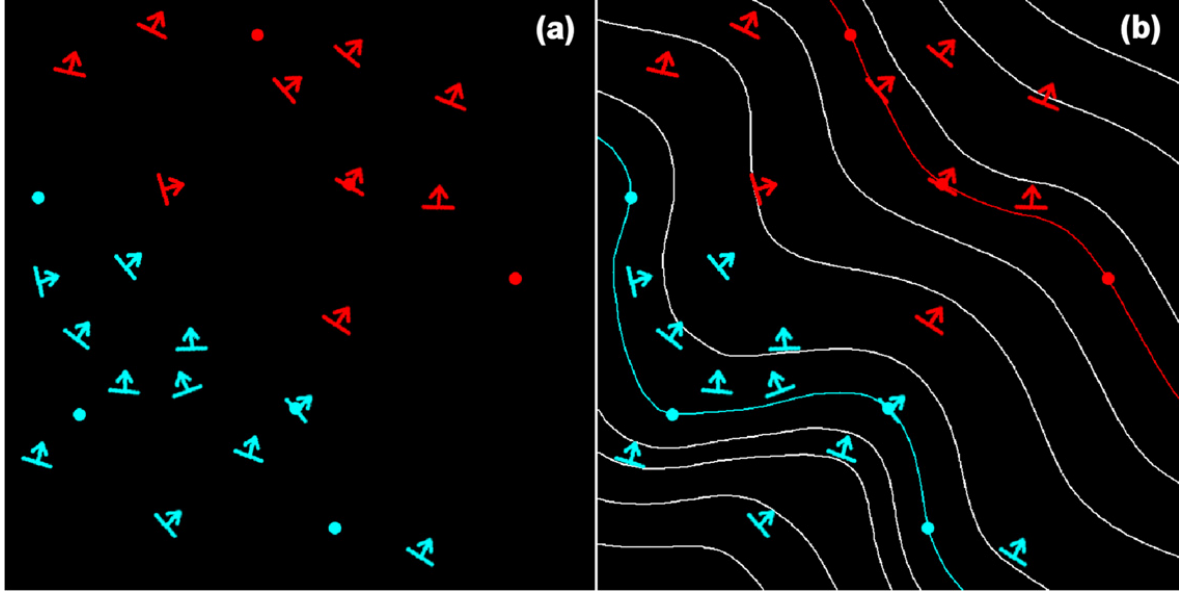


**Figure 2-4:** Illustration of the concept of interpolating to attain a potential field. The original data is depicted in (a), with contact points as dots and orientation measurements indicated by arrows. Colors represent respective assignments to different formations. An accordingly calculated potential field is shown in (b) (from [Calcagno et al. \(2008\)](#)).

types of interactions between sets of geological layers ([Calcagno et al., 2008](#)).

It is pointed out by [Calcagno et al. \(2008\)](#), that this method is particularly appropriate for cases in which knowledge about the geology is only given for sparse locations and is thus applicable for a wide variety of typical problems in geological settings. Furthermore, the model topology is defined by the knowledge contained in the geological pile (set of formations). Thus, the model can be updated in the face of new data or interpretations without the need to consider the impact on the geometry of formations, as this is automatically managed by the rules entailed in the geological pile ([Calcagno et al., 2008](#)).

### 2-2-3 Numerical computational implementation

Bayesian analysis can be conducted numerically using probabilistic programming methods ([Salvatier et al., 2016](#)). The implicit method of forward geological modeling, described above, is to be embedded in such a framework. For doing so, the programming language of choice in this work is Python. The merits of Python have been pointed out by [Behnel et al. \(2010\)](#), [Langtangen \(2008\)](#) and [Salvatier et al. \(2016\)](#). Development is facilitated by an expressive but concise and clean syntax that is easy to learn. Python is dynamic, compatible with multiple platforms and offers good support for numerical computing. Integration of other scientific libraries and extension via C, C++, Fortran or Cython are easily possible ([Behnel et al., 2010; Salvatier et al., 2016; Langtangen, 2008](#)). Python is thus a straightforward tool for the implementation of central components of Bayesian analysis, such as custom statistical distributions and samplers ([Salvatier et al., 2016](#)).

The 3D geological modeling step in this work is implemented using GemPy, an open-source,

Python-based software that is able to generate and visualize complex 3D structural geological models based on the potential field interpolation method elaborated in Section 2-2-2 (De la Varga and Schaaf, 2017). Its design allows for its application in a probabilistic setting as elaborated below. At the time of writing this, GemPy is still under development (version 0.997), but is already functioning for the purpose of this work.

For conducting the Bayesian analysis and embedding the geological modeling step in a probabilistic context, we integrate GemPy into the probabilistic framework of PyMC. This Python library was developed for conducting Bayesian inference and prediction problems in an open-source probabilistic programming environment (Davidson-Pilon, 2015; Salvatier et al., 2016). Different model fitting techniques are provided in PyMC, such as the *maximum a posteriori* (MAP) method and several MCMC sampling methods, including the Adaptive Metropolis introduced in Section 2-2-1. Furthermore, several approaches for checking MCMC convergence are included in PyMC. Here, we rely on a time-series method proposed by Geweke et al. (1991). Convergence is hereby assessed by comparing mean and variance of subsequent intervals in the sampling chain. Resulting scores (Z-scores) can be plotted using PyMC. If a trace has converged, most of the score points should be found within two standard deviations around zero. Also, the initial part of a sampling chain (before convergence) can be discarded by declaring a "burn-in" phase (Geweke et al., 1991; Patil et al., 2010; Davidson-Pilon, 2015). The components which are used to construct a statistical model, are represented by *Deterministic* or *Stochastic* functions or variables in PyMC (Salvatier et al., 2016). These are described as hierarchically related nodes, specifically parent and child nodes, in a Bayesian network:

1. **Parent** nodes include variables that affect other variables.
2. **Child** nodes contain variables that are influenced by other variables (they depend on parent variables) (Ben-Gal, 2007; Koller and Friedman, 2009).

The values of *Deterministic* variables are completely dependent on its parents' values, as defined by a respective mathematical function (Salvatier et al., 2016). *Stochastic* variables are used to represent uncertain parameters  $\theta$  or observed stochastic variables as likelihood functions  $p(y|\theta)$ . Complex mathematical relations between *Stochastic* variables can be described through *Deterministic* functions. Furthermore, PyMC allows for the creation of own object definitions inheriting from the class descriptions of these two function and variable types (Salvatier et al., 2016; De la Varga and Wellmann, 2016).

Bayesian networks as a concept have been presented in further detail by Koller and Friedman (2009). Salvatier et al. (2016) have pointed out that the development of PyMC is continuing, as the inclusion of further tools is planned for future updates.

## 2-3 Model evaluation

After conducting Bayesian inference, posterior distributions and resulting model realizations are to be evaluated. For this, we can examine sampling traces and posterior distributions of single parameters or their combinations. The entirety of accepted 3D geological models (sampled after a burn-in phase) is to be assessed in terms of uncertainty quantification and visualization. Furthermore, a central part of this work is the assignment of an economic

significance to the modeling results. To achieve this, we evaluate accepted models by regarding them as potential hydrocarbon systems. We explain this process in detail in Section 2-3-2. Shannon entropy is introduced as a measure for uncertainty in the following.

### 2-3-1 Visualizing uncertainty

Shannon entropy, commonly also referred to as information entropy, was first defined by [Shannon \(1948\)](#) and adopted as a method to visualize uncertainties in 3D geological models by [Wellmann and Regenauer-Lieb \(2012\)](#). This approach was later also used by [De la Varga and Wellmann \(2016\)](#) and [Schaaf \(2017\)](#). Shannon entropy is applied to predict the model accuracy at every location in the model space by visualizing its respective uncertainty and thus returning a measure for the quality of the model. This is achieved by subdividing the model space into a regular raster of equally sized cells (voxels) and measuring the accuracy for every such cell. In the context of geological modeling, the central question is based on the knowledge of how frequent a single geological feature occurs in a voxel ([Wellmann and Regenauer-Lieb, 2012](#)). [De Luca and Termini \(1972\)](#) established that Shannon entropy can serve as a measure of fuzziness, a concept described by [Zadeh \(1965\)](#). Given a fuzzy set in which fuzziness of each part is indicated by  $f \in [0, 1]$ , the following conditions hold:

1. The measure should only be 0 if  $f$  is 0 or 1 in every cell.
2. The measure is maximal given  $f = 0.5$  in every cell ([De Luca and Termini, 1972](#)).

While the first condition represents the complete absence of uncertainty everywhere in the model, the second condition is met in the opposite case of full uncertainty in the whole model space, i.e. all outcomes are equally likely in each cell ([Schaaf, 2017](#)). From this, the following equation for application in geological modeling was derived ([Mann, 1993; Wellmann and Regenauer-Lieb, 2012](#)):

$$H_m = -\frac{1}{N} * \sum_{x=1}^N [p_m(x) * \log(p_m(x)) + (1 - p_m(x)) * \log(1 - p_m(x))], \quad (2-11)$$

in which  $f$  is denoted as the probability  $p_m$  of an outcome  $m \in M$  in a cell with a position  $x$ . The fuzziness is quantified as the entropy  $H_m$ , normalized by the total number of cells  $N$ . Subsequently, an average Shannon entropy can be calculated for a model as ([Wellmann and Regenauer-Lieb, 2012](#)):

$$H_T = -\frac{1}{N} \sum_{x=1}^N H(x). \quad (2-12)$$

This total entropy  $H_T$  is 0 when no uncertainty is found in any cell, oppositely it is maximal in the case of equal probabilities of outcomes in every cell. The application of these entropy measures allows for the calculation and visualization of uncertainties in each voxel, the assessment of uncertainties of entire geological units, as well as the quantification of total model uncertainty represented by a single number ([Wellmann and Regenauer-Lieb, 2012](#)).

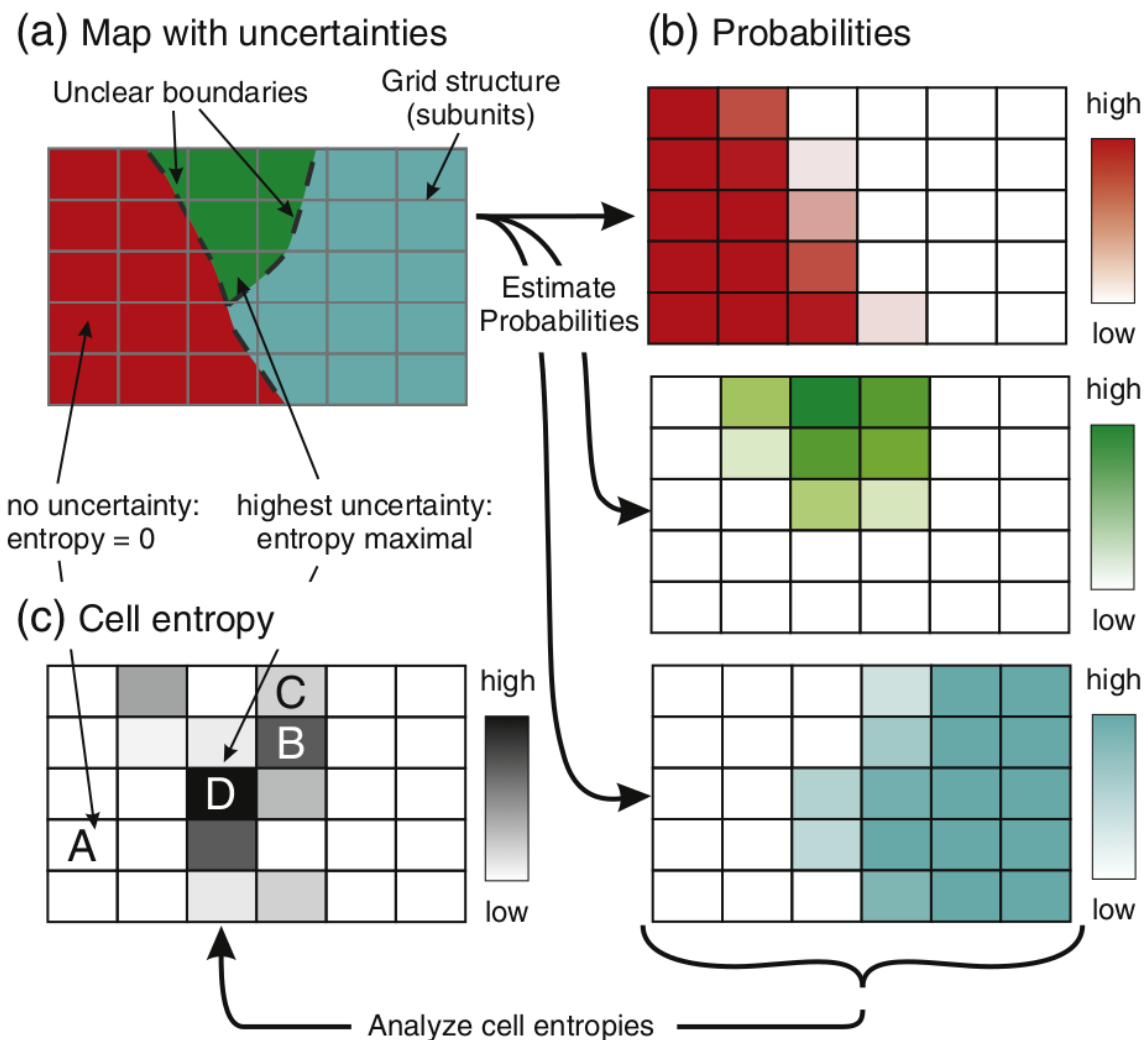


**Figure 2-5:** Illustrations depicting the concept of Shannon entropy to visualize uncertainties in spatial applications. In (a), a map composed of uncertain units is subdivided into a regular grid of equally sized cells. The probabilities of possible outcomes regarding each unit is estimated for each cell in (b). From this results a map of cell Shannon entropies (c), with the highest values where all units can occur equally frequent, and lowest for cells where no uncertainty is given and entropy is zero (from Wellmann and Regenauer-Lieb (2012)).

### 2-3-2 Economic significance of structural geological models as hydrocarbon systems

In this work, the generated structural geological models are to be assigned an economic significance in order to approach a real setting, in which hypothetical actors could have an interest in taking a decision, and thus, to evaluate the influence of the Bayesian inference of the decision making process. Changes in Bayes actions are considered a measure for this effect. For this purpose, it is assumed that a hydrocarbon reservoir system is represented by each geological model realization. Such hydrocarbon systems are typically comprised of the following elements:

1. **Source rock:** A kerogen-rich source rock which produced and emitted hydrocarbons during its burial history, given sufficient heating, is needed to provide oil or gas in the first place (Dolson, 2016a; Selley and Sonnenberg, 2014). These are typically organic-rich sedimentary rocks, shales in particular. For the purpose of this work, it is assumed that a suitable source rock is present and hydrocarbons expulsion took place after the formation of any trap-defining structures in our geological models.
2. **Migration pathway:** A pathway that allows expelled oil and gas to migrate upwards through the subsurface from the source rock into potential reservoir formations is necessary (Dolson, 2016a; North, 1985; Selley and Sonnenberg, 2014). This condition is also assumed to be given in our model. Basement formations in the geological model are simply defined to be permeable.
3. **Seal:** These are formations that able to halt hydrocarbons on their migration pathway as top, lateral and possibly bottom seals (Dolson, 2016a; Sorkhabi and Tsuji, 2005). Such sealing is generally defined by a reduction of pore space geometry relative to migration energy, primarily due to changes in stratigraphical composition to low porosities and micro-sized pore throats. These are characterized by a high capillary entry pressure able to resist the buoyancy pressure of hydrocarbons. This capillary pressure is also the main controlling factor for seal capacity. Lithologically, seals are most commonly comprised of shales, siltstones, tight carbonates, evaporites and salts (Dolson, 2016a,b; Sorkhabi and Tsuji, 2005). An additional factor to sealing is posed by the presence of faults. Fault zones may possess significantly higher or lower permeabilities than surrounding rock formations, which means that they may serve as fluid flow conduits or migration barriers respectively (van der Zee et al., 2003; Sorkhabi and Tsuji, 2005). The possible influence of faults on structural hydrocarbon traps is elaborated in further detail below. For the model in this work, the cap rock is assumed to be a shale.
4. **Reservoir formations:** Suitable lithologies, in which hydrocarbon volumes can be stored, have to be present. For this, a suitable percentage of void space, i.e. a sufficiently high porosity, is required in a rock formation. Further significant factors are the connectivity of the porosity through pore throats, as well as pore geometry and resulting permeability. The larger the pore throats, the easier it is for fluids to migrate in a rock. Typical reservoir rocks are sandstones and carbonates, but even normally tight lithologies might serve as reservoirs, if they are fractured (Dolson, 2016a; Sorkhabi and Tsuji, 2005; North, 1985; Selley and Sonnenberg, 2014). In the models of this work, reservoir formations are assumed to be conventional sandstones.

**5. Trap:** Entrapment results from an appropriate reservoir-seal sequence and a three-dimensional geometric closure. Regarding a top view on a structural relief, closure is generally defined by any intersection of a structural contour and the seal, that is closed on both sides (Dolson, 2016a; Sorkhabi and Tsuji, 2005; North, 1985). A point at which a contour fails to close is referred to as "spill point". The maximum column depth to which a trap can be filled, and ultimately its maximum volume, is defined by this spill point. A trap that contains hydrocarbons down to the spill point is thus referred to as "filled to spill". Traps can also be "filled to seal capacity" when the seal capacity is exceeded by the buoyant pressure of a fill column of greater height. Lower accumulations can also result from insufficient migration, i.e. low charge volumes of oil or gas in the first place. Such a trap is referred to as "charge limited" (Dolson, 2016a). Many different types of traps, in which hydrocarbons can accumulate, are possible. A common trap type is a structural four-way closure, i.e. as reservoir-seal system that was folded into closed anticlines, often resembling a dome. It is thus predominantly defined by the structural closure relief and the cap rock sealing capacity. Such a trap type can be considered to be closed, as the reservoir surface contours are closed in a circle or oval around a relief high. Closure can also be given through the intersection of a fault with the seal (Dolson, 2016a; North, 1985). Two common examples for traps are illustrated in Figure 2-6.

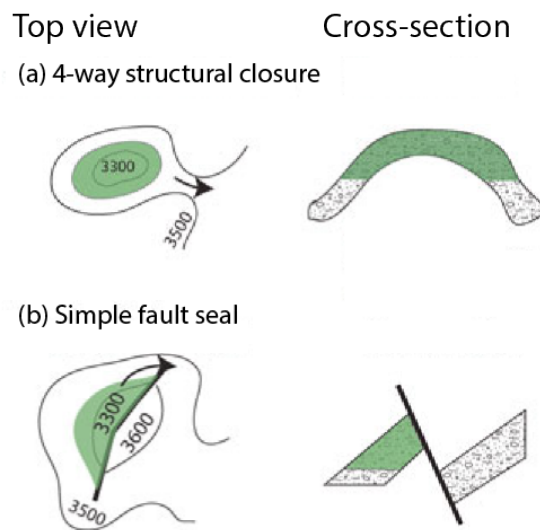


**Figure 2-6:** Conceptual examples of a dome-shaped four-way-closure (a) and a simple fault trap (b) from top view (relief contour) and cross section perspective (modified from Dolson (2016a)).

The presence of a fault in the reservoir-seal sequence can have different impacts on trap closure and the volume of a hydrocarbon accumulation. This is mainly defined by the transport properties of a fault, i.e. in which way it behaves as a seal or flow conduit respectively. Cases might range from complete fault sealing to complete leakage along a fault zone. More complex in-between cases are possible, such as faults that leak across but are sealed along their plane. This ultimately defines the depth to which a trap may be filled and whether this point is controlled by a point of leakage on the fault plane or a spill point related to the remainder of

the 3D structural closure. Another decisive aspect to consider is the nature of juxtapositions across the fault, especially regarding the possibility of cross-fault leakage ([van der Zee et al., 2003](#)). This is summarized in Figure 2-7.

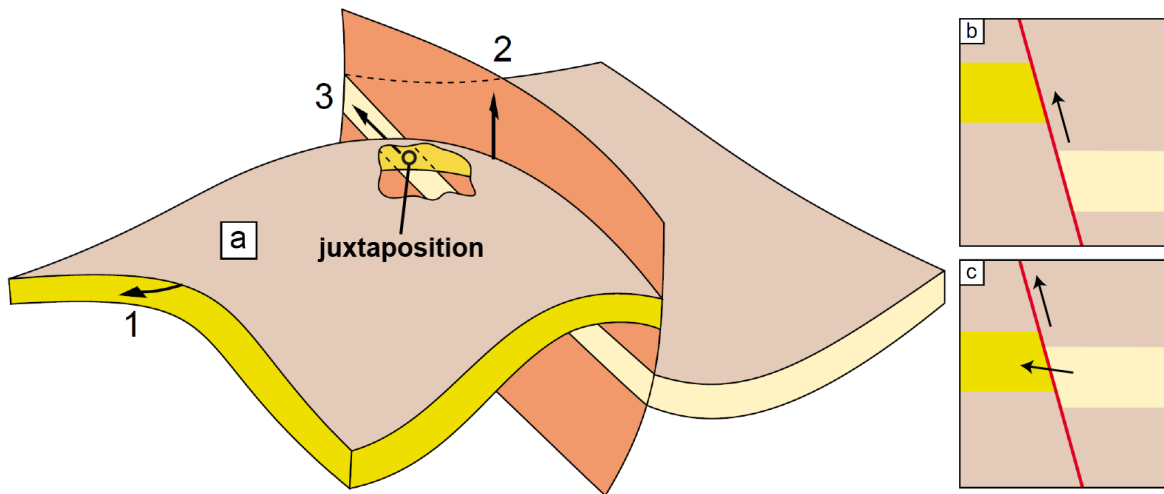


**Figure 2-7:** In (a), a structural trap resulting from the combination of 4-way anticlinal closure and a simple normal fault is illustrated. The two reservoir layers in both sides are juxtaposed, so that the hydrocarbon accumulation potential is controlled by three points of possible leak pathways: (1) the anticlinal spill point, (2) leakage upwards along the fault and (3) leakage across the fault enabled by the juxtaposition. Possibilities (2) and (3) depend on the transport properties of the fault zone, i.e. potential fault sealing. Given leakage along the fault (2), that size volume would be reduced to a small relatively small volume solely defined by the 4-way closure down to maximum contact of the reservoir-seal boundary with the fault plane. In case (b), the reservoirs are not juxtaposed and thus laterally sealed. Fault-related leakage can thus only occur along the plane. Leakage along and across the fault is enabled by the juxtaposition in (c) (modified from [van der Zee et al. \(2003\)](#)).

The transport properties of a fault zone are primarily defined by the internal structure and composition of its fault gouge. Fault gouge properties and ultimately the variation in permeability in the fault zone is primarily dependent on clay content. Clay smearing has thus been a central topic of research surrounding fault sealing (see [Lindsay et al. \(1993\)](#) [Yielding et al. \(1997\)](#), [van der Zee et al. \(2003\)](#), [van der Zee and Urai \(2005\)](#) and [Schmatz et al. \(2010\)](#)). It generally is defined as all processes that lead to the incorporation of clay from the wall rock (e.g. a shale as seal) into the fault zone ([van der Zee et al., 2003](#); [Vrolijk et al., 2016](#)). Clay smearing can be described using different equations, such as the Shale Smear Factor (SSF) and the Shale Gouge Ratio ([Lindsay et al., 1993](#); [Yielding et al., 1997](#); [Vrolijk et al., 2016](#)). The SSF provides a simple conceptual approach to assessing the clay smearing on a fault plane, dependent on ratio of fault throw magnitude  $D$  to displaced shale thickness  $T$  ([Lindsay et al., 1993](#); [Yielding et al., 1997](#); [Yielding, 2012](#)) (see Figure 2-8):

$$\text{SSF} = \frac{D}{T}. \quad (2-13)$$

It has been observed, that as the displacement and thus the ratio increases, a critical value

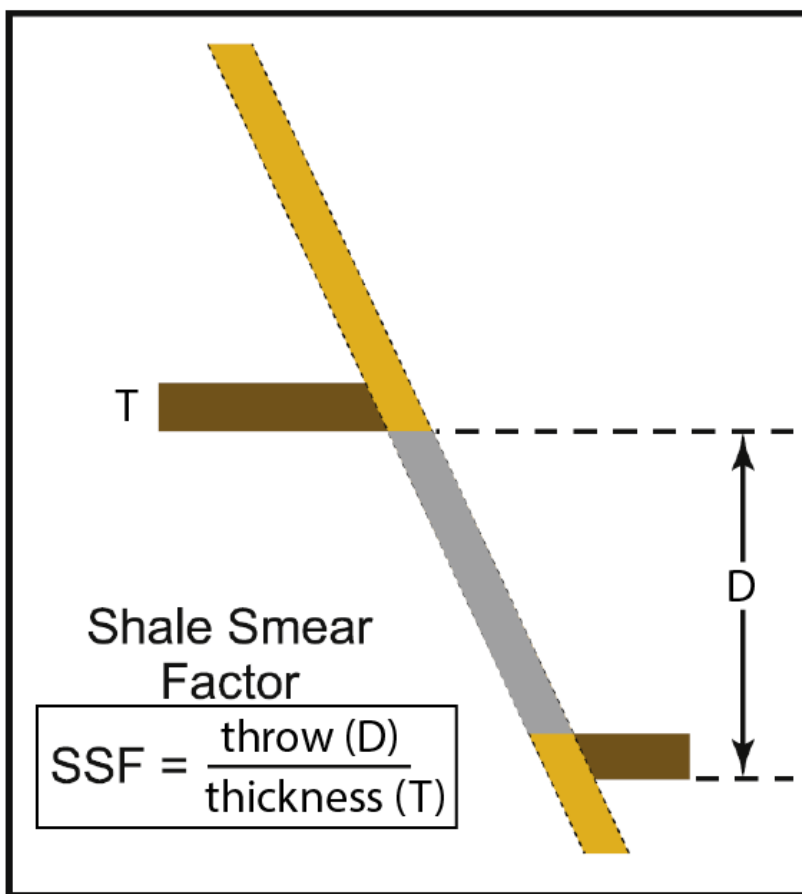


**Figure 2-8:** Conceptual fault section illustrating the Shale Smear Factor approach to assess shale smear potential (modified from [Vrolijk et al. \(2016\)](#).)

$\text{SSF}_c$  will be reached, at which the clay smear is breached and no longer continuous. Initial observations by [Lindsay et al. \(1993\)](#) indicated this threshold to be  $\text{SSF}_c = 7$ . However, the critical value was later suggested to be scale-dependent and smaller for thick clays displaced by large faults ([Yielding, 2012](#)). [Færseth \(2006\)](#) reported that for such large scales, including fault throws greater than 100 m, clay smear continuity can be expected for  $\text{SSF} \leq 4$ . Any larger values come with a decrease in confidence ([Færseth, 2006](#)). A critical review of the research on clay smearing published over the last four decades was recently presented by [Vrolijk et al. \(2016\)](#).

The 3D structural model in this work (see Section 2-6-1) is designed in a way that a potential conventional hydrocarbon trap is included in the form of anticlinal folding combined with normal faulting of a reservoir-seal sequence. Results from modeling are to be evaluated in a way that respective estimations on the basis of loss functions can be conducted, i.e. Bayesian decision theory is applicable. In the typical petroleum industrial setting, the main question is one of how much of the resource can be produced and how high the return on investment will be ([Dean, 2007](#)). Thus, several of the factors named above are to be considered to attain a calculable volume of the structural trap which can further be economically interpreted using the approaches presented below.

### 2-3-3 Original oil-in-place and recoverable volumes as value measures

Before pressure and production tests have been conducted (i.e. before production has started), volumetric estimation is the only approach to assess the amount of hydrocarbons in place in a reservoir. From this value, recoverable reserves can be deduced based on an estimated recovery factor (Dean, 2007; Morton-Thompson et al., 1993).

Oil-in-place and gas-in-place volumes are calculated based on:

1. Subsurface rock volume containing hydrocarbons. This is mainly defined by thickness and areal extend of the accumulation.
2. Weighted average effective porosity of the reservoir rock.
3. Water saturation in the reservoir rock.
4. Hydrocarbon fluid properties (Dean, 2007; Morton-Thompson et al., 1993).

As the hydrocarbon systems in this work are purely synthetic, we assume a pure oil accumulation for simplicity. Furthermore, defined formations are regarded as homogeneous in their lithological composition and petrological properties. Using the factors listed above, the equation for original oil-in-place (OOIP) is formulated as follows:

$$\text{OOIP} = A * h * \phi * (1 - S_W) * 1/\text{FvF}, \quad (2-14)$$

where OOIP is returned in m<sup>3</sup>. The hydrocarbon-filled rock volume is defined by the drainage area  $A$  in m<sup>2</sup> and the net pay thickness  $h$  in m. Porosity  $\phi$  and water saturation  $S_W$  (interstitial water) are given in fractions of the rock volume. A dimensionless factor for the change in oil volume between reservoir conditions and standard conditions at surface is represented by the formation volume factor FvF. Thus, shrinkage of the oil volume brought to the surface is determined by 1/FvF (Dean, 2007; Morton-Thompson et al., 1993).

Subsequently, the effectively recoverable oil volumes (ROV) can be calculated by multiplying the OOIP with a recovery factor RF (Dean, 2007; Morton-Thompson et al., 1993):

$$\text{ROV} = \text{OOIP} * \text{RF} = A * h * \phi * (1 - S_W) * 1/\text{FvF} * \text{RF}. \quad (2-15)$$

The recovery factor is influenced by a number of fluid properties, such as viscosity, density, solution oil/gas ratio and the formation volume factor. Thus, it is difficult to estimate (Dean, 2007). Globally, the ultimate average recovery factor for oil fields is about 35% (Labastie, 2011). For gas accumulations, however, recovery factors range typically between 70 and 90% (Dean, 2007).

In this work, the constructed geological models focus on the representation of the structural control in this equation. This refers in particular to potential structural traps and ultimately the hydrocarbon-filled rock volume represented by  $A * h$  in Equations 2-14 and 2-15. Including the remaining factors as simple uncertain parameters would be easily possible and is usually done in the probabilistic estimation procedures commonly conducted in the petroleum industry (Wim et al., 2001; Murtha et al., 1997; Mudford et al., 2000). However, results and observations related to structural geology might possibly be overprinted and distorted by incorporating other uncertain parameters belonging to petrology and engineering. Effects of interest might become unrecognizable. Thus, fixed values are used for the non-structural

factors. These are chosen arbitrarily and optimistic ( $\phi = 30\%$ ,  $S_W = 20\%$ ,  $FvF = 1.05$ ,  $RF = 80\%$ ), but within a realistic range for a very good conventional oil reservoir (for example values see [Morton-Thompson et al. \(1993\)](#), [Ahmed and Meehan \(2011\)](#) and [Dandekar \(2013\)](#)). Consequently, calculating the ROV from the maximum trap volume merely equates a rescaling of values, as proportions are conserved. Nevertheless, we deem the translation of trap volumes to recoverable oil volumes as appropriate for a formally better consideration of the results in the respective context of decision making in the hydrocarbon sector.

Attaining the hydrocarbon-filled rock volume (i.e. the maximum trap volume) and calculating the ROV is a central step of the model evaluation. Model realizations are hereby assigned the economic value on which decisions are to be based. Realized volumetric values from numerous iterations and several simulations are combined to sets of probability distributions of the ROV. Considering the ROV as the true value to be estimated, loss functions can then be applied as described in Section [2-1-4](#). OOIP and ROV calculations are applicable in a 3D setting, the 1D geological model introduced below in Section [2-5](#), however, requires the use of an abstract valuation system.

## 2-4 Designing a case-specific loss function

As explained before in Section [2-1-4](#), the standard symmetric loss functions provide objectively good estimators minimizing expected loss by returning the median or mean respectively. However, assigning an economic notion to our model and assuming the case of an actor or decision maker in any field, naturally necessitates the consideration of preferences, interests and the overall subjective perspective such an individual or for example a company might have. Further constraints, properties and factors can also be specific to the field, industry or generally to the problem at hand. Consequently, the design of a more specific non-standard and possibly asymmetric loss function might be required, so that an adapted Bayesian estimator can be found. One that includes subjective aspects and difference in weighting of particular gains or losses, arising from an actor's inherent preferences and the environment in which the actor has to estimate or make a decision. In the face of several uncertain parameters, a perfectly true estimate is virtually unattainable. However, an attempt can be made to design a customized loss function that returns a Bayesian estimator involving the least bad consequences for an individual in a specific environment ([Davidson-Pilon, 2015](#); [Hennig and Kutlukaya, 2007](#)). Assuming the reservoir setting case and valuation methods introduced in Section [2-3-2](#), such a customization attempt is made and explained step by step in the following.

For the purpose of estimation, it makes sense that one of the standard loss functions is chosen as a basis and a customized loss function is developed from there. The absolute-error loss seems most appropriate for this case of hydrocarbon reservoir value estimation. Ideally, an actor would like to know the exact true value of interest, say the ROV, so that investments or resources can be allocated appropriately in order to acquire economic gains. This allocation is the decision to be made or action to be taken. We hereby follow the definition by [Bratvold and Begg \(2010\)](#), who, in the context of hydrocarbon exploration and production, referred to a decision as a "conscious, irrevocable allocation of resources to achieve desired objectives". Thus, estimating the true value is deciding. Deviations from the unknown true value in the form of over- and underestimation bring about an error and loss accordingly. In this case, we assume that investments increase linearly with linear growth in the value of the reserve.

For this reason, the absolute-error loss function is favored here over the squared-error loss function. It is chosen as the base function to which further development steps refer, based on logical case-specific assumptions. The steps are illustrated in Figure 2-9 and listed in the following:

1. **Step I:** The standard symmetrical absolute-error loss function is chosen as a starting point for further customization steps:

$$L(\theta, \hat{\theta}) = |\theta - \hat{\theta}|. \quad (2-16)$$

2. **Step II:** Considering the development of a hydrocarbon reservoir, it can be assumed that over-investing is worse than under-investing. Overestimating the size of an accumulation might for example lead to the installation of equipment or facilities that are actually redundant or unnecessary. This would come with additional unrecoverable expenditures. Consequences from underestimating, however, may presumably be easier to resolve. Additional equipment can often be installed later on. Hence, overestimation is weighted stronger in this loss function by multiplying the error with an overestimation factor  $a$ :

$$L(\theta, \hat{\theta}) = |(\theta - \hat{\theta})| * a. \quad (2-17)$$

3. **Step III:** The worst case for any project would be that its development is set into motion, expecting a gain, only to discover later that the value in the reservoir does not cover the costs of realizing the project, resulting in an overall loss. A petroleum system might also turn out to be a complete failure, containing no value at all, although the actor's estimate indicated the opposite. Here, this is referred to as worst case or fatal overestimation. A positive value is estimated, but the true value is zero or negative. This is worse than the "normal" non-fatal overestimation, where both values are positive and a net gain is still achieved, which is only smaller than the best possible gain of expecting the true value. Fatal overestimation is included in the loss function by using another weighting factor  $b$  that replaces  $a$ :

$$L(\theta, \hat{\theta}) = |(\theta - \hat{\theta})| * b. \quad (2-18)$$

In other words: With  $b = 2$ , fatal overestimation is twice as bad as simple underestimation.

4. **Step IV:** A worst case or fatal underestimation can also be derived from the idea of estimating a zero or negative value, when the true value is actually positive. This is assumed to be worse than non-fatal overestimation, but clearly better than fatal overestimation. No already owned resources are wasted, it is only the potential value that is lost, i.e. opportunity costs that arise from completely discarding a reservoir with a potential gain equal to the positive true value. Fatal underestimation is weighted using a third factor:

$$L(\theta, \hat{\theta}) = |(\theta - \hat{\theta})| * c. \quad (2-19)$$

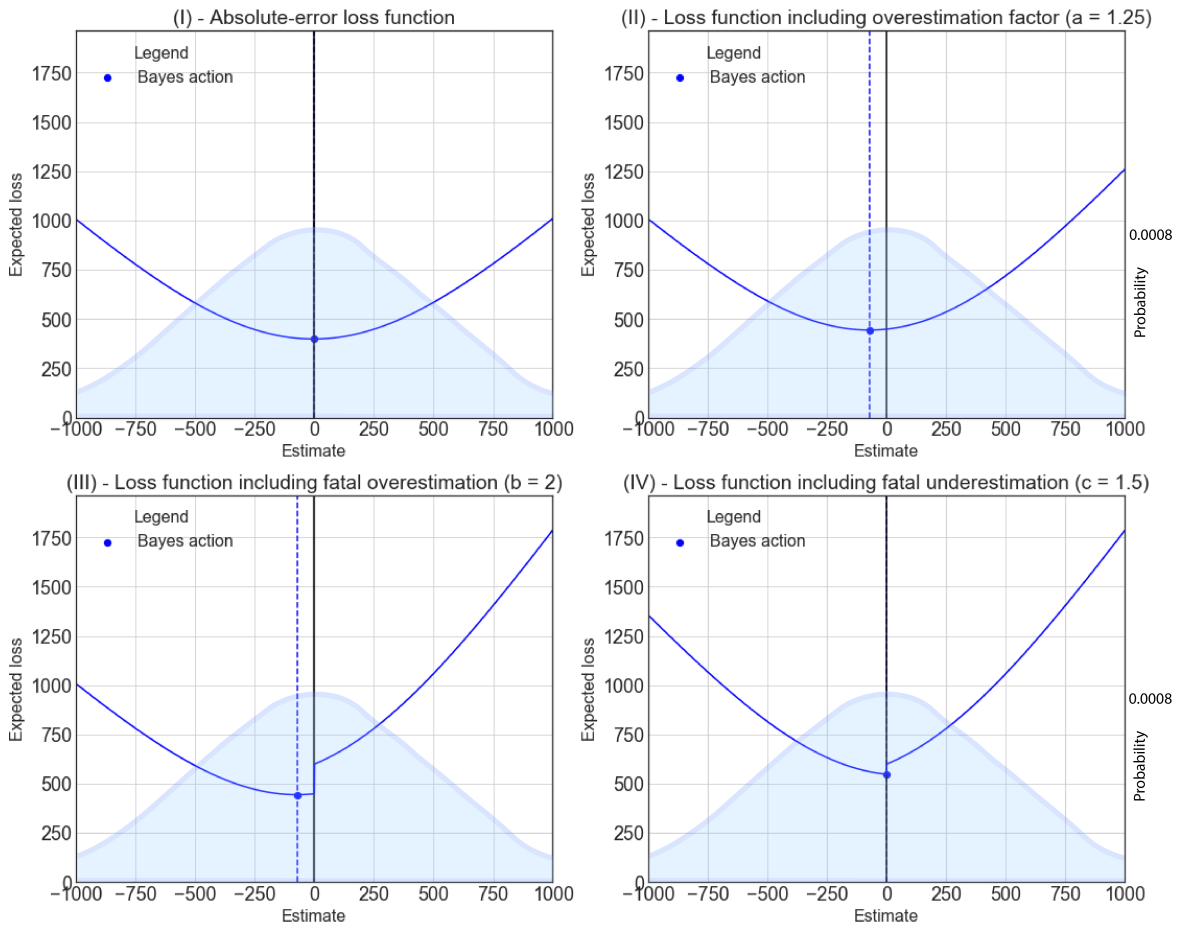


**Figure 2-9:** Single steps (I-IV) of customizing the loss function applied to an exemplary normal distribution ( $\mu = 0; \sigma = 500$ ; illustrated in light blue). The median (in this case also mean and average) is returned for the Bayes action, when using the standard symmetric absolute-error loss function (I). Assigning a stronger weight on overestimation steepens the curve on the right hand side and shifts the minimum to the left, i.e. to a lower estimate (II). Steepening is significantly reinforced by the introduction of fatal overestimation in (III). This affects only the positive side of estimates and leads to a jump at zero, where signs change. Due to a similar condition, the same effect is observed on the negative side of estimate values, where the curve is also steepened, after including fatal underestimation (IV). Due to this, the Bayes action is shifted back to the zero estimate. The final custom loss function is represented by the curve in (IV).

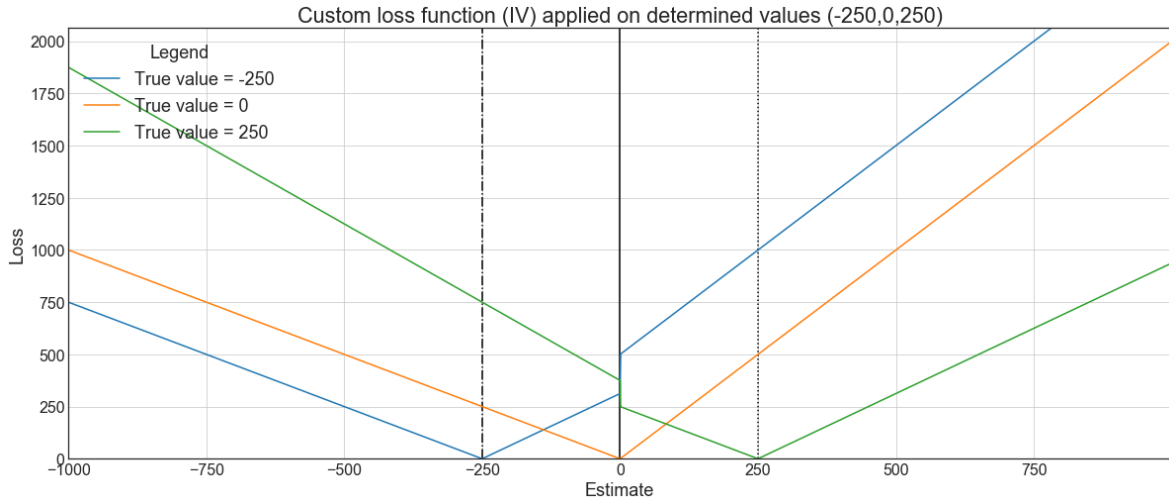


**Figure 2-10:** Loss based on the customized loss function (Equation 2-20) for determined true scores of -750, 0 and 750. This plot is meant to clarify the way real losses are incurred for each guess, relative to a given true score value. The expected loss, as seen in Figure 2-9, is acquired by arithmetically averaging such deterministic loss realizations based on the true score probability distribution by using Equation 2-6.

Combining these adaption steps and the conditions defined in them results in the following customized loss function:

$$L(\theta, \hat{\theta}) = \begin{cases} |\theta - \hat{\theta}|, & \text{for } 0 < \hat{\theta} < \theta \\ |\theta - \hat{\theta}| * a, & \text{for } 0 < \theta < \hat{\theta} \\ |\theta - \hat{\theta}| * b, & \text{for } \theta \leq 0 < \hat{\theta}, \text{ with } a, b, c \in \mathbb{Q}. \\ |\theta - \hat{\theta}| * c, & \text{for } \hat{\theta} \leq 0 < \theta \end{cases} \quad (2-20)$$

It is important to note that the weighting factors defined above can take basically any numerical values but should be chosen in a way that they appropriately represent the framework conditions of the problem. Here, based on the considerations named above, it is assumed that normal overestimation is 25% ( $a = 1.25$ ), fatal overestimation 100% ( $b = 2$ ) and fatal underestimation 50% ( $c = 1.5$ ) worse than normal underestimation. For better understanding of how these determine influence the incurrence, actual losses for three fixed true values are plotted in Figure 2-10.

It has to be emphasized that this is just one possible proposal for loss function customization. There exists not one perfect design for such a case (Hennig and Kutlukaya, 2007). Slight to strong changes can already be implemented by simply varying the values of the weighting factors  $a$ ,  $b$  and  $c$ . Fundamentally different loss functions can also be based on a significantly different mathematical structure. Loss functions are customized regarding the problem environment and according to the subjective needs and objectives of the decision maker (Davidson-Pilon, 2015; Hennig and Kutlukaya, 2007). Thus, they are mostly defined by the actor expressing his perspective. Changes in the individual's perception and attitude might lead to further customization needs at a future point in time, as was reported by Hennig and Kutlukaya (2007). Especially considering individual persons as actors, psychological aspects may play a significant role. Bratvold and Begg (2010) provided an overview on how

biases can influence and impair the decision making of otherwise smart actors.

### 2-4-1 Including different risk affinities in the loss function

It can be assumed that several actors in one sector or decision environment may have the same general loss function but different affinities concerning risks. This might be based for example on different psychological factors or economic philosophies followed by companies. It might also be based on budgets and options such actors have available. An intuitive example is the comparison of a small and a large company. A certain false estimate or error might have a significantly stronger impact on a company which has a generally lower market share and only few projects, than on a larger company which might possess a higher financial flexibility and for which one project is only one of many development options in a portfolio.

In the following, the loss function is further adapted to consider different risk affinities of several actors. Representing risk behavior in a loss function can also be done in different ways and regarding different types of risks. Here, bidding lower is considered the cautious, risk-averse option, as smaller losses can be expected from underestimating. Guessing higher is deemed riskier, as losses from overestimation are greater. However, bidding correctly on a higher value, will also return a greater gain. It is assumed that risk-friendly actors care less about fatal underestimation, i.e. they will rather develop a project than discard it. In the loss function, risk is simply included using a risk factor  $r$  which alters the incurred losses respectively:

$$L(\theta, \hat{\theta}) = \begin{cases} |\theta - \hat{\theta}| * r^{-0.5}, & \text{for } 0 < \hat{\theta} < \theta \\ |\theta - \hat{\theta}| * a * r, & \text{for } 0 < \theta < \hat{\theta} \\ |\theta - \hat{\theta}| * b * r, & \text{for } \theta \leq 0 < \hat{\theta} \\ |\theta - \hat{\theta}| * c * r^{-0.5}, & \text{for } \hat{\theta} \leq 0 < \theta \end{cases}, \quad \text{with } a, b, c, r \in \mathbb{Q}. \quad (2-21)$$

According to this, for  $r = 1$  the risk-neutral loss function is returned, as no re-weighting takes place. For  $r < 1$ , the weight on overestimating ( $a, b$ ) is reduced and increased for fatal underestimation ( $c$ ), as well as normal underestimation. This represents a risk-friendlier actor that is willing to bid on a higher estimate to attain a greater gain. For  $r > 1$ , the overestimation weight ( $a, b$ ) is increased in the loss function, underestimation and fatal underestimation weight ( $c$ ) are decreased and respectively more risk-averse actors are prompted to bid on lower estimates. Accordingly different loss function realizations are plotted in Figure 2-11. The factor  $r$  can take basically any positive values. However, since risk neutrality is expressed by  $r = 1$ , we consider values  $0 < r < 2$  to be the most appropriate choices to represent both sides of risk affinity equally here.

## 2-5 1D geological reservoir model

For simple understanding and a preliminary assessment of the Bayesian statistical methods, as well as the custom loss function described above, we first apply them to a conceptual one-dimensional hydrocarbon system case. The underlying model and basic approach are inherited from [De la Varga and Wellmann \(2016\)](#), but the parameters are adapted to more

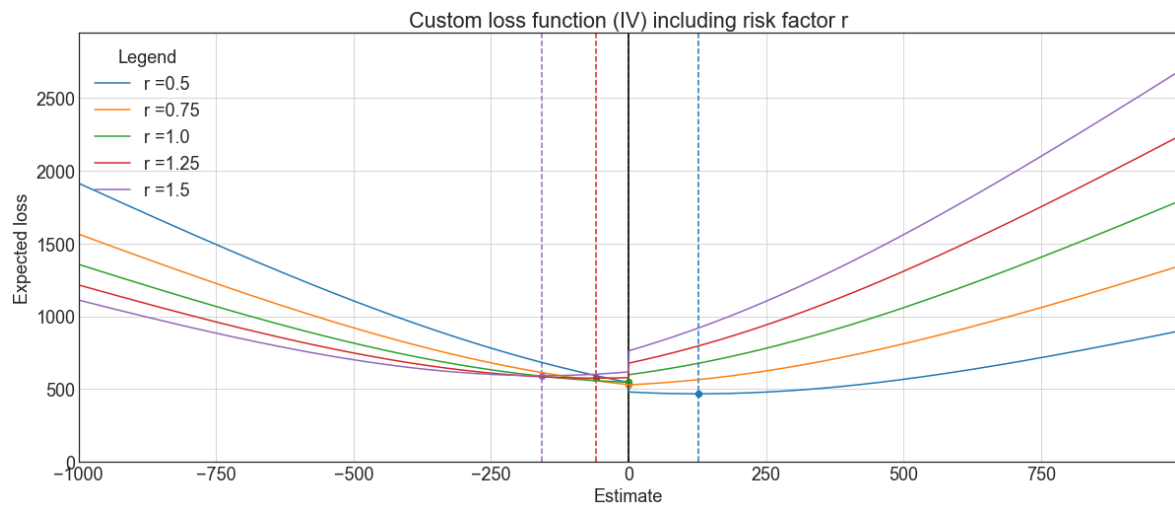


**Figure 2-11:** Plotting of expected loss realizations after including the risk factor  $r$  in the loss function (Equation 2-21) for actors with risk affinities ranging from risk-averse ( $r = 0.5$  and  $0.75$ ), over risk-neutral ( $r = 1$ ), to risk-friendly ( $r = 1.25$  and  $r = 1.5$ ). The loss function was applied the same normal distribution ( $\mu = 0; \sigma = 500$ ) as in Figure 2-9.

appropriately represent a reasonable geological petroleum system, consisting of a reservoir formation with overlying seal in the subsurface. In this 1D setting, only the interface depths and thicknesses of layers such as the reservoir or seal unit can be observed. We assume other defining aspects, such as structural entrapment, to be given. Limiting the model to only one dimension and a small number of uncertain stratigraphical parameters allows for a relatively straightforward and simplified approach to assessing an abstract type of value for a reservoir, applying the custom loss function (Equation 2-20) for value estimation and observing respective effects of Bayesian inference. The construction of this 1D geological model is described in the following.

### 2-5-1 Construction of the uncertain 1D geological model

De la Varga and Wellmann (2016) constructed a simple geological model using three uncertain positions in vertical one-dimensional space, marking hypothetical boundaries of layers in a subsurface column. The location probabilities for these points are defined by sampling from normal distributions. These points confine two layers in the middle, from which the upper one can be labeled as seal and the lower one as reservoir. The standard deviations ( $\sigma$ ) of the distributions increase with depth, representing an increase in uncertainty. For an approximate representation of a hydrocarbon reservoir system, the distribution means ( $\mu$ ) are set to depths of 2000 m (seal top,  $\sigma = 7$ ), 2050 m (reservoir top,  $\sigma = 25$ ) and 2200 m (reservoir bottom,  $\sigma = 45$ ). The resulting model with its prior distributions of possible layer boundary locations is illustrated in Figure 2-12. For conducting Bayesian inference, it is assumed that new observations are made, providing additional information considered here in the form of likelihood functions for the thicknesses of the two layers of interest. Likelihood functions for reservoir and seal thicknesses are introduced based on another set of normal probability distributions. These are directly related to the layer boundary positions, i.e. the

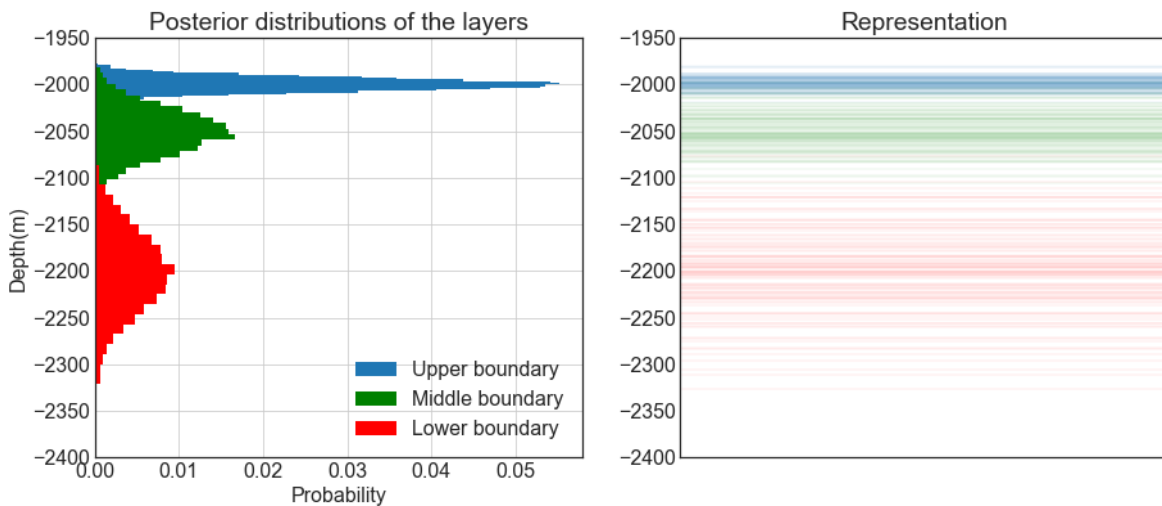


**Figure 2-12:** Probability distributions for positions of layer boundaries in the subsurface and a respective representation using lines. These normal distributions are determined by the following values: Seal top:  $\mu = 2000$  m,  $\sigma = 7$  m; reservoir top:  $\mu = 2050$  m,  $\sigma = 25$  m; reservoir bottom:  $\mu = 2200$  m,  $\sigma = 45$  m.

prior parameter distributions. Means and standard deviations of the likelihood distributions are variable, so that several scenarios based on the assumption of different observations can be tested. Parameter priors and likelihood functions are embedded into a probabilistic modeling framework as described in Section 2-2-3 and MCMC sampling is conducted accordingly. Performing Bayesian inference on such a 1D geological model follows the conceptual example devised by De la Varga and Wellmann (2016). Posterior distributions are to be evaluated based on the valuation method described in the following.

### 2-5-2 Abstract valuation of the 1D geological model

For valuating a simplified 1D model, OOIP and ROV calculations are not applicable, as these require a 3D setting. Given only layer boundary positions in one vertical dimension, we resort to an abstract way of reservoir valuation by defining a scoring system. A dimensionless reservoir score is made dependent on three factors derived from the uncertain 1D interface positions: (1) reservoir thickness, (2) reservoir top depth and (3) seal thickness. From these, (2) equals the prior parameter that indicates the reservoir-seal boundary in depth. The other two are respectively deduced from the distance between parameter values. According to this dependence, these values, which we use to valuate the reservoir, inherit the uncertainty from their parent parameters. An exemplary comparison between the distribution of these values depending on prior and posterior parameters is depicted in Figure 2-13. We hereby demonstrate how model uncertainties are translated to uncertainties related to valuation measures.

Assuming that reservoir thickness is a simplified indicator for the amount of extractable oil or gas and thus value in place, a gain in score can be correlated with increase in thickness. Here, we assign two score points to one meter of thickness. Increasing costs of drilling are indicated by increasing depth of the reservoir top. Consequently, we ascribe one negative

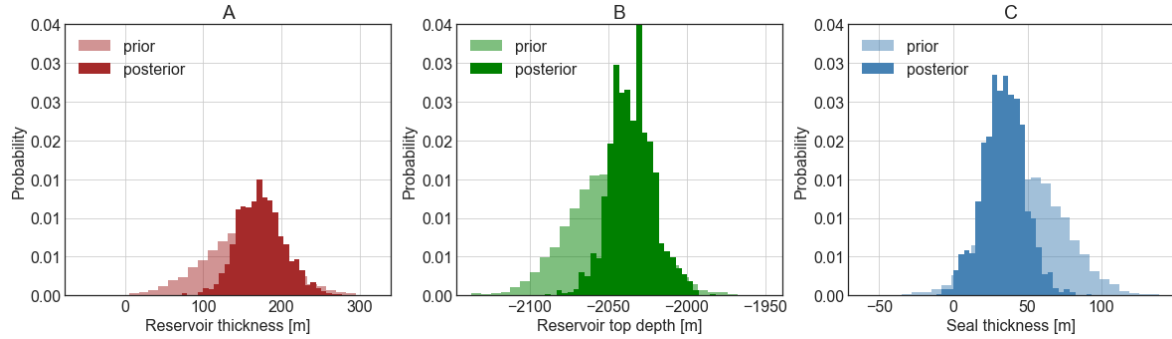


**Figure 2-13:** Probability distributions for the three factors used in the score-based reservoir valuation as formulated in Equation 2-22: (A) reservoir thickness  $h_{res}$ , (B) reservoir top depth  $d_{res}$  and (C) seal thickness  $h_{seal}$ . These are deduced from the 1D model input parameters and are thus uncertain. Here, we show a comparison between the three factors as deduced from prior parameters in Figure 2-12 and as determined from exemplary posterior parameter distributions.

score point to every meter in depth. Samples from the probability distributions of these two factors are drawn to model the true score of the reservoir (depth scores are subtracted from reservoir thickness scores). A third parameter is defined by the seal thickness. Score points are not added or subtracted by this parameter directly. Instead, we define a threshold for seal reliability beforehand. Here, it is set to 20 m thickness. If the seal thickness falls below this threshold, it is assumed that the seal fails completely and thus all the potential value (positive score) of the reservoir is lost, while costs of depth (negative score) remain. Thus, we include a condition to check whether the seal is reliable. We define a respective equation for the reservoir score  $S_{res}$  as:

$$S_{res} = \begin{cases} 2h_{res} + d_{res}, & \text{for } h_{seal} \geq 20 \\ d_{res}, & \text{for } h_{seal} < 20 \end{cases}, \quad (2-22)$$

where reservoir thickness is given by  $h_{res}$ , seal thickness by  $h_{seal}$  and reservoir depth, which is always a negative value, by  $d_{res}$ .

We apply this valuation method to the original prior-only Monte Carlo simulation of the 1D model as reference and then on each posterior distribution set after conducting Bayesian inference. Resulting score probability distributions can be compared directly and additionally under use of the case-specific custom loss function (Equation 2-21) defined before.

## 2-6 3D geological reservoir model

The concept of the 1D geological model is to be transferred and extended to a 3D setting that incorporates a more realistic and complete geological reservoir system. A three-dimensional space allows not only for better consideration of stratigraphical aspects, but also for the inclusion of structural formations, in particular hydrocarbon trap-defining features.

### 2-6-1 Design of the 3D geological reservoir model

For the purpose of exploring the application and effects of Bayesian analysis and decision theory in this work, the model is nevertheless to be kept conceptual and relatively simple. Stratigraphically, it is designed to include one main reservoir unit (sandstone), one main seal unit (shale), an underlying basement through which hydrocarbon fluids could have flown upwards and overlying formations that are assumed to be permeable, so that hydrocarbons can escape upwards. Structurally, it is constructed to feature an anticlinal fold that is displaced by a normal fault. All layers are tilted so that they dip in the opposite direction of the fault plane dip. The original concept of this model is designed in a way that a potential hydrocarbon trap is formed in the reservoir rock enclosed by the deformed seal and the normal fault. This trap, more specifically the trap volume, is defined as the central feature of economic interest. For conducting simple and straightforward volumetric calculations, it is assumed that found closed traps are always filled to spill with oil, i.e. the complete trap volume is hydrocarbon filled and the OOIP can be attained over this volume.

The maximum trap volume is assumed to equate the hydrocarbon-filled rock volume  $A * h$  in Equation 2-14 and is thus to be used to valuate each realization of the geological model. Single results are expected to vary, depending on the uncertain input parameters defined in Section 2-6-2 below. The custom loss function 2-21 is to be applied to the resulting value distributions before and after performing Bayesian inference. This way, the effect of incorporating additional information in the form of likelihoods is to be assessed from a perspective of Bayesian decision theory. It is furthermore assumed that the hydrocarbon trap volume is directly linked to a project development decision, i.e. investment and allocation of resources is represented by bidding on a volume estimate.

### 2-6-2 Construction of the uncertain 3D geological reservoir model

We construct the 3D structural geological model as follows: In principle, it is defined as a cubic block with an extent of 2000 m in  $x$ -,  $y$ - and  $z$ -directions. The basic input data for the interpolation of the geological features is comprised of 3D point coordinates for layer interfaces and fault surfaces, as well as measurements that indicate respective dip directions and angles. In a Python environment, the data is imported as comma-separated values (see Figures A-3 to A-5) using GemPy. From the generated data frame, GemPy is able to interpolate surfaces following the potential-field method explained in Section 2-2-2 and compute voxel-based 3D geological models (see Figure 2-14).

This model allows for the consideration of various kinds of uncertainties and their implementation in several different ways. Here, they are included by assigning uncertainties to the  $z$ -positions of points which mark layer interfaces in the 3D space. This is achieved based on respective probability distributions from which deviation values are drawn, which are then added to the original input data  $z$ -value. Uncertainties regarding layer surface positions in depth, layer thicknesses, topological shape and degree of fault offset can be incorporated. These can be assigned as homogeneous sets to groups which are to share a common degree of uncertainty. Here, points belonging to the same layer interface are assigned the same base uncertainty by applying one shared probability distribution. Assuming an increase of uncertainty with depth, standard deviations for the distributions are increased for lower formations. Furthermore, uncertainty regarding the magnitude of fault offset is incorporated by

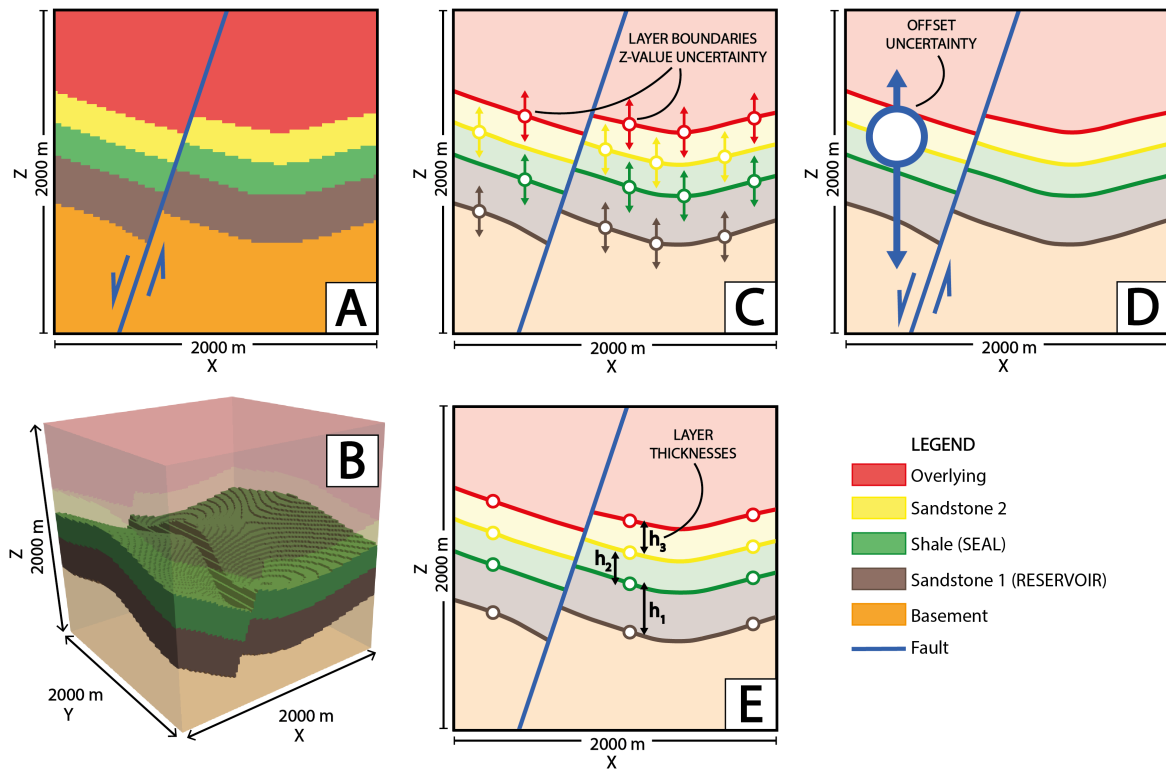


**Figure 2-14:** Illustration of the design and construction of the 3D structural geological model. A 2D cross section through the middle of the model, perpendicular to the normal fault, is shown in (A). A 3D representation of the model, highlighting the reservoir and seal formations as voxels, is visualized in (B). In (C) and (D), the inclusion of parameter uncertainties is presented. Colors indicate certain layer bottoms (i.e. boundaries) which are assigned a shared normal distribution on which their z-positional uncertainties are based (C). All points in the hanging wall are additionally assigned a fault offset uncertainty based on a skew normal distribution (D). Thicknesses of the three middle layers are defined by the distances of boundary points (E) and are thus directly dependent on (C). These thicknesses are to be defined as likelihoods.

adding a skew normal probability distribution that is shared by all layer interface points on the hanging wall. A left skewed ( $\alpha = -2$ ) normal distribution is chosen to reflect the nature of throw on a normal fault, particularly the slip motion of the hanging wall block. Mainly negative values are returned by this distribution. This way, the offset nature of the normal fault is maintained and the inversion to a reverse fault is avoided. Specific distributions used to represent uncertainties are listed in Section 3-2-1.

### 2-6-3 Determination of the maximum trap volume

In the course of this work, several algorithms are developed within the Python environment. This set of functions enables the automatic recognition and calculation of trap volumes in geological models computed by GemPy. To assign voxels of the model to the trap volume, it is checked whether the following conditions (illustrated in Figure 2-15) are satisfied by each

particular voxel:

1. **Labeled as reservoir formation:** The voxel has been assigned to the target reservoir formation (see Sandstone 1 in Figure 2-15 (1)) in the lithology block model. This is determined by respective labeling of the input data and the computation conducted by GemPy.
2. **Location in footwall:** The voxel is located on the footwall side of the fault. This condition is applicable to this specific model design, in which entrapment is assumed to occur between the footwall anticlinal enclosure and the normal fault. Due to respective dip of the reservoir formation, full leakage is assumed for the reservoir formation in the hanging wall. A distinction between foot- and hanging wall is easily achievable by using the fault model block that is generated by GemPy. In this fault block, voxels on both sides are assigned respective values for distinction.
3. **Location above spill point horizon:** The voxel is located vertically above the final spill point of the trap. In the algorithm to find this final spill point, it is distinguished between a spill point defined by the folding structure, referred to as anticlinal spill point, and a cross-fault leak point, that depends on the magnitude of displacement and the resulting nature of juxtapositions. Once both of these points have been determined, the higher one is defined to be the final spill point used to determine the maximum fill capacity of the trap. Given a juxtaposition with layers overlying the seal, due to fault displacement, the respective section is checked for fault sealing by taking into account the Shale Smear Factor value. In the case of a suitable SSF and consequent fault sealing, leakage across this type of juxtaposition is discarded as irrelevant. For simplicity, the fault is considered to be sealing along its plane. The processes of finding the decisive spill point, as well as the determination of juxtapositions and SSF is explained below in further detail.
4. **Location inside of closed system:** The voxel is part of a model section inside of the main anticlinal feature. All of the voxels inside this particular section are separated from the borders of the model by voxels that do not meet the conditions above, which primarily means that they are encapsulated by seal voxels laterally and upwards. This condition is applicable under the assumption, that connection to the borders of the model lead to leakage. A trap is thus defined as a closed system in this model and trap closure is assumed to be void outside of the space of information, i.e. the model space.

It has to be emphasized that these conditions have been fitted to the geological model constructed as described in Section 2-6-2. For other models featuring different geological properties, features and levels of complexities, these conditions might not apply at all or might have to be adapted. Models of higher complexities will surely require the introduction of further conditions.

#### 2-6-4 Finding the decisive spill or leak point of a trap

Regarding anticlinal structures and traps, it can be observed that, geometrically and mathematically, a spill point is a saddle point of the reservoir top surface in 3D. This was described

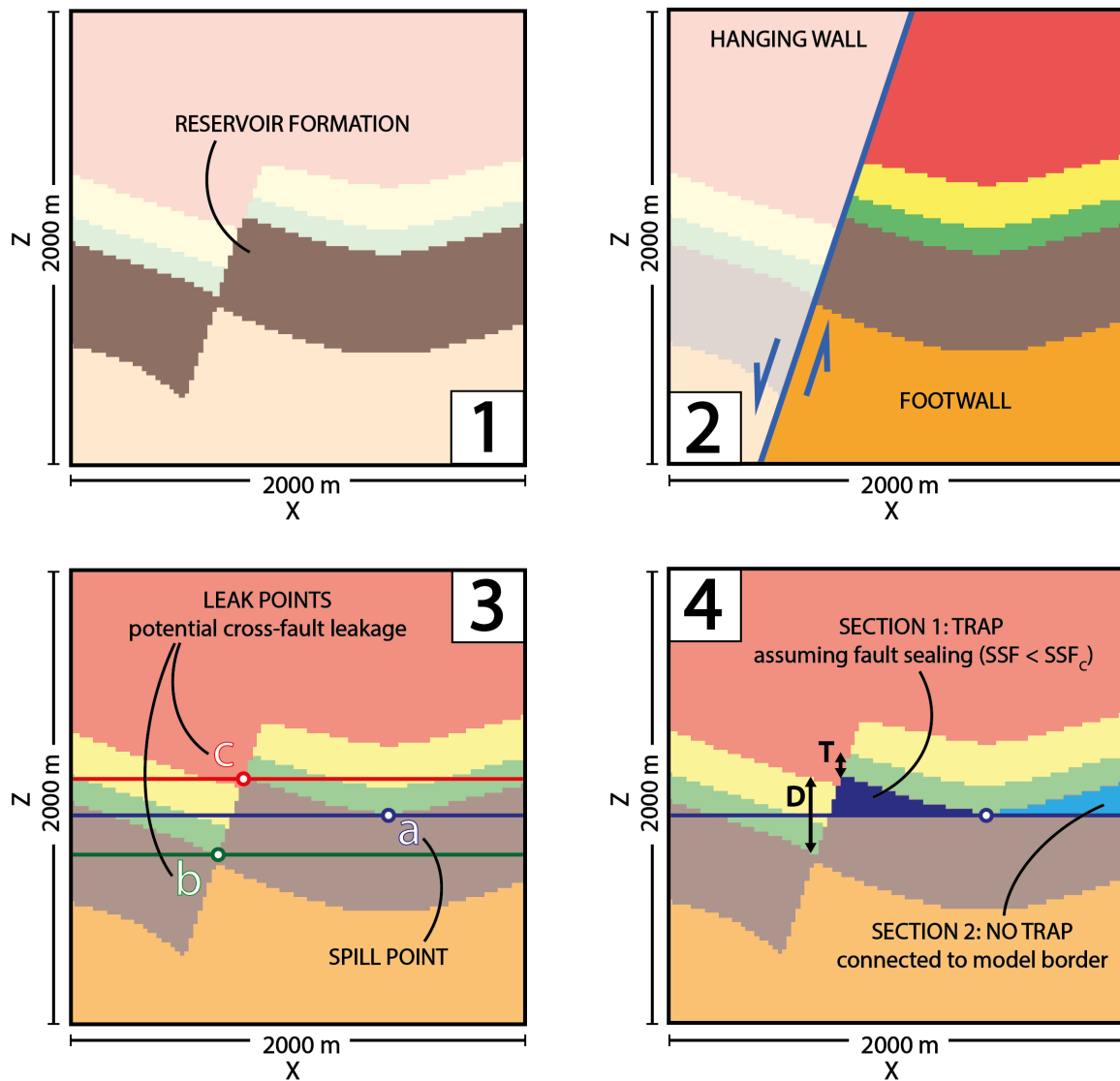


**Figure 2-15:** Illustration of the process of trap recognition, i.e. the conditions that have to be met by a model voxel, to be accepted as belonging to a valid trap. A voxel has to be labeled as part of the target reservoir formation (1) and positioned in the footwall (2). Trap closure is defined by the seal shape and the normal fault (3). Consequently, the maximum trap fill is defined by either the anticlinal spill point (3;a) or a point of leakage across the fault, depending on juxtapositions with layers underlying (3;b) or overlying the seal (3;c). The latter is only relevant if the critical Shale Smear Factor is exceeded, as determined over  $D$  and  $T$  in (4). In this example, assuming sealing of the fault due to clay smearing, the fill horizon is determined by the spill point in (4). Subsequently, only trap section 1 is isolated from the model borders in (4) and can thus be considered a closed trap.

by Collignon et al. (2015), who pointed out that the linkage of folds is given by saddle points. These are thus a controlling factor for spill-related migration from respective structural traps. For anticlinal traps, closure can consequently be defined as the distance between the saddle point (i.e. spill point) and maximal point of the trap (Collignon et al., 2015).

Regarding a surface defined by  $f(x, y)$ , a local maximum at  $(x_0, y_0, z_0)$  would resemble a hill top (Guichard et al., 2013). Local maxima will be found looking at the cross-sections in the planes  $y = y_0$  and  $x = x_0$ . Furthermore, the respective partial derivatives (i.e. gradients)  $\frac{\delta z}{\delta x}$  and  $\frac{\delta z}{\delta y}$  will equal zero at  $x_0$  and  $y_0$ , i.e. that the extremum is a stationary point (Guichard et al., 2013; Weisstein, 2017). In the context of a geological reservoir system, such a hill can be regarded as a representation of an anticlinal structural trap. Local minima are defined analogously, presenting local minima in both planes at a stationary point (Guichard et al., 2013). A saddle point, however, is a stationary point, while not being an extremum (Weisstein, 2017). In general, saddle points can be distinguished from extrema by applying the second derivative test (Guichard et al., 2013; Weisstein, 2017): Considering a 2D function  $f(x, y)$  with continuous partial derivatives at a point  $(x_0, y_0)$ , so that  $f_x(x_0, y_0) = 0$  and  $f_y(x_0, y_0) = 0$ , the following discriminant  $D$  can be introduced:

$$D(x_0, y_0) = f_{xx}(x_0, y_0)f_{yy}(x_0, y_0) - f_{xy}(x_0, y_0)^2 \quad (2-23)$$

Using this, the following holds for a point  $(x_0, y_0)$ :

1. If  $D > 0$  and  $f_{xx}(x_0, y_0) < 0$ , there is a local maximum.
2. If  $D > 0$  and  $f_{xx}(x_0, y_0) > 0$ , there is a local minimum.
3. If  $D < 0$ , there is a saddle point at the point  $(x_0, y_0)$ .
4. If  $D = 0$ , the test fails (Guichard et al., 2013).

Figure 2-16 can be seen as a representation of a point of spill between two dome structures (i.e. surface maxima or "hills") which is defined by the surface's saddle point between both. In GemPy, layer boundary surfaces are returned in the form of discretized arrays of simplices and vertices. The latter can be interpolated to a 2D rectangular grid that contains  $z$ -positional values for the surface in  $x$  and  $y$  directions. According to Verschelde (2017), a saddle point in a matrix is maximal in its row and minimal in its column. This corresponds to the logical geometrical deduction, that a saddle point for a surface defined by  $f(x, y)$  is marked by a local maximum in one plane, but a local minimum in the perpendicular plane. This is observable in Figure 2-17 and made use of in the respective algorithm in this work. Regarding leakage across the normal fault in this geological model, a similar approach is taken. The reservoir top surface can be used to find the cross-fault leak point regarding juxtapositions with layers underlying the seal. In this case, the leak point can be defined as the maximal point of the hanging wall contact of the reservoir top surface with the fault. At the same time, this point will be a local minimum on the plane perpendicular to the normal fault and thus equal a saddle point. Higher magnitudes of fault displacement can lead to detachment of the seal in the hanging wall and consequently the juxtaposition of the trap section with seal-overlying formations which are assumed to be completely permeable. This case is dealt with independently, by checking this area of juxtaposition with regard to its SSF and potential fault sealing, as is further elaborated in Section 2-6-5 below.

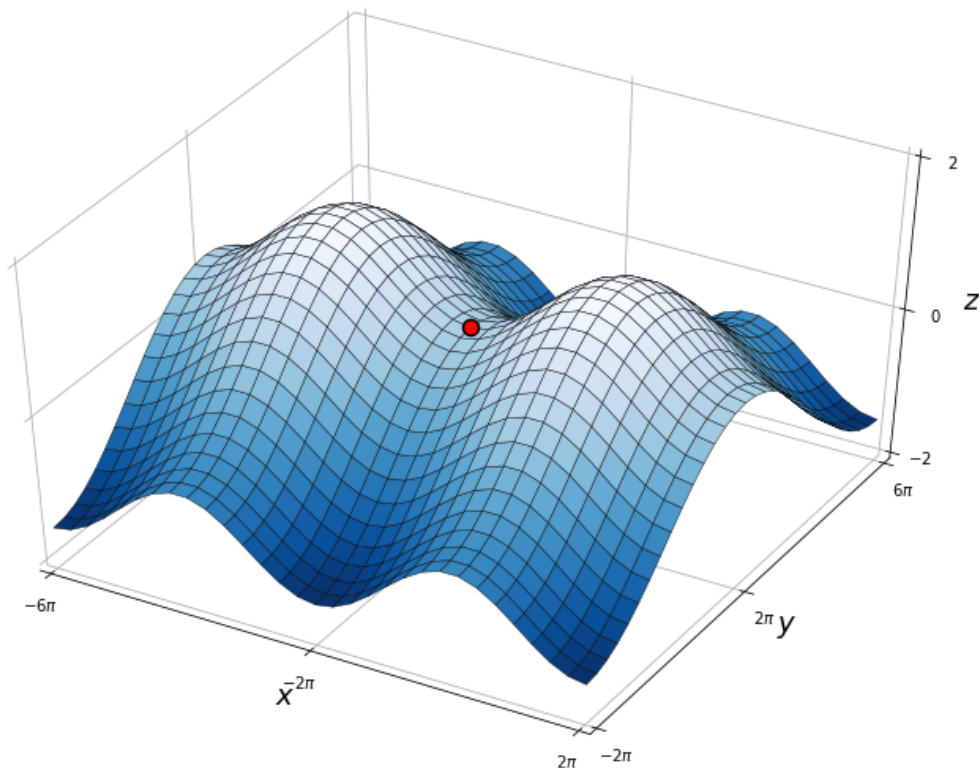


**Figure 2-16:** Saddle point (red dot) between two maxima. In a geological setting, these surface maxima may be interpreted as two dome-shaped four-way closure traps. Spill-related migration between the two structures would take place over the saddle point, i.e. the spill point.

Following these observations, the algorithm developed in this work uses a function from the Python library Scipy to find local extrema in the 2D reservoir top surface arrays attained over GemPy. This function returns the position of relative extrema in an array, by comparing every grid value with a variable number of neighbors along the same row or column. Points where local minima and maxima of perpendicular axes  $x$  and  $y$  coincide in an array, are then defined as saddle points. The anticlinal spill point is deduced as the maximal saddle point in the footwall. The cross-fault leak point is determined analogously in the hanging wall. In the end, whichever point of these two is maximal, is defined to be the decisive spill point of the trap. If no cross-fault leak point is found, it is presumed that full leakage is allowed to take place due to little or no displacement of the reservoir layer. Given only minor fault offset, no local maximum is found in the plane perpendicular to the fault. The  $z$ -value of the decisive spill point is used to determine the maximum down-to-horizon to which the trap feature can be filled.

Kuijper (2004) has pointed out that finding spatial critical points, saddle points especially, can be problematic using discretized methods and rectangular grids in particular. Finding all extrema and saddle points can be difficult (Kuijper, 2004). Failures to detect saddle points in this work's model are resolved by adding a buffer around extrema that define the anticlinal structure. However, it has to be pointed out that saddle points might still be missed in some rare cases, especially if they are located in an orientation which is "rotated" and not aligned

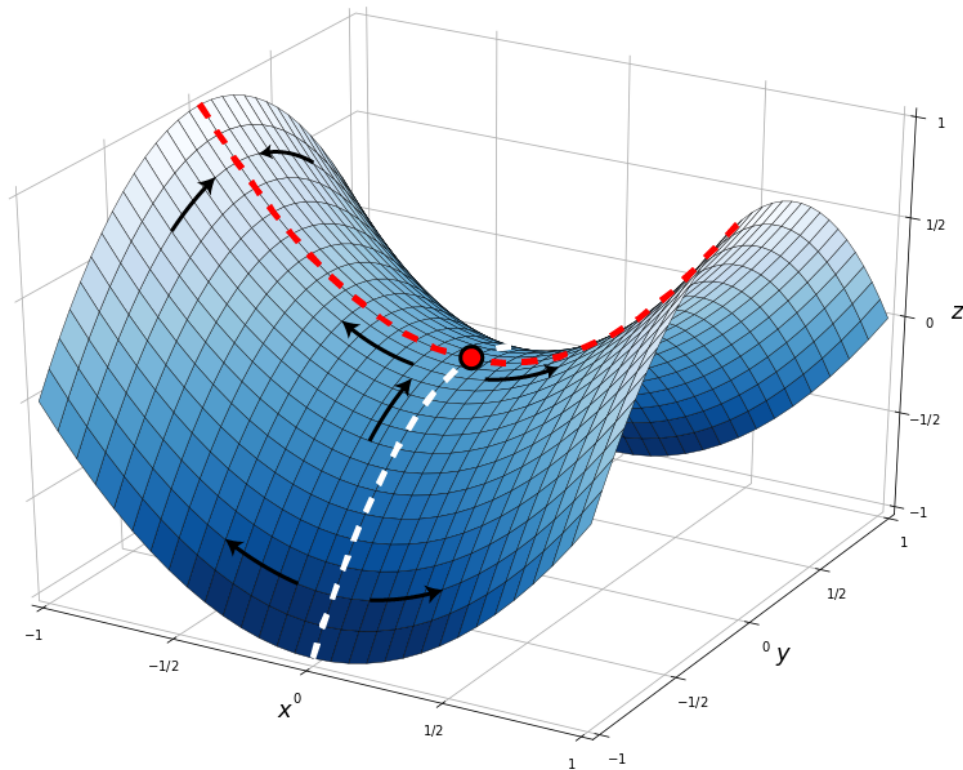


**Figure 2-17:** Surface and saddle point (red dot) generated by the function  $z = x^2 - y^2$ . Maxima in direction  $y$  is marked by a red, minima in direction  $x$  by a white dashed line. Considering the surface as a seal, consequent buoyant flow directions are indicated by arrows. Such flow would be directed away from minima and towards maxima, with the saddle point indicating a junction and divide, i.e. a possible spill point.

with the  $x$ - and  $y$  axes. Furthermore, in this work, the geological model is designed in a way that saddle points are presumed to only occur within or near the structures of interest and are thus easier to differentiate.

### 2-6-5 Checking for juxtapositions and possible fault sealing

Given a juxtaposition of a trap section with layers overlying the seal across the fault, the respective area is to be examined with regard to its clay smearing potential. Here, this is achieved by calculating the SSF as introduced in Section 2-3-2. Juxtaposition areas can be attained using a topology function that is part of GemPy. On the base of this, a new function is created, with which the  $z$ -extent, i.e. the height of relevant juxtapositions can be deduced. These are juxtapositions of all layers on which the seal slipped and seal-overlying formations. In the case of high displacement, for example, the footwall reservoir, but also the basement might be in contact with units above the seal in the hanging wall. The heights of each of these single juxtapositions, below the point of maximum displacement at the trap, are added up to attain a total juxtaposition height. Consequently, the fault throw can be attained by

adding the seal thickness to this. The resulting displacement value can then be related to the seal thickness to obtain the Shale Smear Factor.

As mentioned before, it has been reported that the critical value  $SSF_c$  is dependent on scale and can be expected to be lower with larger shale thicknesses and greater fault throws. So, as the scale in the present geological model is relatively large, but also for the purpose of shedding light on different conceptual scenarios by allowing the threshold value to be exceeded, the critical Shale Smear Factor is set to a respectively low value of  $SSF_c = 3$ . Consequently, in model realizations where  $SSF < 3$ , the fault surface on which the seal slipped, is assumed to be sealing due to clay smearing. Otherwise, for  $SSF \leq 3$ , the sealing is assumed to be breached. Due to the topological shape of the trap, full leakage is expected and the maximum trap volume is set to zero by not assigning any voxels to the trap structure.

### 2-6-6 Calculating the maximum trap volume

Have all trap voxels (fulfilling the four conditions defined above) been determined, these cells are seen as part of the maximum trap volume  $V_{trap}$ . This volume can then be calculated by simply counting the number of trap voxels and rescaling their cumulative volume depending on the resolution in which the model was computed:

$$V_{trap} = n_v * \left(\frac{S_{orig}}{R_m}\right)^3, \quad (2-24)$$

Where  $n_v$  is the number of trap voxels,  $S_{orig}$  gives the original scale and  $R_m$  the used resolution for the model. As mentioned before, we assume  $V_{trap}$  to equal the hydrocarbon-filled rock volume  $A * h$  used in Equation 2-14. For the example of a cubic geological model with an original extent of 2000 m in three directions, computed using a resolution of 100, the scale factor is 20 m. Every voxels thus accounts for  $20 \text{ m} * 20 \text{ m} * 20 \text{ m} = 8,000 \text{ m}^3$  in volume. It has to be noted, that this direct approach to rescaling and calculating the volume requires the model to be designed as a cubic block.

### 2-6-7 Implementation of reservoir-related likelihoods in the 3D model

As for the 1D case before, for the 3D case we also assume that additional information is provided in the form of layer thickness likelihoods. In this geological scenario, the information might have been gained for example from additional seismic observations or from data from a drilling well nearby. Likelihoods could also be derived from knowledge of the geological history of the formation, such as the depositional environment of sedimentary layers. Assuming a possible correlation of nearby core samples with the layers in our model section, layer thickness likelihoods can be defined respectively as normal distributions.

First of all, a method to determine layer thicknesses in the geological model realizations has to be introduced. Here, as single  $x$ - and  $y$ -point, i.e. a 1D column in  $z$  in the footwall of the model is chosen as a measure for the thickness of the layers. In this column, point coordinates for the layer interfaces had been defined in the original data frame and can be observed as they are altered in the interpolation data frame with each probabilistic modeling iteration. Thicknesses are simply calculated as the distance between two layer boundary points in this column. Variations in thicknesses can be traced and vary relative to the changes in

the layer interface positions, defined by the uncertainties in their  $z$ -values. At  $x = 1100$  m and  $y = 1000$  m, the point of measurement is located centrally in the overall model block, as well as the original potential trap structure, and is thus presumed to be of representative significance for the reservoir analysis.

After defining these thickness to point-positional dependencies, thickness likelihood functions are implemented based on probability distributions, as done for the 1D model. Various types of geological information, conclusions and expectations can be expressed by adapting mean and standard deviation of these normal distributions. For core sampling, for example, information might be evenly provided for all layers, irrespective of depth, so that similar degrees of standard deviation might be assigned to all layer thicknesses. Alternatively, taking into account certain depositional environments for which high thickness variability is characteristic, specific standard deviations can be raised accordingly.

We additionally consider a likelihood function related to the Shale Smear Factor. This function is based on a normal distribution as well. As the SSF is a more complex derivate of parameter relations, it also more difficult to argue, how respective observations were sourced. Related knowledge about fault displacement and thicknesses in an area nearby, would come with respective likelihood functions for those parent parameters as well. Possibly, the additional information about the SSF was acquired indirectly, for example by having tested the leakage potential of other faults in the same general region. The inclusion of these likelihood functions is based on purely hypothetical assumptions and is intended to provide the opportunity, to explore the effects different types of information might have. While the thickness likelihood functions are dependent on input parameters directly, the implementation of the SSF likelihood function requires a full computation of the model and extended algorithms of structural analysis.

Some representative cases of Bayesian inference applied to the 3D model are presented in Chapter 3.

## 2-6-8 Bayesian analysis and evaluation for the 3D geological model

According to the methods introduced in Sections 2-1 and 2-2, the 3D geological model is to be incorporated in a probabilistic modeling framework and analyzed from a Bayesian perspective. First, we conduct a simple Monte Carlo simulation considering only priors, so that a base reference distribution for the original model is generated. Subsequently, Bayesian inference is conducted based on different assumptions concerning the additional observations made and by incorporating likelihoods which respectively are designed to reflect the nature of this auxiliary data. Posterior distributions, in particular resulting volume distributions, can then be examined and evaluated by applying the methods described in Section 2-3. Furthermore, for every simulation, the mechanisms which ultimately determined the trap closure in every iteration, such as the spill point and cross-fault leakage, are traced as trap volume controls factors.

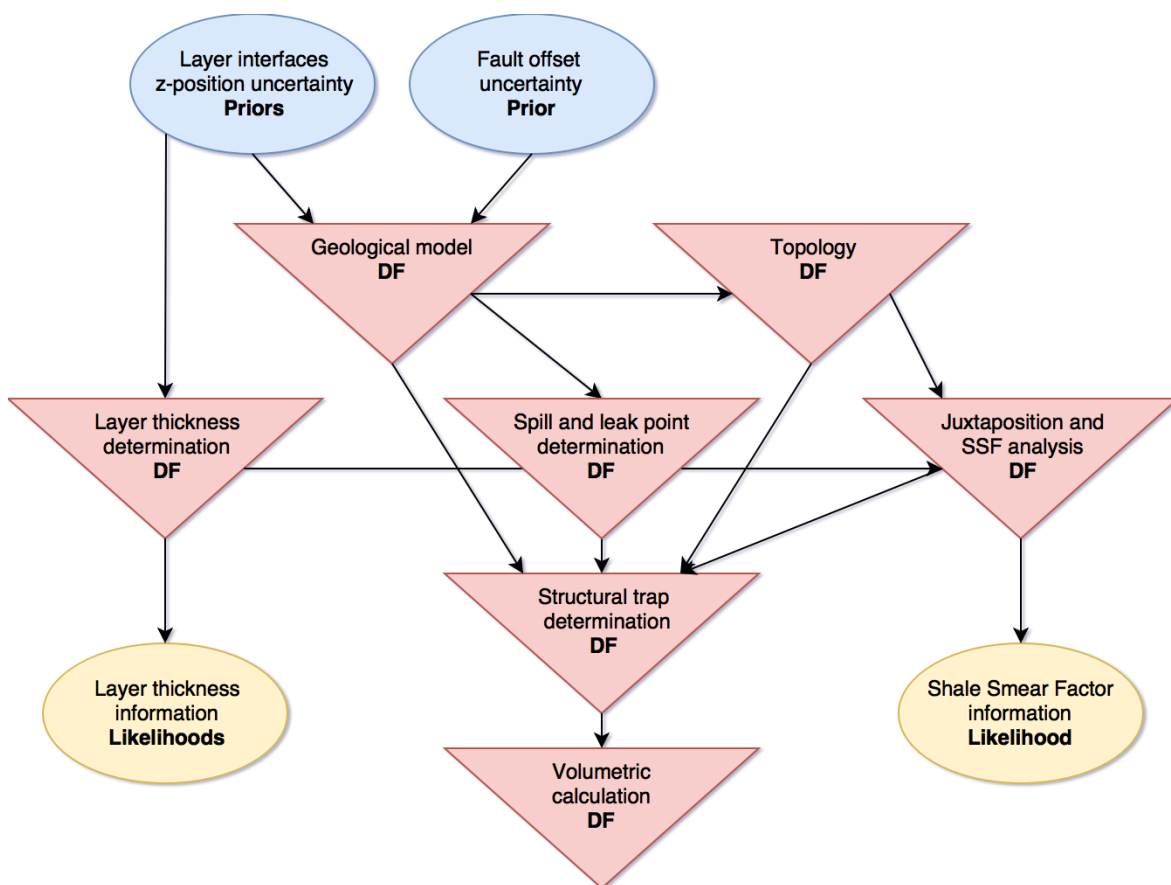


**Figure 2-18:** Illustration of our probabilistic model (3D) as a hierarchical Bayesian network after Koller and Friedman (2009). *Stochastic* nodes are represented by ellipses (blue for priors, yellow for likelihoods). *Deterministic* functions are depicted as triangles in red. Arrows indicate direct connections from parent to child nodes. We included the most important functions that contribute to the automatic trap recognition and volumetric calculation in our structural geological model.

---

# Chapter 3

---

## Results

### 3-1 1D geological reservoir model results

c

#### 3-1-1 Scoring

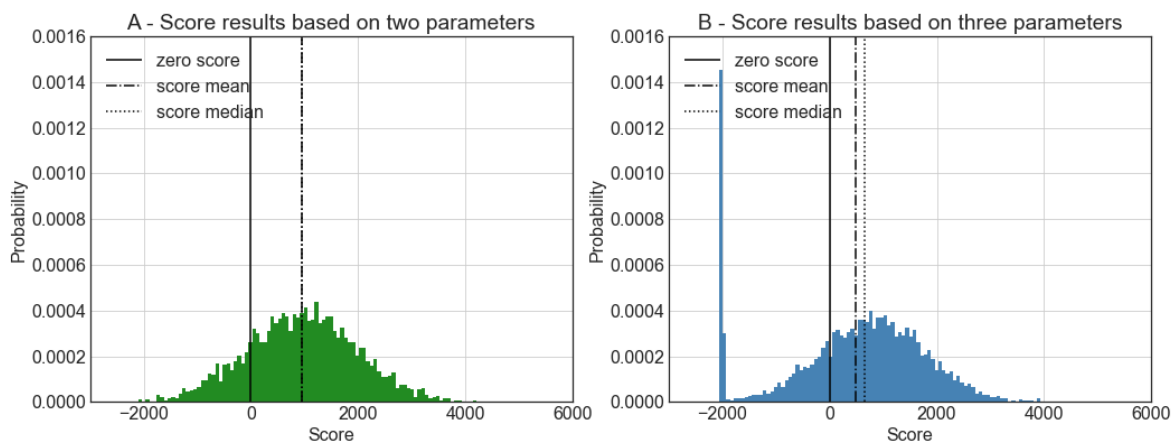


**Figure 3-1:** Posterior probability distributions from modeling scores using two (A) and three parameters (B) (reservoir thickness, reservoir top depth and seal thickness with a safety threshold of 20 m).

Results from scoring based on simple Monte Carlo error propagation (10000 iterations) using only the priors of the 1D model (as defined in Section 2-5-1) are plotted in Figure 3-1. A test run of scoring with only the two parameters reservoir thickness and depth, is shown in Figure 3-1 (A). These results are represented by an approximately normal distribution. The score is negative in about 17% of the cases. Mean and median are about the same. Full scoring results, including also seal reliability (with a threshold of 20 m) as a parameter,

are visualized in Figure 3-1 (B). The main distribution is not changed significantly, except for a striking peak of probability at the possibility for a score of -2000. This presumably represents the bulk of cases in which the seal is assumed to have failed. Regarding this, it is to be noted, that the mean of the seal top distribution is found at -2000 m. It can be seen in Figure 3-3 (A1), that around that depth in the model column, reservoir top and seal top probability distributions significantly overlap. Thus, there is a possibility for a higher score, due to a shallower reservoir top position, but also a high probability for a seal thickness below the safety cut-off threshold of 20 m. The negative score peak at -2000 is thus presumably caused by a high number of seal failures, due to both layer interfaces located within this range. Furthermore, as a consequence of this negative peak, mean and median of the score distribution have been shifted to lower values and are now found further apart (see Figure 3-1 (B)).

Using this prior score distribution as a base, the custom loss function including risk was applied (see Figure 3-2). It can be observed that the minima for expected loss, i.e. the Bayesian estimators for differently risk-affine actors, are located at different estimates. Mean and median of the score distribution are clearly surpassed by the best estimate of the most risk-friendly actor ( $r = 0.5$ ), while for the most risk-averse actors ( $r = 1.25$  and  $r = 1.5$ ), the Bayes action equals a zero score estimate and thus the decision to take no action. It can also be recognized that the expected loss is generally lower for risk-friendlier actors on the side of positive estimates, which in this case is the relevant side for decision making.

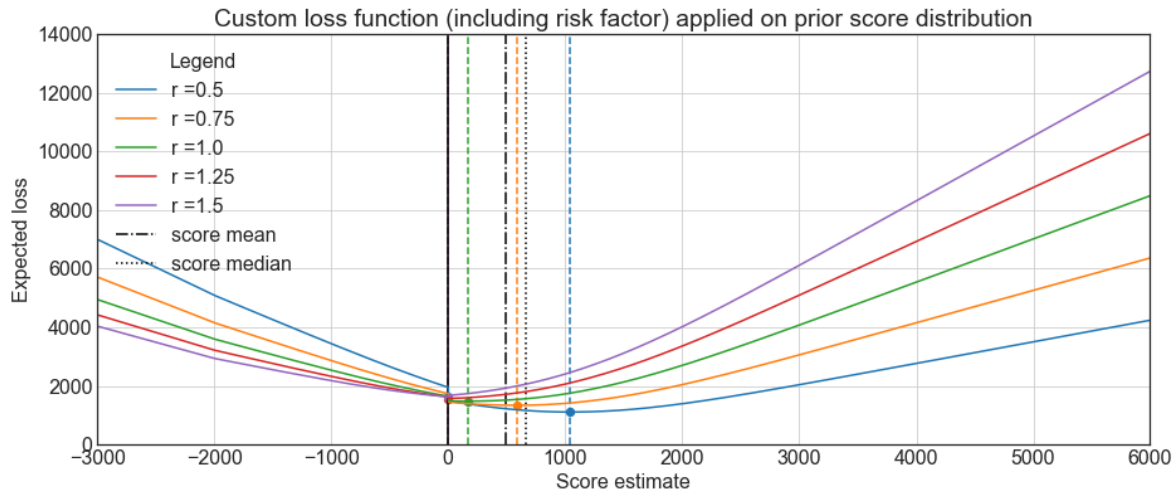


**Figure 3-2:** Plotting of expected loss realizations after including the risk factor  $r$  in the loss function for actors with risk-affinities ranging from risk-averse ( $r = 0.5$  and  $0.75$ ), over risk-neutral ( $r = 1$ ), to risk-friendly ( $r = 1.25$  and  $r = 1.5$ ), based on the application of the custom loss function (Equation 2-21) on a prior score distribution (see Figure 3-1 (B)) from simple Monte Carlo error propagation.

### 3-1-2 Bayesian inference using thickness likelihood functions

Three representative Bayesian updating cases (10000 iterations; burn-in phase of 1000 iterations) based on different sets of likelihoods (see Table 3-1) in the 1D model are presented in the following. In each case, the layer boundaries defined in Section 2-5-1 were adopted as

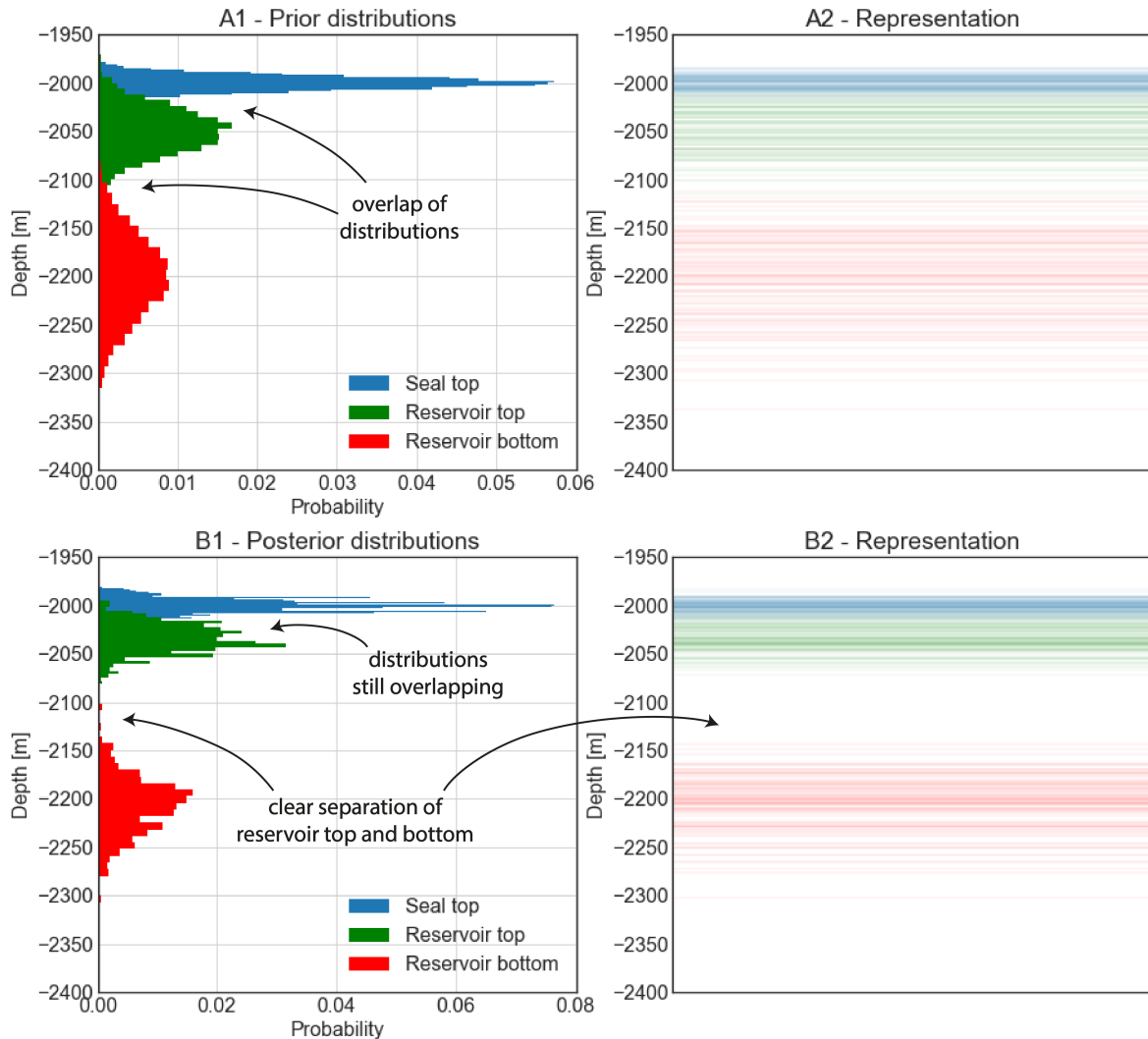


**Figure 3-3:** Prior (A1) and posterior distributions (A2) of the layer boundary positions in depth and respective representations (A2, B2). Bayesian inference was conducted using likelihoods defined as follows: Seal thickness:  $\mu = 25 \text{ m}; \sigma = 20 \text{ m}$ ; reservoir thickness:  $\mu = 180 \text{ m}; \sigma = 40 \text{ m}$ . From (A1) to (B1), the distributions are slightly narrowed. Seal top and reservoir top distributions are still overlapping in (B1). A moderate reduction in uncertainty is also indicated by the representation in (B2), compared to (A2).

prior parameters. The various results from modeling with likelihoods, i.e. applying Bayesian inference, are compared to the original results and evaluations based on simple Monte Carlo error propagation using only priors.

(a) Inference case I - Likelihoods: Layer thicknesses (normal distributions)		
	$\mu$ [m]	$\sigma$ [m]
Formation bottom		
Seal	25	20
Reservoir	180	40
(b) Inference case II - Likelihoods: Layer thicknesses (normal distributions)		
	$\mu$ [m]	$\sigma$ [m]
Formation bottom		
Seal	50	20
Reservoir	180	40
(c) Inference case III - Likelihoods: Layer thicknesses (normal distributions)		
	$\mu$ [m]	$\sigma$ [m]
Formation bottom		
Seal	70	10
Reservoir	100	30

**Table 3-1:** Thickness likelihoods defined by normal distributions, as used for the three inference cases of the 1D model.

### 1D - Inference case I: Moderately reinforcing information

As can be observed in Figure 3-3, the uncertainty in the probability distributions for the positions of layer boundaries in depth was reduced moderately by implementing the likelihoods defined in Table 3-1 (a).

Scoring was applied based on these new distributions. In Figure 3-4 (A), it can be recognized that the bulk of the score distribution was shifted to the positive side of values and narrowed, approximately resembling a normal distribution there. However, the peak at -2000 was raised, while the probability of scores between -2000 and 0 was decreased to be negligible, i.e. the true score is most likely either positive or -2000, if it is negative. So while uncertainties were reduced in areas of opposite sign, the divide between these was significantly increased. The overall uncertainty seems thus to have been widely maintained and barely transformed into a problem of duality.

Application of the custom loss function (Equation 2-21) is visualized in Figure 3-4 in which the expected losses are compared before (B1) and after (B2) inference. It is observable, that by adding information about layer thickness likelihoods, Bayes actions were shifted relative to the nature of the information. In this case, the added data generally reinforced the probability of the reservoir to be sufficiently thick. Information on the seal, however, based on a normal distribution around 25 m thickness, left high uncertainty about the reliability of the seal, as the safety threshold was defined to be 20 m. Consequently, the risk of complete seal failure remained a major concern.

Increased certainty about the reservoir thickness was sufficient to shift Bayes actions to

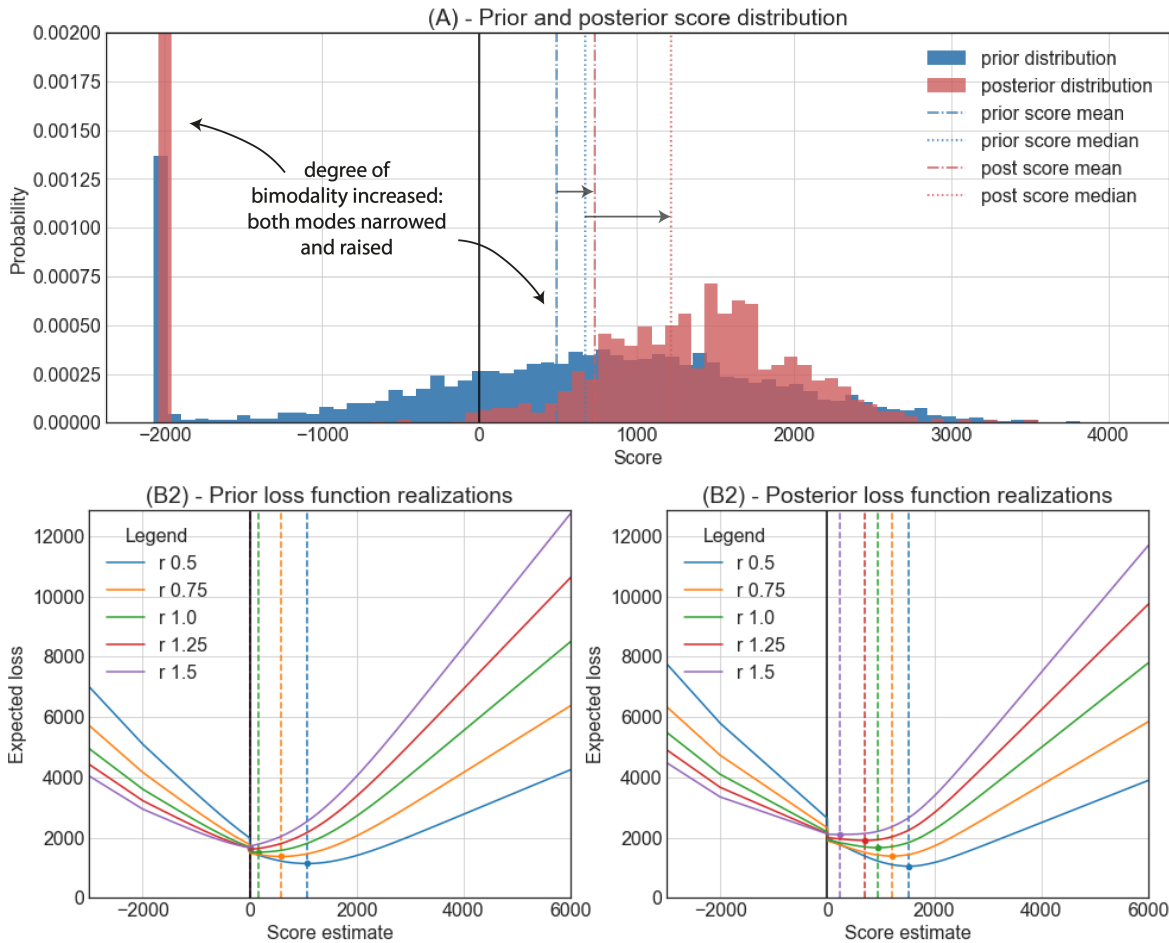


**Figure 3-4:** 1D - Inference case I. Reservoir score distributions (A) and change in the realizations of expected loss for several risk parameters (B1, B2) before and after Bayesian updating based on likelihoods defined as follows: Seal thickness:  $\mu = 25 \text{ m}$ ;  $\sigma = 20 \text{ m}$ ; reservoir thickness:  $\mu = 180 \text{ m}$ ;  $\sigma = 40 \text{ m}$ .

higher estimates for all actors. Estimators of the more risk-neutral actors ( $r = 0.75$  to  $r = 1.25$ ) were increased the most. This has led to a slight convergence of the Bayes actions. For the risk-neutral actor, change in expected loss was negligible. For risk-friendlier actors, the expected loss was decreased, but for risk-averse actors, as they shifted from zero ("take no action") to positive estimates, increased.

### 1D - Inference case II: Likely reliable seal

In this second case, the reservoir thickness likelihood was defined in the same way as in case I (see Table 3-1). For the seal, a higher mean of 50 m chosen, favoring the likelihood of a safe thickness relative to the threshold of 20 m (see Figure A-1). Respective score results are depicted in Figure 3-5 (A). The bulk of the distribution is narrowed on the positive side of estimates. Very apparent is the significant diminishment of the "seal failure peak" at -2000.

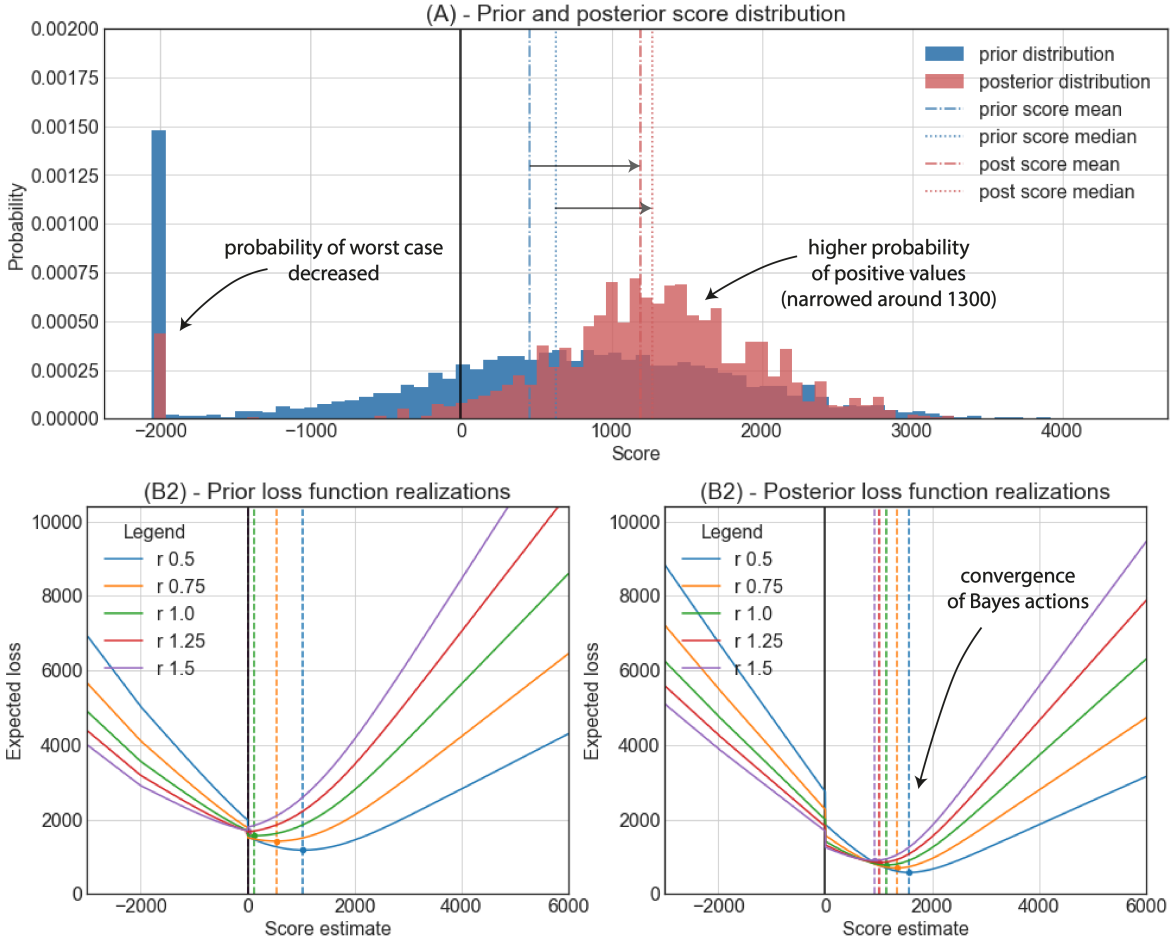


**Figure 3-5:** 1D - Inference case II. Reservoir score distributions (A) and change in the realizations of expected loss for several risk parameters (B1, B2) before and after Bayesian updating based on likelihoods defined as follows: Seal thickness:  $\mu = 50 \text{ m}$ ;  $\sigma = 20 \text{ m}$ ; reservoir thickness:  $\mu = 180 \text{ m}$ ;  $\sigma = 40 \text{ m}$ .

Due to this, in combination with the overall distribution narrowing, mean and median were clearly shifted to higher values and are now much closer together.

Applying the custom loss function to this new score distribution resulted in the realizations of expected loss illustrated in Figure 3-5. Bayes actions were shifted clearly to higher estimates and expected losses of these minima were significantly reduced for all actors. The risk-neutral to risk-averse individuals seem to have profited the most, due to a large change in estimator value and decreased expected loss (Bayes risk). Compared to the foregone case, a higher degree of overall uncertainty reduction was achieved. The risk of seal failure is now much lower. Consequently, Bayes actions were not only shifted to greater values, but also narrowed significantly in their range, i.e. the optimal decisions of the different actors have converged to a much greater extent than in case I.

### 1D - Inference case III: Safe seal but likely subpar reservoir thickness

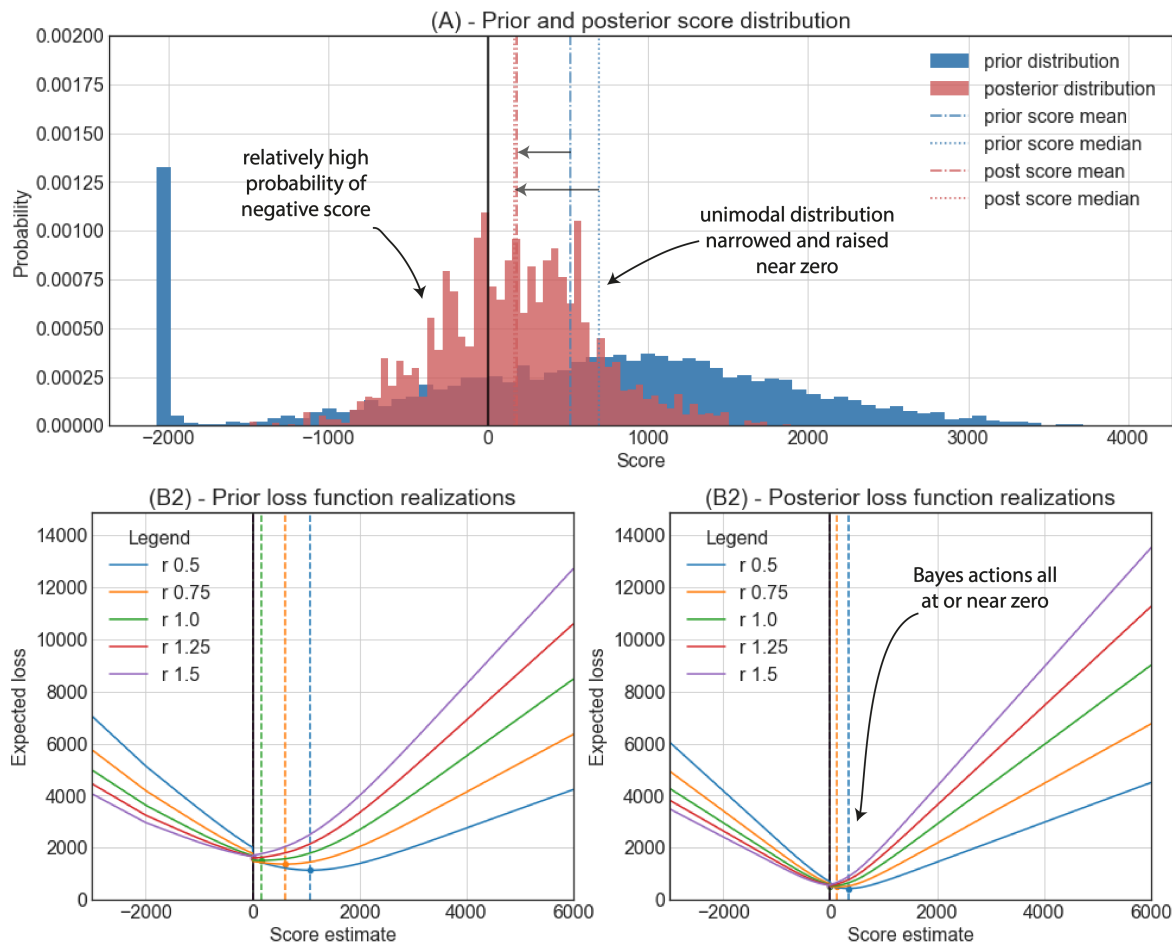


**Figure 3-6:** 1D - Inference case III. Reservoir score distributions (A) and change in the realizations of expected loss for several risk parameters (B1, B2) before and after Bayesian updating based on likelihoods defined as follows: Seal thickness:  $\mu = 70 \text{ m}$ ;  $\sigma = 10 \text{ m}$ ; reservoir thickness:  $\mu = 100 \text{ m}$ ;  $\sigma = 30 \text{ m}$ .

In this third case, seal safety was ensured by using a mean of 70 m with a standard deviation of 10 m for the seal thickness likelihood. However, the new observations were assumed to provide information about the reservoir unit that makes it likely to be thinner than priorly expected (see Table 3-1 (c) and Figure A-2)

The subsequent score distribution is depicted in Figure 3-6 (A). It can be seen that while the whole distribution was strongly narrowed, it also was shifted to lower and negative estimates. Mean and median are almost equal, indicating narrowing towards symmetry in the shape of a normal distribution. As seal reliability was practically guaranteed, the peak at -2000 vanished.

Based on this posterior score probability distribution, Bayes actions were shifted to lower estimates for all actors (see Figure 3-6 (B2)). The risk-neutral and both risk-averse individuals find their Bayesian estimators to be zero after updating, i.e. bidding on a positive score is deemed to be too risky to them. There is no shift in estimate for risk-averse actors, as they

already found their best estimates to be zero before updating. Notable is the large reduction of expected loss (Bayes risk) in general. The range of Bayes actions was significantly narrowed. Overall, it is apparent that uncertainty was greatly reduced (see the narrowed distribution). However, although the seal can now be expected to be safe, the reservoir thickness is likely subpar. Due to this, the distribution was shifted to lower and negative values, strongly increasing the probability of an unfavorable true score. Consequently, only risk-friendly actors are willing to take action.

## 3-2 3D geological reservoir model results

In the following, we present the results from applying the methods to the synthetic 3D structural geological model. Several representative examples of posterior models based on the use of different likelihoods are referenced to the original prior model. For each simulation, 1,000 sampling steps were conducted, with a burn-in phase of 50 iterations for MCMC sampling. For computational reasons, Shannon entropy visualization was based on 200 sampling steps and a burn-in phase of 50 iterations. Convergence diagnostic results (Geweke and trace plots for the uncertain priors) can be found in the Appendix (Figures A-7 to A-11). Considering that the majority of Z-score points in the Geweke plot are found within two standard deviations around zero, we deem that suitable convergence was achieved for the purpose of this work. For the comparison of results, we consider in particular the following measures: (1) Shannon entropy, (2) occurrence of trap control mechanisms, (3) resulting recoverable oil volumes and (4) consequent realization of expected losses and related Bayes actions (i.e. decisions).

### 3-2-1 3D - Prior model

To generate a set of reference results, a prior model was first generated by running a simple Monte Carlo simulation considering only the uncertainty of prior parameters. No likelihood functions were included. The prior parameter uncertainties (defined in Table 3-2) were chosen to be identical for all posterior simulations.

The nature of the prior uncertainties was visualized using Shannon entropy (see Figure 3-8 (a)). High entropies can be seen at and near the possible locations of layer boundaries. This effect was strongly amplified by the offset uncertainty in the footwall, where the highest entropies are found.

The occurrence of the different mechanisms of maximum trap control were traced for all simulations and labeled as follows:

1. **SPILL POINT:** Migration related to the anticlinal spill point of the trap.
2. **LEAK UNDER:** Leakage due to juxtaposition of the reservoir with formations underlying the seal in the hanging wall.
3. **LEAK OVER:** Leakage due to juxtaposition of the reservoir with formations overlying the seal in the hanging wall. This was defined to lead to full leakage and complete failure of the trap.

---

(a) Uncertainty: Layer boundaries $z$ -position (normal distributions)		
Formation bottom	$\mu$ [m]	$\sigma$ [m]
Overlying	0	40
Sandstone 2	0	60
Shale (Seal)	0	80
Sandstone 1 (Reservoir)	0	100
<hr/>		
(b) Uncertainty: Normal fault offset (skew normal distribution)		
Fault side	$\mu$ [m]	$\sigma$ [m]
Hanging wall offset	0	- 150
		- 2

---

**Table 3-2:** Prior parameter uncertainties defined by distributions with respective means  $\mu$ , standard deviations  $\sigma$  and shape factor  $\alpha$ , as used in all model simulations (3D). Points belonging to the same layer interface share the same normal distribution (a). The offset uncertainty (b) is based on a skew normal distribution that affects all positional points in the hanging wall.

4. **STRAT:** Leakage due to stratigraphical connections of the trap to seal-overlying units, i.e. stratigraphical breaches of the seal. Full leakage and trap failure were assumed for this mechanism as well.
5. **UNCLEAR:** Label defined to track cases in which a mechanism was not recognized. This is deemed an indicator for failures of the algorithms or the computation, i.e. the reliability of the overall model and incorporated functions.

It is shown in Figure 3-8 (c) that all four relevant mechanisms occurred for the prior model. The dominant factor is the anticlinal spill point accounting for more than 60% of model realizations. It is followed by cross-fault leakage labeled "LEAK UNDER" ( $\sim 20\%$ ) and "LEAK OVER" ( $\sim 13\%$ ). Stratigraphical breaches of the seal were registered to be decisive in only about 3% of iterations. A satisfactory reliability of model algorithms and computation is indicated by the lack of unrecognized mechanisms.

Recoverable oil volumes were calculated for each model iteration and plotted as a probability distribution in Figure 3-7 (a). It can clearly be seen that while a large portion of the distribution is found in a range of highly positive volumes, forming a normal distribution shape around 3.8 million m<sup>3</sup>, there is also a high probability of complete failure, i.e. for the trap volume to be zero. This results in a bimodal characterization with low probability of the ROV to be found between zero and 3 million m<sup>3</sup>.

Consequently, applying the custom loss function to this distribution resulted in divergent Bayes actions for the differently risk-affine actors (see Figure 3-7 (b)). Although all actors find their estimators to be positive, only the risk-neutral to risk-friendliest actors come close to the described positive mode of the distribution (ROV > 3\*10<sup>6</sup> m<sup>3</sup>). Risk-averse individuals bid on significantly lower estimates. It can also be observed that expected losses resulted to be generally lower for risk-affine actors. It can be presumed that the divergence of different Bayes actions was caused by the bimodality of the ROV probability distribution.

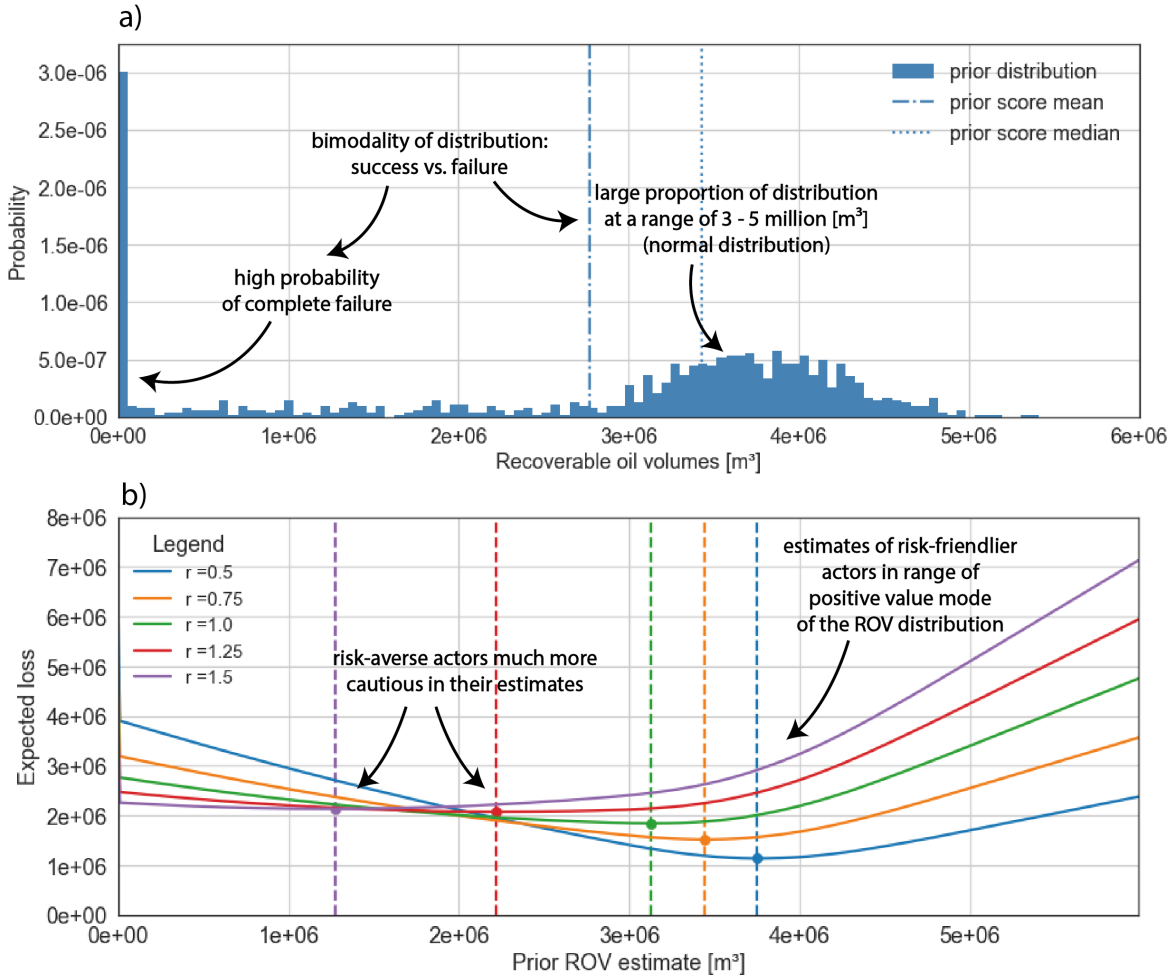


**Figure 3-7:** Recoverable oil volumes probability distribution for the prior 3D model (a) and respective realization of the custom loss function (b).

### 3-2-2 3D - Posterior model I: Seal and reservoir likely thick

For the simulation of this first posterior model, we included thickness likelihoods for the three central layers in the probabilistic model. These were defined in a way that reinforced the probabilities of the relevant layers to be significantly thick (see Table 3-3). Respective results are summarized in Figure 3-8.

Considering the changes in Shannon entropy, it can be seen that the uncertainty about layer interface positions in  $z$  was clearly reduced in the footwall. Information entropy was also decreased in the middle section of the hanging wall, but remained high in upper and lower parts, presumably due to the remaining influence of the offset uncertainty.

Regarding trap volume control (Figure 3-8 (c)), only spill point-related migration ("SPILL POINT") and cross-fault leakage due to juxtaposition with permeable layers below the seal in the hanging wall ("LEAK UNDER") remained relevant in the posterior model. As no occurrences of leakage through overlying layers were observed, these two main mechanisms increased in frequency while staying proportionally the same to one another. It can be presumed that by introducing the respective likelihoods, a high thickness of the seal was ensured,

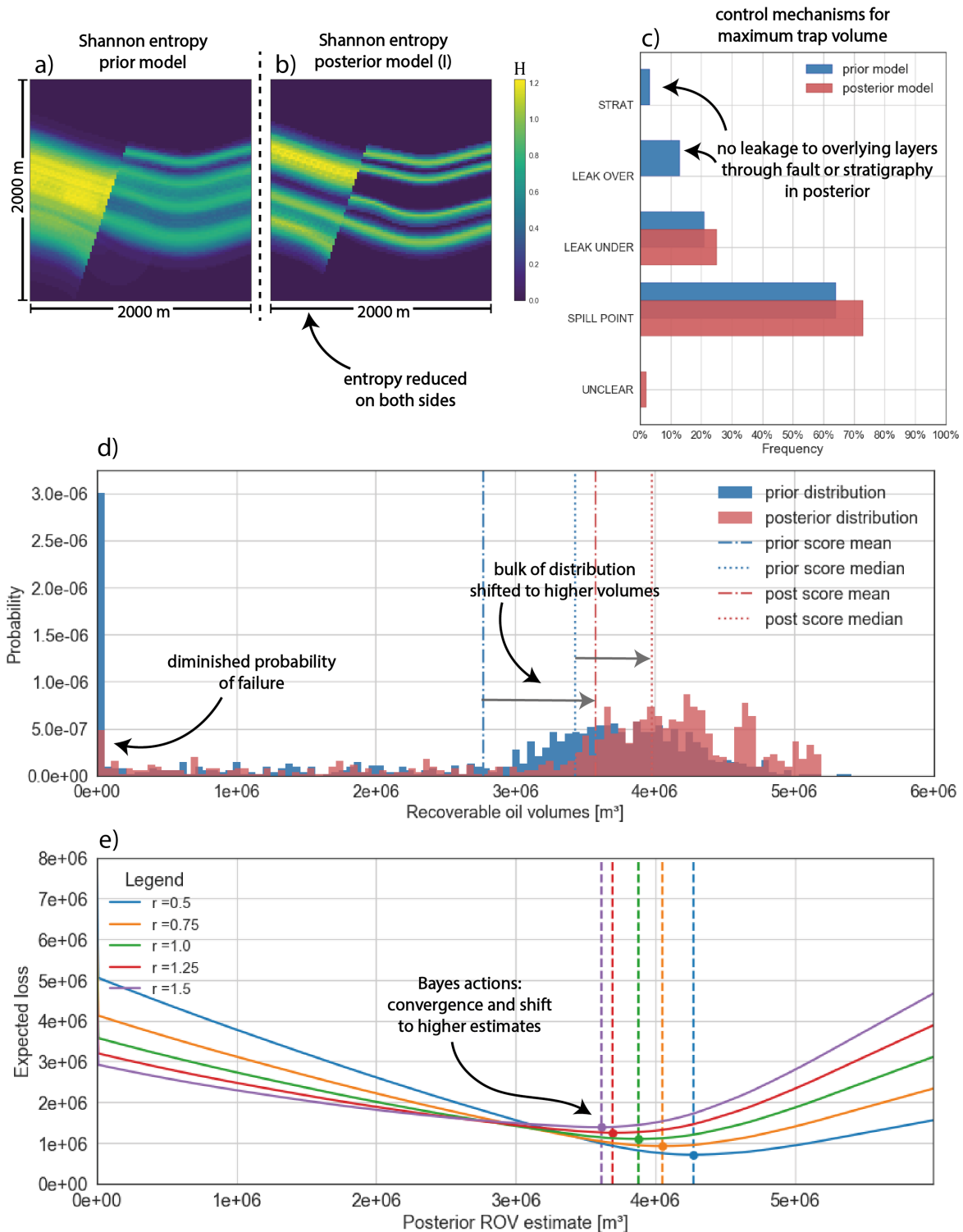


**Figure 3-8:** Summary of results from evaluating posterior model I (3D). Shannon entropies in prior (a) and posterior (b) are compared. So are the mechanisms of maximum trap volume control (c). Prior and posterior ROV probability distributions are shown in (d). Respective loss function and Bayes actions are plotted in (e).

---

Model I - Likelihoods: Layer thicknesses (normal distributions)		
Formation	$\mu$ [m]	$\sigma$ [m]
Sandstone 2	150	30
Shale (Seal)	350	30
Sandstone 1 (Reservoir)	250	30

---

**Table 3-3:** Layer thickness likelihoods determined by normal distributions as used for posterior model I (3D).

as can also be recognized in Figure 3-8 (b). This not only made stratigraphic leakage in this model impossible but also enforced a favorable SSF. A minor emergence of unrecognized control factors ("UNCLEAR") suggests that, for a few iterations, the model was possibly not correctly computable or the structural analysis failed for a different reason.

The bulk that accounted for the positive mode in the prior ROV distribution was raised and shifted laterally to higher values, while the probability of failure ( $ROV = 0$ ) was diminished significantly (see Figure 3-8 (d)). This can presumably be explained by the disappearance of leakage to overlying formations as a trap control mechanism, which was programmed to always lead to complete failure of the trap volume.

As the probability of failure and thus the bimodality of the probability distribution were diminished, all Bayes actions were shifted to higher estimates, most significantly those of the two risk-averse individuals (see Figure 3-8 (e)). These have thus converged into an area of similar expectations. Additionally, expected losses (Bayes risks) were lowered overall. The posterior state of knowledge, provided by the updated model, encouraged even the most risk-averse decision maker to expect recoverable oil volumes from 3.5 million m<sup>3</sup> upwards.

### 3-2-3 3D - Posterior model II: Likely thin reservoir formation

---

Model II - Likelihoods: Layer thicknesses (normal distributions)		
Formation	$\mu$ [m]	$\sigma$ [m]
Sandstone 2	300	30
Shale (Seal)	400	40
Sandstone 1 (Reservoir)	50	10

---

**Table 3-4:** Layer thickness likelihoods determined by normal distributions as used for posterior model II (3D).

For the second model, thickness likelihoods were defined in a way that reinforced the probability of a very thick seal but at the same time restricted the reservoir formation to a likely significantly thinner thickness of around 50 m (see Table 3-4). The results (see Figure A-6 in the Appendix) are very similar, in fact almost identical, to those of model I above. This can be explained by the influence of leak and spill point. As the shape of the general structure itself was not defined to be uncertain, the position of the anticlinal spill point relative to the fault top remains mostly unchanged, irrespective of layer thickness variations. Thus, reservoir thickness is only a secondary factor to trap volume control. Assuming fixed values for

all other parameters, the maximum fill horizon is most likely the same for a 300 m as for a 50 m thick reservoir unit. The thickness of the reservoir only becomes significant, if it is thin enough to locate the respective layer bottom above the leak and spill point depth in the trap section. Ultimately, the spill point appears to be the primary limiting factor to maximum trap fill. It can furthermore be derived from this that the maximum trap volume potential, as defined by the given structural features, is already represented in the ROV probability distribution of the prior model. After examining Figure 3-8 (d), it seems that this overall maximum volume is found at approximately 5.7 million m<sup>3</sup>. Higher values were not observed in any other model realization and are presumed to be unattainable due to the restriction given by the spill point.

### 3-2-4 3D - Posterior model III: Likely thin seal

Model III - Likelihoods: Layer thicknesses (normal distributions)		
Formation	$\mu$ [m]	$\sigma$ [m]
Sandstone 2	300	30
Shale (Seal)	50	10
Sandstone 1 (Reservoir)	400	30

**Table 3-5:** Layer thickness likelihoods determined by normal distributions as used for posterior model III (3D).

Using likelihoods which favor a thick reservoir but only a thin seal of about 50 m thickness (see Table 3-5), leakage due to juxtaposition with seal-overlying formations across the fault ("LEAK OVER") became the primary mechanism for trap volume control (see Figure 3-9 (c)). It can be recognized in Figure 3-9 (b) that, while uncertainty was reduced clearly in the footwall, it remained high in the hanging wall. The Shannon entropy visualization furthermore suggests that the seal layer frequently appeared significantly deeper in the hanging wall than in the footwall. Combined with a generally very thin seal, this allowed for the occurrence of high displacement to seal thickness ratios, i.e. a high SSF. Thus, frequent surpassing of the critical SSF and subsequent fault seal breaching were enabled. It is additionally apparent in Figure 3-9 (b), that while fault-related leakage became predominant, control by the spill point was suppressed to be widely irrelevant in this posterior model.

A dramatically higher probability of complete trap failure was induced by the high frequency of cross-fault leakage to overlying formations. Consequently, the bulk of the posterior ROV probability distribution was shifted to a volume of zero, as depicted in Figure 3-9 (d). Any positive trap volumes have become highly improbable.

Bayes actions changed accordingly. Given this posterior ROV distribution, all actors find their minimum of expected loss at ROV = 0, which equals the decision to "take no action" (see Figure 3-9 (e)). It has to be pointed out that all Bayes actions are found at the same point due to the lack of negative values into which more risk-averse actors would presumably have moved, given the possibility. This poses a difference to the score system implemented for the 1D geological model evaluation. As volumes cannot be negative, Bayes actions cannot be shifted past the limit of ROV = 0. Compared to the prior model, expected losses decreased overall, but are higher for risk-friendlier individuals at the minimum. Results from this third

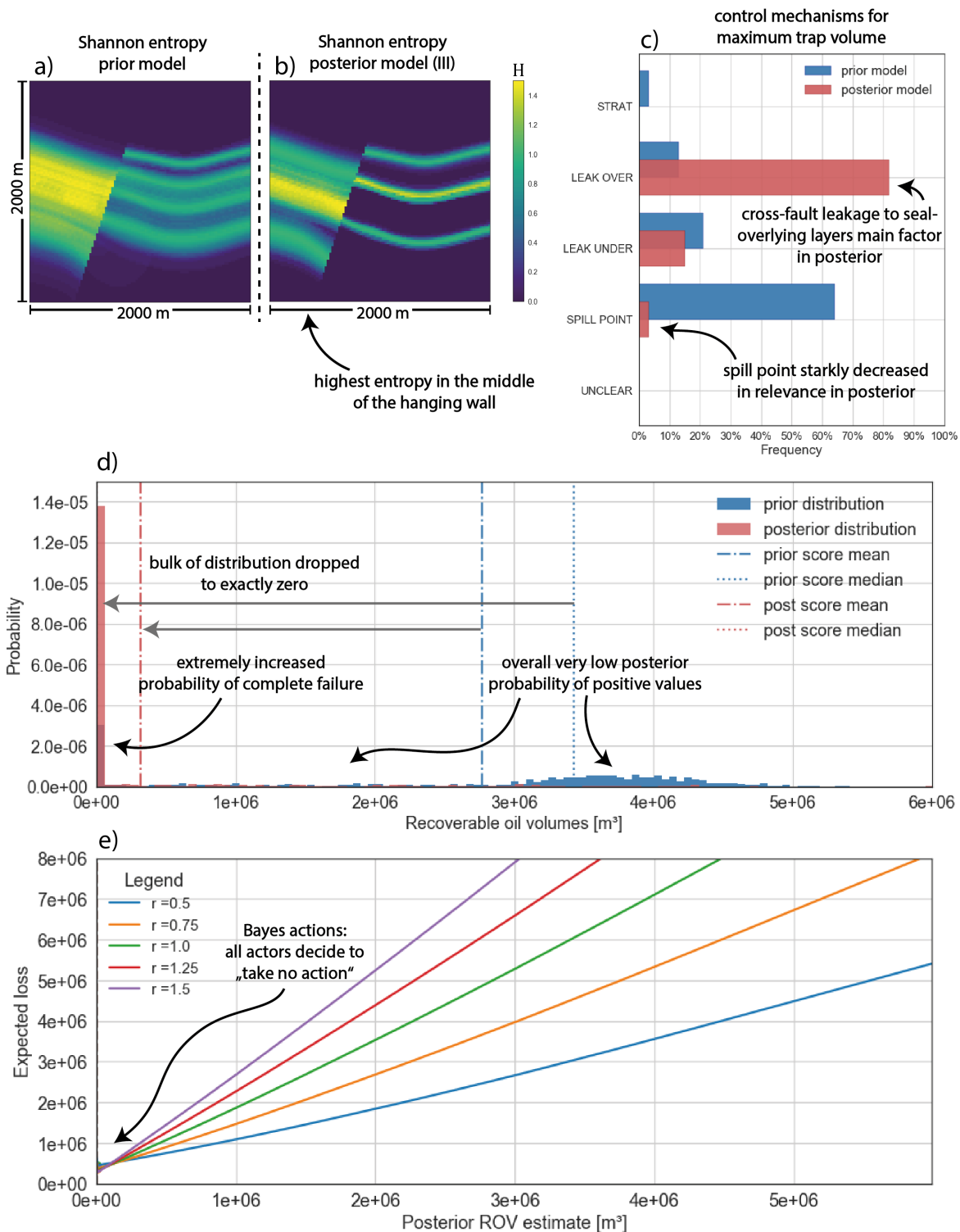


**Figure 3-9:** Summary of results from evaluating posterior model III (3D). Shannon entropies in prior (a) and posterior (b) are compared. So are the mechanisms of maximum trap volume control (c). Prior and posterior ROV probability distributions are shown in (d). Respective loss function and Bayes actions are plotted in (e).

model show that in contrast to the reservoir thickness, seal thickness is a primary and decisive factor for the manifestation of a reliable trap structure.

### 3-2-5 3D - Posterior model IV: SSF likelihood reinforcing trap reliability

Model IV - Likelihood: Layer thicknesses (normal distributions)		
Formation	$\mu$ [m]	$\sigma$ [m]
Sandstone 2	150	20
Shale (Seal)	300	30
Sandstone 1 (Reservoir)	250	25

Model IV - Likelihood: Shale Smear Factor (normal distribution)		
-	$\mu$	$\sigma$
SSF	1.5	0.5

**Table 3-6:** Layer thickness likelihoods and SSF likelihood determined by normal distributions as used for posterior model IV (3D).

For this fourth model, thickness likelihoods were chosen to be comparable to those of model I, i.e. supporting the probability of thick layers in general. Additionally, we implemented a SSF-related likelihood function. With a mean of 1.5 and a standard deviation of 0.5, it was chosen to mostly reinforce the likelihood of a SSF below the critical value of  $SSF_c = 3$  (see Table 3-6).

In Figure 3-10 (b), it can be seen that the uncertainty about the position of interfaces in the footwall was greatly reduced for all layers. In the hanging wall, Shannon entropy remained higher but was shifted upwards and mainly concentrated in an area that is juxtaposed to the footwall seal formation.

In the resulting ROV distribution, the possibility of trap failure was completely extinguished, while the probability of high volumes in the range between 3.5 and 5 million m<sup>3</sup> was significantly increased. Mean and median are found at almost the same value, but the bulk of the distribution found in this range appears to be slightly bimodal in itself, resembling approximately the shape of two normal distributions overlapping around the value of 4.3 million m<sup>3</sup>. Accordingly, Bayes actions converged within this range of positive values. Considering the two modes in this range, risk-averse to risk-neutral bids remained in the middle of the mode of lower volumes, while the risk-friendliest actor was encouraged to bid on a higher volume found in the second mode. Overall, significant convergence was achieved, also in respect to expected losses.

The importance of a safe seal was once again emphasized by these results. Reliable fault sealing was favored by the chosen SSF likelihood. It should be pointed out that computation of the complete model is required to attain the SSF. This value is furthermore characterized by a complex interdependence with other parameters and is directly related to layer thicknesses and fault offset. For this reason, Shannon entropy and offset uncertainty in the hanging wall were not reduced significantly more than without considering a SSF likelihood in posterior model I. However, we presume that the certainty about the ratio of displacement to layer thicknesses was improved by using the SSF in a likelihood function.

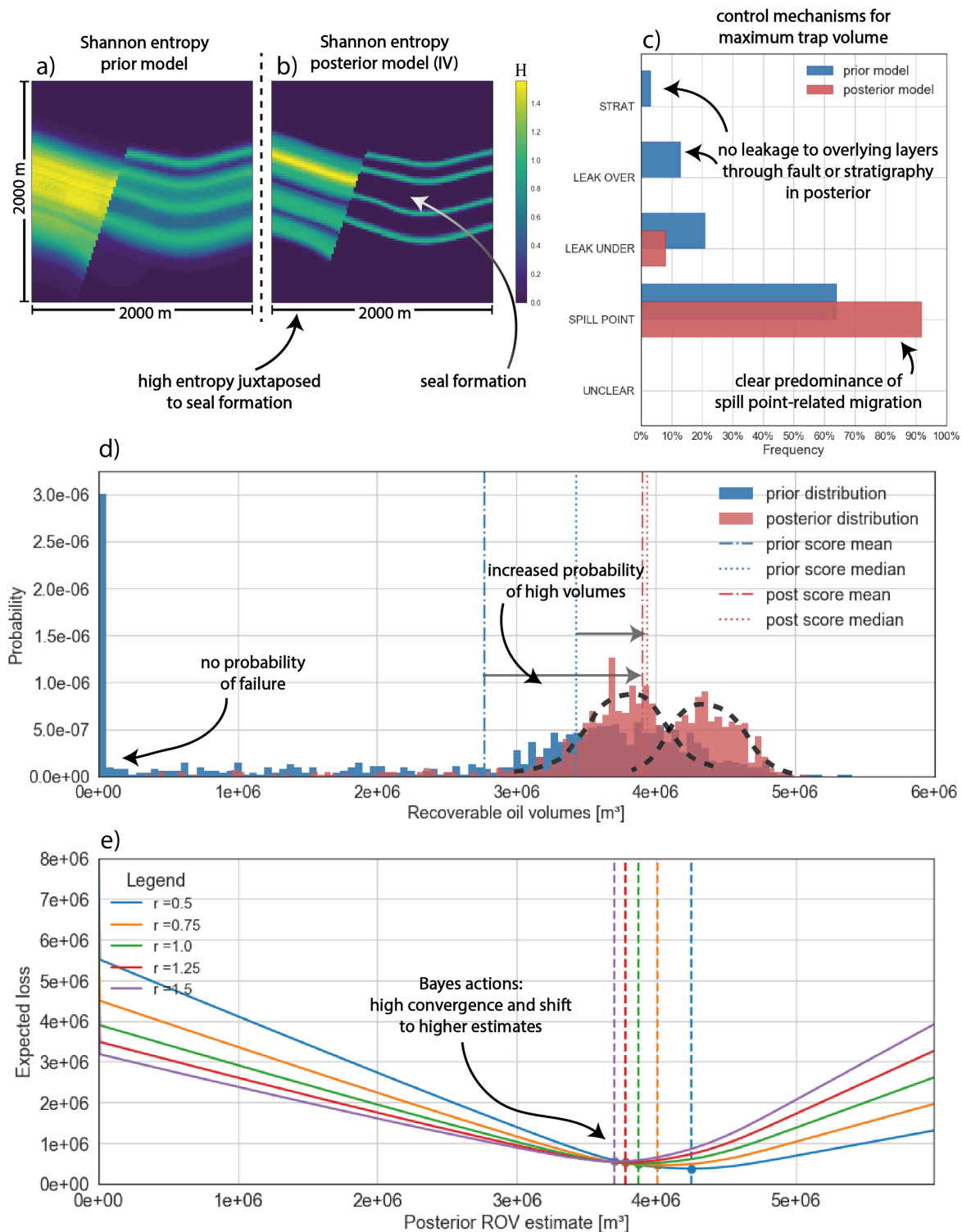


**Figure 3-10:** Summary of results from evaluating posterior model IV. Shannon entropies in prior (a) and posterior (b) are compared. So are the mechanisms of maximum trap volume control (c). Prior and posterior ROV probability distributions are shown in (d). Respective loss function and Bayes actions are plotted in (e).

### 3-2-6 3D - Posterior model V: Controversial information about the Shale Smear Factor

Model V - Likelihood: Shale Smear Factor (normal distribution)		
-	$\mu$	$\sigma$
SSF	3	0.3

**Table 3-7:** SSF likelihood determined by a normal distributions as used for posterior model V (3D).

In this last case example, no thickness likelihoods, only a SSF-related likelihood was used. In contrast to model IV, this was chosen to narrow the probability of the SSF to be around the threshold of its critical value of  $SSF_c = 3$  (see Table 3-7).

Results are relatively similar to those of the prior model. Shannon entropies were only slightly decreased overall (Figure 3-11 (b)). An increase in the relevance of cross-fault leakage to overlying formations ("LEAK OVER") as a trap volume mechanism (increase from  $\sim 13\%$  to  $\sim 18\%$ ) was observed (Figure 3-11 (c)). Consequently, the bimodal character between the bulk of positive values and the probability of complete failure in the ROV distribution was reinforced. This is also indicated by a shift of mean and median to lower volumes (Figure 3-11 (d)). Accordingly, a higher degree of decision divergence, i.e. a greater separation of different Bayes actions, was induced (Figure 3-11 (e)). Expected losses for these estimators were raised as well.

It is notable that the implementation of a likelihood function, which can be expected to significantly decrease the SSF-related uncertainty, overall leads to an amplification of the duality in the ROV probability distribution and to dispersion of differently risk-affine decisions. This effect is presumably caused by conservation of decisive uncertainty between "success" and complete failure of the trap, due to narrowing of the SSF probability around its critical value.

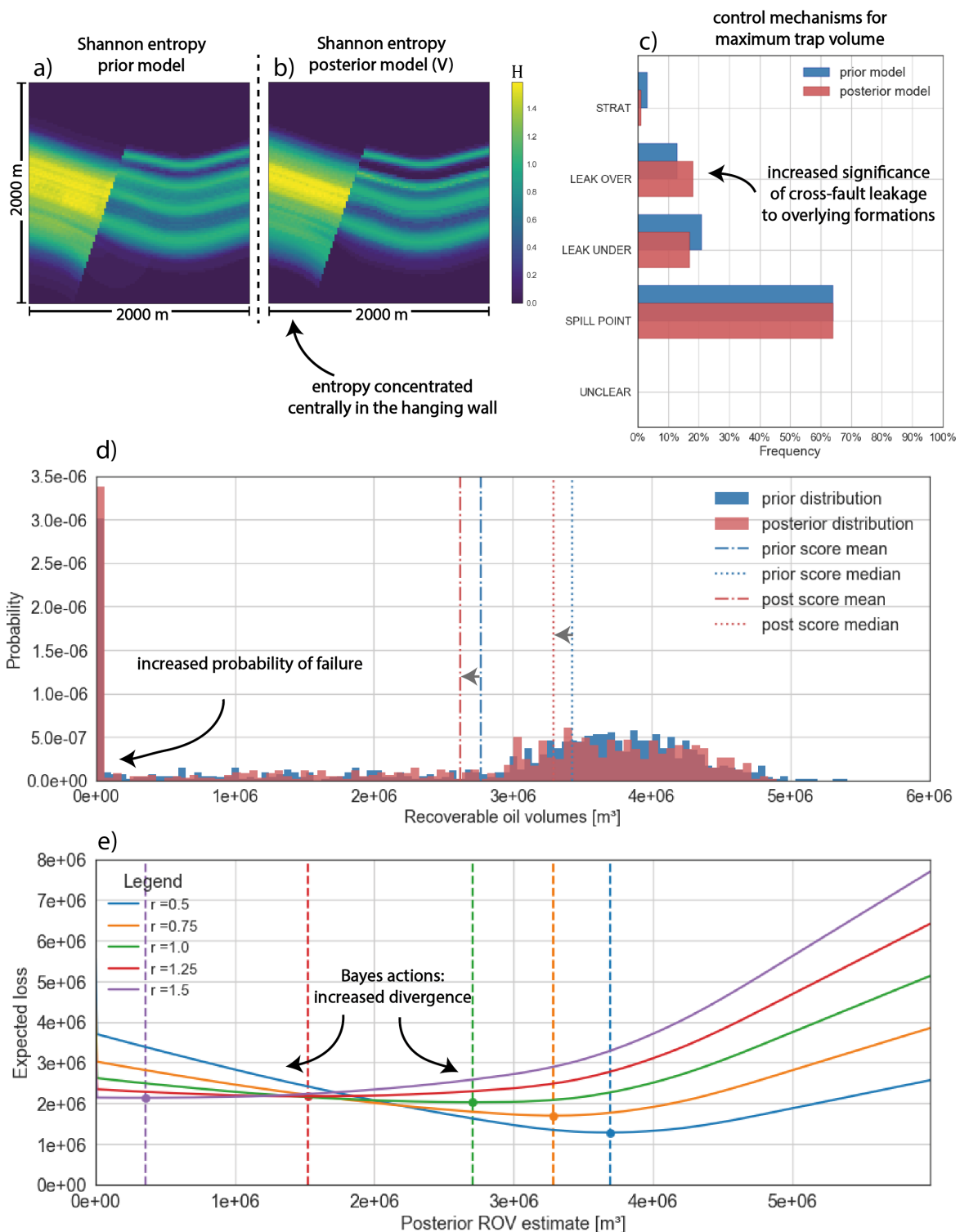


**Figure 3-11:** Summary of results from evaluating posterior model V. Shannon entropies in prior (a) and posterior (b) are compared. So are the mechanisms of maximum trap volume control (c). Prior and posterior ROV probability distributions are shown in (d). Respective loss function and Bayes actions are plotted in (e).

---

# Chapter 4

---

## Discussion

Building upon the recent findings by [De la Varga and Wellmann \(2016\)](#), the aim of this work was to extend their approach by considering practical applications and the utility structural geological modeling viewed as an Bayesian inference problem might have in an economic context. A sector in which structural geological modeling is of central importance is hydrocarbon exploration. This field is characterized by the necessity to make decisions in the face of high risks and potentially high rewards. As these decisions are often closely linked to geological modeling and the estimation of reservoir-related values, we aimed to use this context to extend the Bayesian inference step by considering its influence on respective decision making. To observe this, a case-specific loss function was developed in this work. In doing so, we intended to furthermore show that the loss function estimation approach is suitable and useful to describe varying degrees of complexities behind decision-making environments and the risk-related behavior of actors in it. To analyze this, geological models were interpreted as potential hydrocarbon systems. A central part of our work was comprised of the development of algorithms capable of automatic structural trap recognition and subsequent calculation of volumetric values relevant to decision making. Different prior and posterior probability distributions for such values were generated to form a basis for estimation via application of the custom loss function. We applied these methods first to a conceptual 1D geological model and subsequently to a full 3D structural model. Despite a significant leap in complexity, the results from both models proved to be widely similar.

### **State of knowledge, decision uncertainty and consequent decision making via loss function optimization**

The economic value realized in each model construction (score and ROV, respectively), had been defined to depend on model parameters, either directly or indirectly by taking into account their relations to other parameters or to specific thresholds and conditions. This meant, in general, that in this step of valuation, model uncertainties were in a way translated and reduced to the probability distribution of a single decisive value. As this was set to be the foundation for loss function estimation, we consider this value distribution to be an

expression of the state of knowledge on which the decision making is to be based. Thereby, we furthermore propose that the overall uncertainty inherent in this probability distribution can be referred to as "decision uncertainty" and that this entity is to be viewed separately from the model uncertainty.

By viewing decision making as a problem of optimizing a case-specific loss function based on such a state of knowledge and decision uncertainty, we were able to observe clear differences in the respective behavior of distinctly risk-affine actors. The position and separation of their Bayes actions, i.e. their decisions, manifested according to the properties of the value distributions. These were in turn determined by the proportionality regarding distribution modes, their relative probabilities and distances to each other. This was often indicated by the position of mean and median relative to these modes. A mean located in the middle between two widely separated modes, which might be of low intrinsic uncertainty themselves, would indicate a much higher overall decision uncertainty, than a mean found in the middle of a narrow unimodal distribution. Pronounced bimodality between two extremes, i.e. high overall uncertainty, resulted in a wider separation of Bayes estimators. Reduction of the distribution to one mode conversely led to the convergence of different Bayes actions. A decrease in decision uncertainty furthermore was accompanied by a reduction in expected loss for each Bayes estimator. Considering these observations, we derive that the degree of Bayes action convergence and respective expected losses, i.e. Bayes risks, can be considered measures for the state of knowledge and decision uncertainty at the moment of making a decision. The better these are, the more similar the decisions of differently risk-affine actors and the lower their loss expectations are. It can be assumed that given perfect information all actors would bid on the same estimate (the true value) and expect no loss, since no risk is present. It furthermore follows from this that the relevance of risk factors decreases with greater reduction of decision uncertainty.

### **Impact of additional information on decision making**

Cases of various states of knowledge and decision uncertainties, i.e. different realizations of the value probability distribution, were attained by the implementation of Bayesian inference. While, in most settings, adding information via inference led to a reduction of decision uncertainty, this was not always the case. We observed that the impact on decision uncertainty, induced by Bayesian inference, is not necessarily strictly aligned with the change in uncertainty regarding model parameters and their combinations. In respect to this, two aspects seems to be of central importance: (1) "where" in the model uncertainty is reduced, i.e. in which spatial area or regarding which model parameters, and (2) which possible outcome is enhanced in terms of probability. An increased probability of a thick or thin seal in our 3D model, for example, equally reduced decision uncertainty significantly, by raising the probability of a positive or negative outcome, respectively. Improved certainty about our reservoir thickness, however, had little to no impact on decision making. This shows that some areas and parameters of the model have a much greater influence on the decision uncertainty than others.

Adding to this, we observed a particular effect related to threshold values that led to an abrupt cut-off between two extrema of decision ranges. In both types of model construction, 1D and 3D, this was directly related to sealing reliability. Thresholds regarding seal thickness (1D model) and Shale Smear Factor ( $SSF_c$  in 3D model) were defined in a way that

introduced a significant possibility of complete trap failure. Consequently, it was observed that reducing the uncertainty in a way that narrowed the probability of a threshold-related parameter around its cut-off value, led to an amplification of the respective mode and thus emphasized the risk of complete failure. This can be seen in the posterior ROV distribution of 3D model V (see Figure 3-11). Resulting Bayes actions were characterized by an increase in divergence and expected losses, indicating a deterioration of the state of knowledge and an according increase in decision uncertainty. Thus, in some cases, adding information to the inference process might leave actors in greater disagreement than before.

However, we furthermore have to consider that actors weight possible outcomes of the value distribution differently. They consequently are affected differently by the same type of additional information. Risk-friendly actors were the most robust in their decision making in the face of possible trap failure. Eliminating this risk proved to be far less significant to the most risk-friendly, than for risk-averse actors. Accordingly, it should be of foremost importance for risk-averse actors to reduce the uncertainty regarding threshold-related factors which might decide between the success and complete failure of a project. This is less relevant for risk-friendly decisions makers, who respectively might acquire a comparable benefit from knowing more about the probability of positive outcomes, as they are less discouraged from overestimating and less afraid of failure. It was stated by [Bratvold and Begg \(2010\)](#) that uncertainty has two possible consequences: risk and opportunity. According to them, risk is a consequence which is subjectively undesirable to an actor, while opportunity is the opposite. In our loss function, this seems to be well represented by varying affinities to rather over- or underestimate. For risk-averse actors, a major risk is posed by seal failure. The risk-friendliest individual sees a greater risk in missing out on opportunity. Nevertheless, it is suggested by the results from the different inference cases, that the best states of knowledge are attained by eliminating multimodality and narrowing the range of probabilities to one mode anywhere along the value axis.

Crucial risks might be easily assessed, if they are dependent on only one or a few parameters, such as seal thickness in the 1D model. In other cases, they are derived from more complex parameter inter-relations, as is the case for the Shale Smear Factor, which is the ratio of displacement to seal thickness. Posterior models IV and V (see Sections 3-2-5 and 3-2-6) showed that reduced uncertainty about the SSF is not necessarily directly recognizable via Shannon entropy visualization, especially if uncertainty regarding its parent parameters remains high. It follows that, to approach an effective mitigation of high risks, the complexities behind decisive factors need to be assessed thoroughly and respective parent parameters, as well as their interdependencies, need to be identified. This might enable a better understanding of which type of information is missing and where in the model additional data might be of use for improved decision making.

A central conclusion from these observations seems to be that more of simply any type of information does not necessarily lead to better decisions. Instead, improved decision making is achieved by attaining the right kind of information that is able to shed light on uncertainties which are relevant to an individuals own goals and preferences, as well as the general problem at hand. These findings pair well with statements made by [Bratvold and Begg \(2010\)](#), who emphasized that the purpose of models in the hydrocarbon sector is to attain insights to improve decisions. In their book, they point out that value is not generated by uncertainty quantification or reduction in itself, but is created to the extent that these processes have potential to change a decision. This is reflected by our results which showed that one set of information might have a vastly different effects on a variety of Bayes estimators. New

observations might lead to a great change in decision for one actor, but be negligible for the other.

### Value distribution modes as possible model scenarios and potential decision options

Effects of adding information via Bayesian inference were reflected in changing appearances of modes in the reservoir value distributions. Considering that these changes correlated with increased or decreased relevance of specific trap control mechanisms in the 3D model, we derive that each mode represents the occurrence of a specific mechanism-related scenario. These were mostly distinctly separated with little probability in between. This presumably resulted from the assumption that traps are always "filled to spill" in respect to spill and leak point, and that full leakage is assumed for any type of seal failure, resulting in an approximate discretization into respective scenarios.

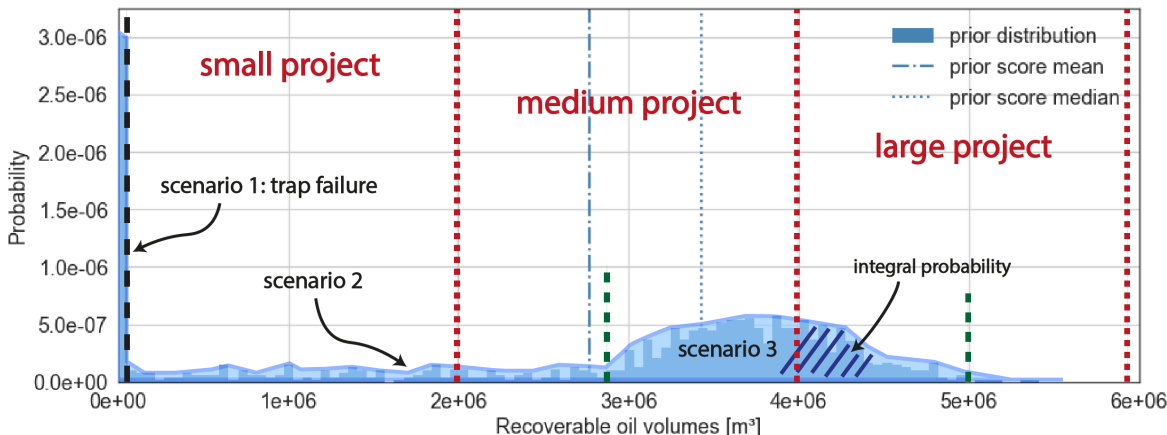


**Figure 4-1:** ROV distribution of the prior model subdivided by modes into scenarios which could pose decision options (boundaries marked by green lines). Red lines indicate a discretization of decision options according to fixed scales of resource allocations for a project. For both cases, zero equals the option to "take no action", i.e. to allocate no resources.

From a decision-making perspective, these scenarios might be interpreted as different decision options. In a case of distinct bimodality as seen in the prior of the 3D model, two main options would be given: (1) to not take any action or (2) to allocate resources according to an estimated value within the positive mode. However, most often, low probabilities for the values between these two opposite options remain. Especially considering the use of loss functions which lead to estimators located in these areas of low probability, it is debatable, how these ranges should be treated. A possibility could be to subdivide the value probability distribution accordingly into regions. Considering respective integral probabilities for each such section and by introducing a critical integral probability as a threshold, it could be determined whether such a subregion is to be considered an actual option for decision making or not. If a Bayes action is located outside of such a decision option, it could be automatically assigned to the closest region of sufficient integral probability. This approach should be easily applicable as an extension to our custom loss function. Furthermore, it could serve to build a bridge between this continuous loss function method and discrete approaches to structuring

decision problems, such as decision trees. In real cases, normally only a limited number of options is given. In the context of hydrocarbon exploration and production, this would relate to fixed magnitudes of resource allocation, such as a certain number of required drilling wells or the size of a production platform. A discretization of decision subregions in a probability distribution could thus also be based on previously defined actual options. A schematic illustration of these concepts is shown in Figure 4-1, where three predefined decision areas are labeled according to hypothetical project sizes options.

### **Comparison to common practices and research in the hydrocarbon sector**

It remains to be argued to what extent our methodology and findings contribute to practical applications in hydrocarbon exploration and production. Monte Carlo simulation for reservoir estimation and risk assessment has become common in this sector and is often used in combination with decision trees (see [Murtha et al. \(1997\)](#), [Mudford et al. \(2000\)](#), [Wim et al. \(2001\)](#) and [Bratvold and Begg \(2010\)](#)). However, it seems to us that distributions resulting from probabilistic modeling are mostly only considered to attain best estimates in the form of means. Most likely and extreme outcomes are identified as percentiles, typically P50 (the median), P10 and P90. We believe that this practice does not harness the full potential of such a probabilistic distribution and that much of the inherent information potential is discarded. Contrary to that, customized loss functions, as a Bayesian method, take into account the full probability distribution and enable the inclusion of various conditions in the process of finding an optimal estimate. While used in statistical decision theory and other scientific fields, loss functions have, to the best of our knowledge, found no significant application in the field of petroleum exploration and production. Thus, we intend to provide a new perspective with our methodology. [Murtha et al. \(1997\)](#) emphasized that Monte Carlo simulation does not make decisions. It merely prepares for it. We believe that loss functions have the potential to go one step further. A hypothetical ideal loss function would consider all conditions in an economic environment, as well as perfectly represent preferences and goals of an actor and consequently be able to automatically find an optimal decision. While this is obviously unrealistic, we presume that an elaborate loss function might at least provide a very good preliminary decision recommendation. It might furthermore be able to weight risks that are not immediately apparent to an individual as a person. Furthermore, the influence of human biases and psychological behavioral challenges, as described by [Bratvold and Begg \(2010\)](#), could be mitigated.

More recently, Bayesian inference and MCMC methods were applied for OOIP estimation and forecasting of reservoir productivity by [Wadsley et al. \(2005\)](#), [Ma et al. \(2006\)](#) and [Liu et al. \(2010\)](#). However, their research focused on history-matching simulations for already producing fields. Our approach of applying Bayesian inference for structural geological modeling and volumetric reservoir calculations is intended to support decision making in the earliest stages of a reservoir, when it has to be decided whether a project should be developed or not. Nevertheless, it was shown in the research conducted by [Wadsley et al. \(2005\)](#) that early volumetric OOIP estimates can be combined with later calculations from production data via MCMC methods. This is an area where our methods could possibly be integrated.

[Bratvold and Begg \(2010\)](#) highlighted the potential to use Monte Carlo simulation to identify, via sensitivity analysis, which uncertainties have the greatest impact on decisions. This was virtually achieved by performing several cases of Bayesian inference in our work, as we

recognized primarily the importance of seal safety.

### **Representativity and limitations of this methodology**

It has too be emphasized that the models constructed in this work were synthetic and not based on real data. Nevertheless, the 3D model in particular was designed to include some typical structural characteristics related to hydrocarbon systems. We developed algorithms aimed to consider the most common conditions that define structural traps. The fact that similar observations were made for the 1D, as well as the 3D model, indicates a certain degree of continuity with respect to representativity. However, we also need to address that the uncertainties employed in the 3D model related to  $z$ -axis positional values only and were thus of primarily one-dimensional nature. This may in part account for the parallelism to the 1D model results. Furthermore, it follows that no effective uncertainty concerning the overall structural shape was implemented, particularly regarding anticlinal features and the position of the spill point in relation to the trap top. Due to this, trap volumes tended to occur primarily in distinct scenarios. While being unrealistic, this enabled the recognition of pronounced influences related to the various control mechanisms. For computational reasons, we had to keep the number of MCMC sampling steps relatively low. For improved convergence and a higher reliability of results, more iterations should be executed. Nevertheless, we believe that for the purpose of this study, sufficient convergence and meaningful posterior results were achieved.

For a conceptual application, the customization of the loss functions was kept relatively simple. We argue that, despite its simplicity, the design of the function and the incorporation of a risk factor was suitable to achieve a clear distinction between differently risk-affine actors and respective behaviors. It would be possible to extend this design to attain very complex loss functions. As the loss function in this work was designed based on only a few basic assumptions, it might be more generally representative than a complex function that takes into account numerous very specific aspects. The consideration of more details, without a basis on real data, would have furthermore required extensive speculation, which would have presumably impaired the generalization potential of respective observations. We defined risk affinity to be dependent on arbitrarily chosen risk factors which led to according re-weighting. [Davidson-Pilon \(2015\)](#) used risk parameters determined by the maximal loss each actor could incur. Other approaches could be based on more tangible values, for example by making risk attitude dependent on a fixed budget. While standard loss functions only return mean or median as estimates, loss function customization offers a flexible approach to express different objective and subjective weighting factors that are specified to particular decision-making environments and decision makers' perspectives.

### **Possibilities for future research and extensions**

Considering the findings of this work, there is still many points that could be expanded on in future research. It would be of interest to apply the same overall concept and methodology to an authentic case based on real datasets. Given a realistic economic scenario, including capital and operational expenditures of a project, possibly a full net-present-value (NPV) analysis could be conducted. Recoverable volumes could be replaced by the NPV to evaluate modeling results and serve as a base for decision making. A more elaborate loss function

---

could be customized on the base of surveys, acquiring the specific preferences of one or several companies and thus attaining a better profile of the economic environment, as well as the individuals acting in it. Value of information (see [Eidsvik et al. \(2015\)](#)) could be considered as a parameter to better quantify the impact of Bayesian inference as observed in this work. Although the algorithms for automatic 3D hydrocarbon trap recognition were developed to fit primarily the model in this work, we presume that they could easily be adapted to other structural cases or even engineered further to be universally applicable.

Furthermore, additional and different uncertainty parameters should be considered in the future. A respective next step regarding our model would be the incorporation of uncertainties which to a wider extent affect structural shapes in all three dimensions. Otherwise, non-structural reservoir parameters could be included as uncertain values, such as porosities and permeabilities of different layers. This might be of particular interest considering factors which are part of the ROV equation or other aspects that are related to high risks in decision making.

We chose hydrocarbon systems and petroleum exploration as a sector for an exemplary application, but other settings can be found in which geological modeling is of central significance for decision making. One example would be subsurface storage of fluids in a reservoir, such as carbon capture and storage (CCS). Questions regarding storage capacity and safety deal with similar conditions and geological problems as the ones presented this work, most importantly seal reliability and the risk of leakage. In respect to this, the models and approaches in this work might provide a basis to raise new and advanced explorable cases.



---

## Bibliography

- Ahmed, T. H. and Meehan, D. N. (2011). *Advanced reservoir management and engineering*. Gulf Professional Publishing.
- Ashby, D. (2006). Bayesian statistics in medicine: a 25 year review. *Statistics in medicine*, 25(21):3589–3631.
- Ashby, D. and Smith, A. F. (2000). Evidence-based medicine as bayesian decision-making. *Statistics in medicine*, 19(23):3291–3305.
- Aug, C. (2004). *Modélisation géologique 3D et caractérisation des incertitudes par la méthode du champ de potentiel*. PhD thesis, École Nationale Supérieure des Mines de Paris.
- Barber, D. (2012). *Bayesian reasoning and machine learning*. Cambridge University Press.
- Behnel, S., Bradshaw, R., Citro, C., Dalcin, L., Seljebotn, D. S., and K, S. (2010). Cython: The best of both worlds. *Computing in Science Engineering*, 13(2).
- Ben-Gal, I. (2007). Bayesian networks. *Encyclopedia of statistics in quality and reliability*.
- Berger, J. O. (2013). *Statistical decision theory and Bayesian analysis*. Springer Science & Business Media.
- Box, G. E. and Tiao, G. C. (2011). *Bayesian inference in statistical analysis*, volume 40. John Wiley & Sons.
- Bratvold, R. and Begg, S. (2010). *Making good decisions*. Society of Petroleum Engineers.
- Calcagno, P., Chilès, J.-P., Courrioux, G., and Guillen, A. (2008). Geological modelling from field data and geological knowledge: Part i. modelling method coupling 3d potential-field interpolation and geological rules. *Physics of the Earth and Planetary Interiors*, 171(1):147–157.
- Caumon, G. (2010). Towards Stochastic Time-Varying Geological Modeling. *Mathematical Geosciences*, 42(5):555–569.

- Chilès, J.-P., Aug, C., Guillen, A., and Lees, T. (2004). Modelling the geometry of geological units and its uncertainty in 3d from structural data: the potential-field method. In *Proceedings of international symposium on orebody modelling and strategic mine planning, Perth, Australia*, volume 22, page 24.
- Collignon, M., Fernandez, N., and Kaus, B. (2015). Influence of surface processes and initial topography on lateral fold growth and fold linkage mode. *Tectonics*, 34(8):1622–1645.
- Dandekar, A. Y. (2013). *Petroleum reservoir rock and fluid properties*. CRC press.
- Davidson-Pilon, C. (2015). Bayesian methods for hackers: Probabilistic programming and bayesian inference.
- De la Varga, M. and Schaaf, A. (2017). Gempy. <https://github.com/cgre-aachen/gempy/>.
- De la Varga, M. and Wellmann, J. F. (2016). Structural geologic modeling as an inference problem: A bayesian perspective. *Interpretation*, 4(3):SM1–SM16.
- De Luca, A. and Termini, S. (1972). A definition of a nonprobabilistic entropy in the setting of fuzzy sets theory. *Information and control*, 20(4):301–312.
- Dean, L. (2007). Reservoir engineering for geologists - volumetric estimation. *The Monthly Magazine of the Canadian Society of Petroleum Geologists*, pages 11–14.
- Dolson, J. (2016a). The basics of traps, seals, reservoirs and shows. In *Understanding Oil and Gas Shows and Seals in the Search for Hydrocarbons*, pages 47–90. Springer.
- Dolson, J. (2016b). Quantifying seals and saturations: Capillary pressure, pseudo-capillary pressure and quantitative show assessment. In *Understanding Oil and Gas Shows and Seals in the Search for Hydrocarbons*, pages 233–314. Springer.
- Eidsvik, J., Mukerji, T., and Bhattacharjya, D. (2015). *Value of Information in the Earth Sciences - Integrating Spatial Modeling and Decision Analysis*. Cambridge University Press.
- Færseth, R. B. (2006). Shale smear along large faults: continuity of smear and the fault seal capacity. *Journal of the Geological Society*, 163(5):741–751.
- Gelman, A., Carlin, J. B., Stern, H. S., and Rubin, D. B. (2014). *Bayesian data analysis*, volume 2. Taylor & Francis.
- Geman, S. and Geman, D. (1984). Stochastic relaxation, gibbs distributions, and the bayesian restoration of images. *Pattern Analysis and Machine Intelligence, IEEE Transactions on*, (6):721–741.
- Geweke, J. et al. (1991). *Evaluating the accuracy of sampling-based approaches to the calculation of posterior moments*, volume 196. Federal Reserve Bank of Minneapolis, Research Department Minneapolis, MN, USA.
- Gilks, W. R. (2005). *Markov chain monte carlo*. Wiley Online Library.
- Guichard, D., Koblitz, N., and Keisler, H. J. (2013). *Calculus: Early Transcendentals*. D. Guichard.

- Haario, H., Saksman, E., and Tamminen, J. (2001). An adaptive metropolis algorithm. *bernoulli* 7 223–242. *Mathematical Reviews (MathSciNet)*: MR1828504 Digital Object Identifier: doi, 10:3318737.
- Harney, H. L. (2013). *Bayesian inference: Parameter estimation and decisions*. Springer Science & Business Media.
- Hastings, W. (1970). Monte carlo sampling methods using Markov chains and their applications. *Biometrika*, 57(1):97–109.
- Hennig, C. and Kutlukaya, M. (2007). Some thoughts about the design of loss functions. *REVSTAT - Statistical Journal*, 5(1):19–39.
- Hillier, M. J., Schetselaar, E. M., de Kemp, E. A., and Perron, G. (2014). Three-dimensional modelling of geological surfaces using generalized interpolation with radial basis functions. *Mathematical Geosciences*, 46(8):931–953.
- Hoffman, M. D. and Gelman, A. (2014). The no-u-turn sampler: Adaptively setting path lengths in hamiltonian monte carlo. *The Journal of Machine Learning Research*, 15(1):1593–1623.
- Jaynes, E. T. (1986). Bayesian methods: General background.
- Jaynes, E. T. (2003). *Probability theory: The logic of science*. Cambridge university press.
- Jessell, M. W., Ailleres, L., and De Kemp, E. A. (2010). Towards an integrated inversion of geoscientific data: What price of geology? *Tectonophysics*, 490(3):294–306.
- Koller, D. and Friedman, N. (2009). *Probabilistic graphical models: principles and techniques*. MIT press.
- Kuijper, A. (2004). On detecting all saddle points in 2d images. *Pattern Recognition Letters*, 25(15):1665–1672.
- Labastie, A. (2011). En route: Increasing recovery factors: A necessity.
- Lajaunie, C., Courrioux, G., and Manuel, L. (1997). Foliation fields and 3d cartography in geology: principles of a method based on potential interpolation. *Mathematical Geology*, 29(4):571–584.
- Langtangen, P. H. (2008). *Python scripting for computational science*. Springer Verlag, New York.
- Lindsay, N., Murphy, F., Walsh, J., and Watterson, J. (1993). Outcrop studies of shale smears on fault surfaces. *The Geological Modelling of Hydrocarbon Reservoirs and Outcrop Analogues*, pages 113–123.
- Liu, C., McVay, D. A., et al. (2010). Continuous reservoir-simulation-model updating and forecasting improves uncertainty quantification. *SPE Reservoir Evaluation & Engineering*, 13(04):626–637.

- Ma, X., Al-Harbi, M., Datta-Gupta, A., Efendiev, Y., et al. (2006). A multistage sampling method for rapid quantification of uncertainty in history matching geological models. In *SPE Annual Technical Conference and Exhibition*. Society of Petroleum Engineers.
- MacKay, D. J. (2003). *Information theory, inference and learning algorithms*. Cambridge university press.
- Mallet, J.-L. (1992). Discrete smooth interpolation in geometric modelling. *Computer-aided design*, 24(4):178–191.
- Mann, J. C. (1993). Uncertainty in geology. In *Computers in geology—25 years of progress*, pages 241–254. Oxford University Press, Inc.
- Metropolis, N., Rosenbluth, A. W., Rosenbluth, M. N., Teller, A. H., and Teller, E. (1953). Equation of state calculations by fast computing machines. *The journal of chemical physics*, 21(6):1087–1092.
- Morton-Thompson, D., Woods, A. M., et al. (1993). *Development Geology Reference Manual: AAPG Methods in Exploration Series, No. 10*. Number 10. AAPG.
- Mosegaard, K., Tarantola, A., et al. (2002). Probabilistic approach to inverse problems. *International Geophysics Series*, 81(A):237–268.
- Moyé, L. A. (2006). *Statistical reasoning in medicine: the intuitive P-value primer*. Springer Science & Business Media.
- Mudford, B. et al. (2000). Valuing and comparing oil and gas opportunities: A comparison of decision tree and simulation methodologies. In *SPE Annual Technical Conference and Exhibition*. Society of Petroleum Engineers.
- Murtha, J. A. et al. (1997). Monte carlo simulation: its status and future. *Journal of Petroleum Technology*, 49(04):361–373.
- North, F. (1985). *Petroleum Geology*. Springer Netherlands.
- Patil, A., Huard, D., and Fonnesbeck, C. J. (2010). PyMC: Bayesian stochastic modelling in python. *Journal of statistical software*, 35(4):1.
- Salvatier, J., Wiecki, T. V., and Fonnesbeck, C. (2016). Probabilistic programming in python using pymc3. *PeerJ Computer Science*, 55(2).
- Sambridge, M. and Mosegaard, K. (2002). Monte carlo methods in geophysical inverse problems. *Reviews of Geophysics*, 40(3).
- Schaaf, A. (2017). Geological inference based on kinematic structural models. Master's thesis, RWTH AACHEN UNIVERSITY, Aachen, Germany.
- Schmatz, J., Vrolijk, P., and Urai, J. (2010). Clay smear in normal fault zones—the effect of multilayers and clay cementation in water-saturated model experiments. *Journal of Structural Geology*, 32(11):1834–1849.
- Selley, R. C. and Sonnenberg, S. A. (2014). *Elements of petroleum geology*. Academic Press.

- Shannon, C. E. (1948). A mathematical theory of communication, part i, part ii. *Bell Syst. Tech. J.*, 27:623–656.
- Sorkhabi, R. and Tsuji, Y. (2005). The place of faults in petroleum traps.
- Tarantola, A. and Valette, B. (1982). Inverse problems= quest for information. *J. geophys.*, 50(3):150–170.
- Theodoridis, S. (2015). *Machine learning: a Bayesian and optimization perspective*. Academic Press.
- van der Zee, W. and Urai, J. L. (2005). Processes of normal fault evolution in a siliciclastic sequence: a case study from miri, sarawak, malaysian. *Journal of Structural Geology*, 27(12):2281–2300.
- van der Zee, W., Urai, J. L., and Richard, P. D. (2003). Lateral clay injection into normal faults. *GEOARABIA-MANAMA-*, 8:501–522.
- Verschelde, J. (2017). Programming tools and file management - part i: A tour of python. <http://homepages.math.uic.edu/~jan/mcs275/mcs275notes/index.html>. Last visited on 18/10/2017.
- Vrolijk, P. J., Urai, J. L., and Kettermann, M. (2016). Clay smear: Review of mechanisms and applications. *Journal of Structural Geology*, 86:95–152.
- Wadsley, A. W. et al. (2005). Markov chain monte carlo methods for reserves estimation. In *International Petroleum Technology Conference*. International Petroleum Technology Conference.
- Wald, A. (1950). Statistical decision functions.
- Weisstein, E. W. (2017). Saddle point. from mathworld—a wolfram web resource. <http://mathworld.wolfram.com/SaddlePoint.html>. Last visited on 18/10/2017.
- Wellmann, J. F., De la Varga, M., Murdie, R. E., Gessner, K., and Jessell, M. (2017). Uncertainty estimation for a geological model of the sandstone greenstone belt, western australia insights from integrated geological and geophysical inversion in a bayesian inference framework. In Gessner, K., Glessinkop, T. G., and Sorjonen-Ward, P., editors, *Characterization of Ore-Forming Systems from Geological, Geochemical and Geophysical Studies*. Geological Society, London, Special Publications, 453.
- Wellmann, J. F., Horowitz, F. G., Schill, E., and Regenauer-Lieb, K. (2010). Towards incorporating uncertainty of structural data in 3d geological inversion. *Tectonophysics*, 490(3):141–151.
- Wellmann, J. F. and Regenauer-Lieb, K. (2012). Uncertainties have a meaning: Information entropy as a quality measure for 3-d geological models. *Tectonophysics*, 526:207–216.
- Wim, J., Swinkels, H., et al. (2001). Guidelines for the evaluation of petroleum reserves and resources. *Society of Petroleum Engineers*.
- Yielding, G. (2012). Using probabilistic shale smear modelling to relate sgr predictions of column height to fault-zone heterogeneity. *Petroleum Geoscience*, 18(1):33–42.

Yielding, G., Freeman, B., and Needham, D. T. (1997). Quantitative fault seal prediction. *AAPG bulletin*, 81(6):897–917.

Zadeh, L. A. (1965). Fuzzy sets. *Information and control*, 8(3):338–353.

---

## Appendix A

---

# Appendix

### A-1 Code availability

GemPy and PyMC are both fully open source and to be used in a Python environment. At the time of writing this, GemPy is still under development (version 0.997). It can be obtained from <https://github.com/cgre-aachen/gempy>. PyMC can be downloaded from <https://github.com/pymc-devs/pymc> (PyMC2) and <https://github.com/pymc-devs/pymc3> (PyMC3).

The models, algorithms and functions developed and presented in this work are accessible as IPython Notebooks on github: <https://github.com/nre-aachen/Theses/tree/master/Riskanalysis>.

## A-2 Additional tables and figures

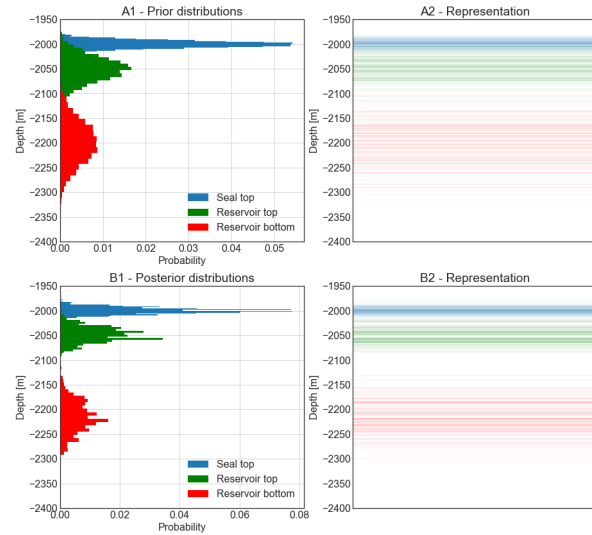


**Figure A-1:** Prior (A1) and posterior distributions (B1) of the layer boundary positions in depth and respective representations (A2, B2) for 1D inference case II.

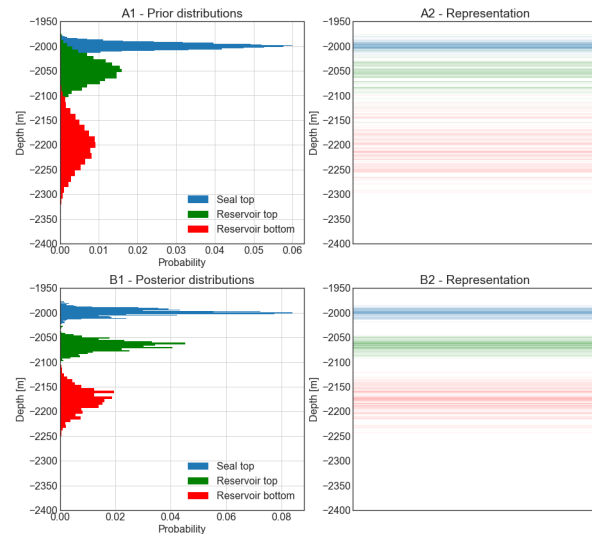


**Figure A-2:** Prior (A1) and posterior distributions (B1) of the layer boundary positions in depth and respective representations (A2, B2) for 1D inference case III.

**Interface positional information**

X	Y	Z	formation
800	50	750	Res_Top
800	150	700	Res_Top
800	300	700	Res_Top
800	500	800	Res_Top
800	1000	1000	Res_Top
800	1500	700	Res_Top
800	1700	600	Res_Top
800	1950	650	Res_Top
0	1000	1100	Res_Top
300	1000	1000	Res_Top
450	1000	950	Res_Top
1100	1000	900	Res_Top
1400	1000	850	Res_Top
1700	1000	900	Res_Top
1500	500	800	Res_Top
1500	1500	750	Res_Top
800	50	450	Base_Top
800	150	400	Base_Top
800	300	400	Base_Top
800	500	500	Base_Top
800	1000	700	Base_Top
800	1500	400	Base_Top
800	1700	300	Base_Top
800	1950	350	Base_Top
0	1000	800	Base_Top
300	1000	700	Base_Top
1100	1000	600	Base_Top
1400	1000	550	Base_Top
1700	1000	600	Base_Top
1500	500	500	Base_Top
1500	1500	450	Base_Top

**Figure A-3:** 3D model construction input data (1): point-positional values for layer interfaces and the fault surface.

### Interface positional information

X	Y	Z	formation
900	150	920	Seal_Top
900	300	920	Seal_Top
900	1500	920	Seal_Top
900	1700	820	Seal_Top
900	1950	870	Seal_Top
0	1000	1300	Seal_Top
300	1000	1200	Seal_Top
600	1000	1100	Seal_Top
1100	1000	1100	Seal_Top
1400	1000	1050	Seal_Top
1700	1000	1100	Seal_Top
1500	500	1000	Seal_Top
1500	1500	950	Seal_Top
0	1000	1500	SecRes_Top
300	1000	1400	SecRes_Top
600	1000	1300	SecRes_Top
1100	1000	1300	SecRes_Top
1400	1000	1250	SecRes_Top
1700	1000	1300	SecRes_Top
1500	500	1200	SecRes_Top
1500	1500	1150	SecRes_Top
700	1000	900	MainFault
600	1000	600	MainFault
500	1000	300	MainFault
800	1000	1200	MainFault
900	1000	1500	MainFault

**Figure A-4:** 3D model construction input data (2): point-positional values for layer interfaces and the fault surface.

### Interface dip information

X	Y	Z	azimuth	dip	polarity	formation
1000	1000	950	90	18,435		1 Res_Top
400	1000	1400	90	18,435		1 SecRes_Top
500	1000	864,602	270	71,565		1 MainFault

**Figure A-5:** 3D model construction input data (3): dip-related values for layer interfaces and the fault surface.

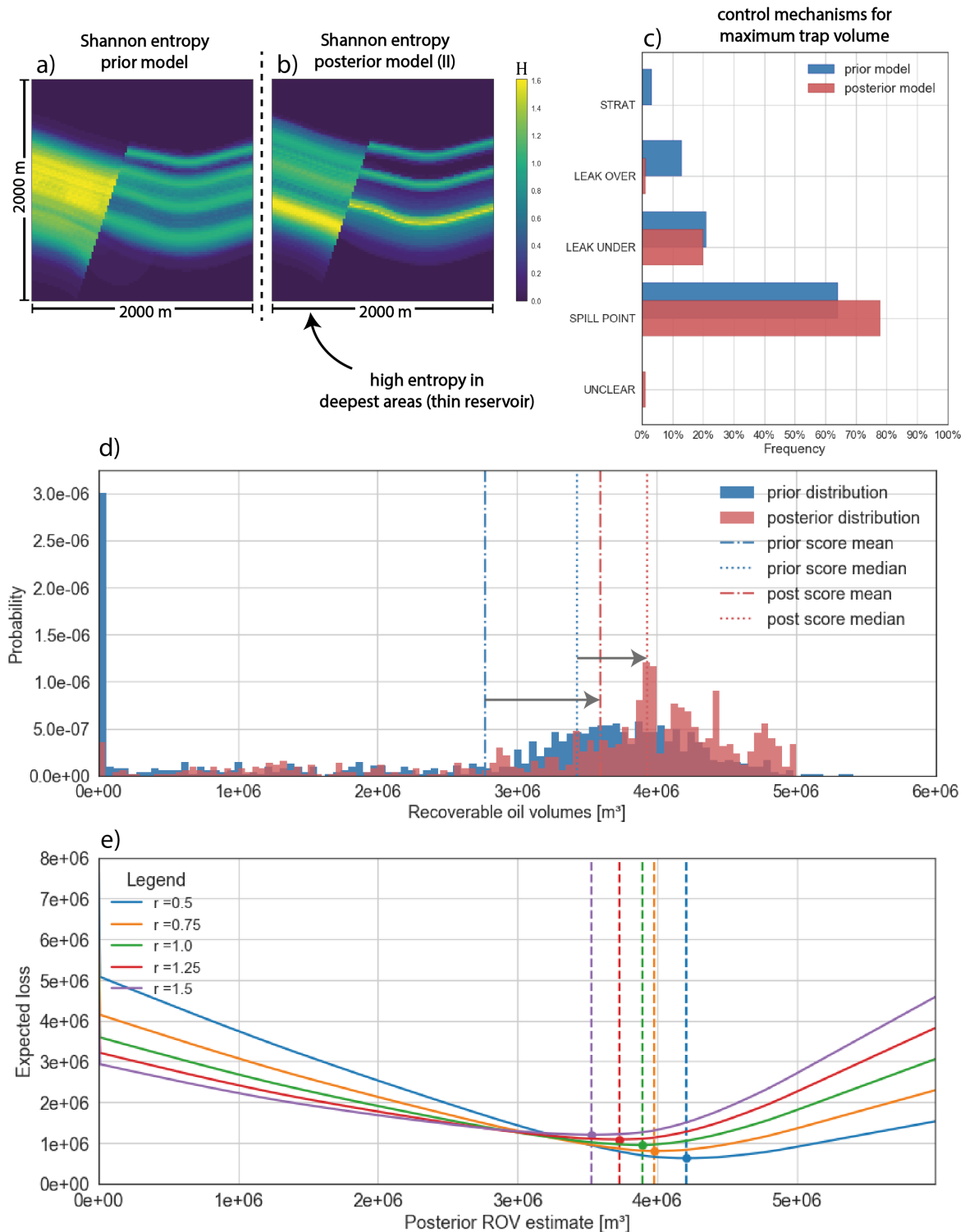
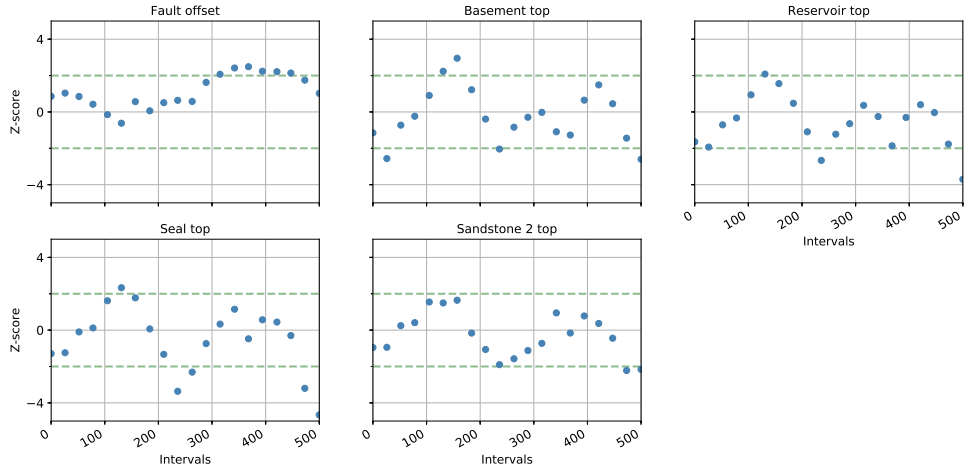
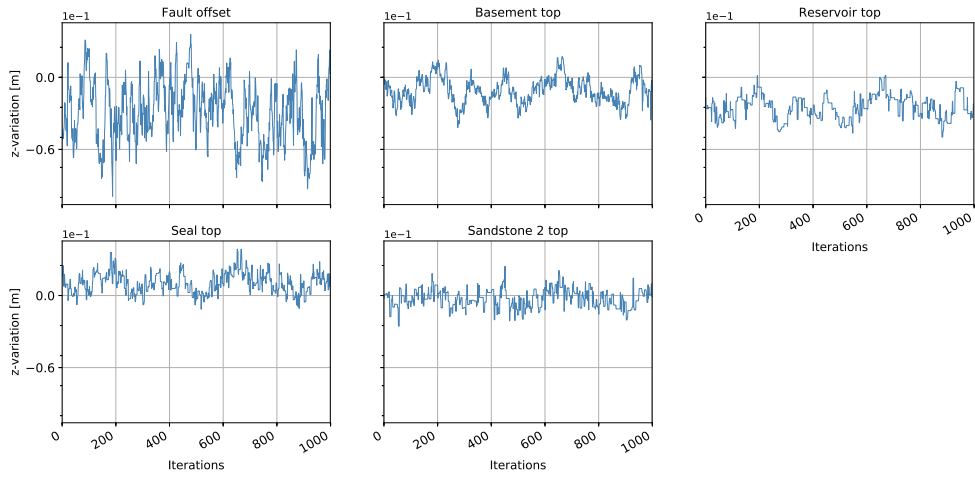


**Figure A-6:** Summary of results from evaluating posterior model II (3D). Shannon entropies in prior (a) and posterior (b) are compared. So are the mechanisms of maximum trap volume control (c). Prior and posterior ROV probability distributions are shown in (d). Respective loss function and Bayes actions are plotted in (e).

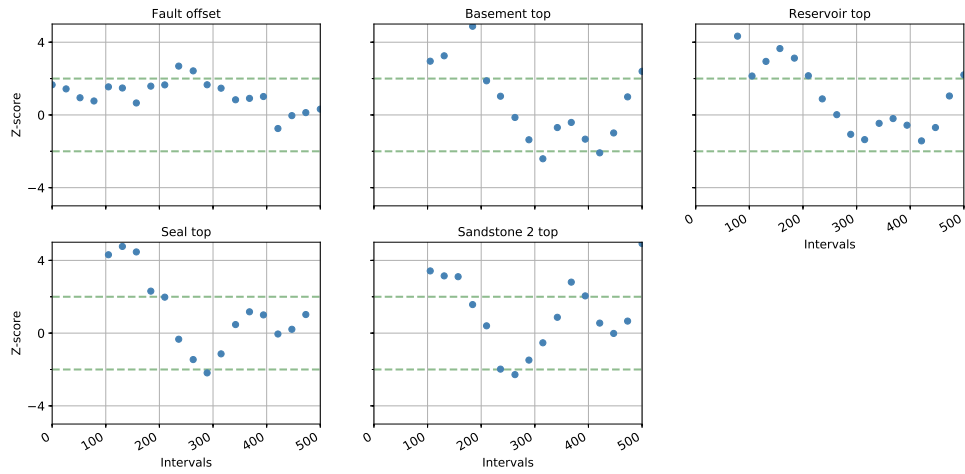


(a) Geweke plots for uncertain priors.

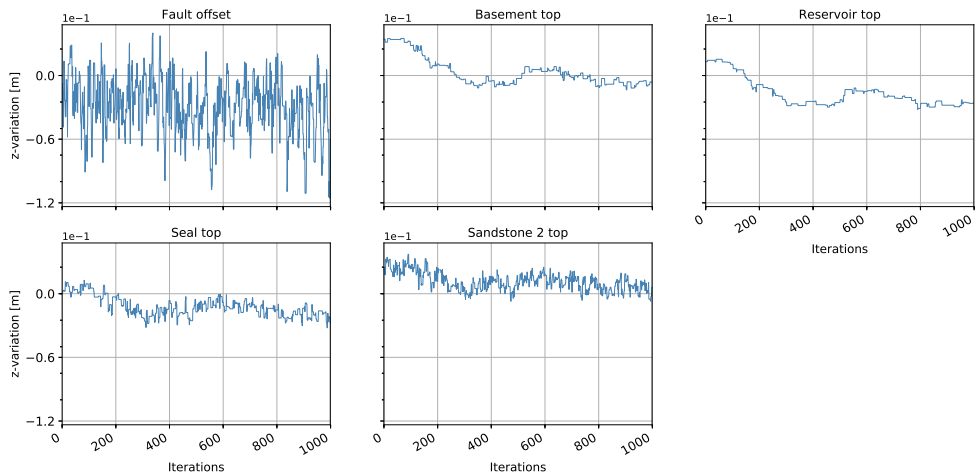


(b) Traces for uncertain priors.

**Figure A-7:** 3D posterior model I: Geweke convergence analysis (a) and plotted traces (b) for uncertain priors. In (a), the standard deviation between the mean value of one trace interval and the following is represented by the Z-score. Scores in the range between -2 and 2 indicate convergence of the MCMC sampling process.

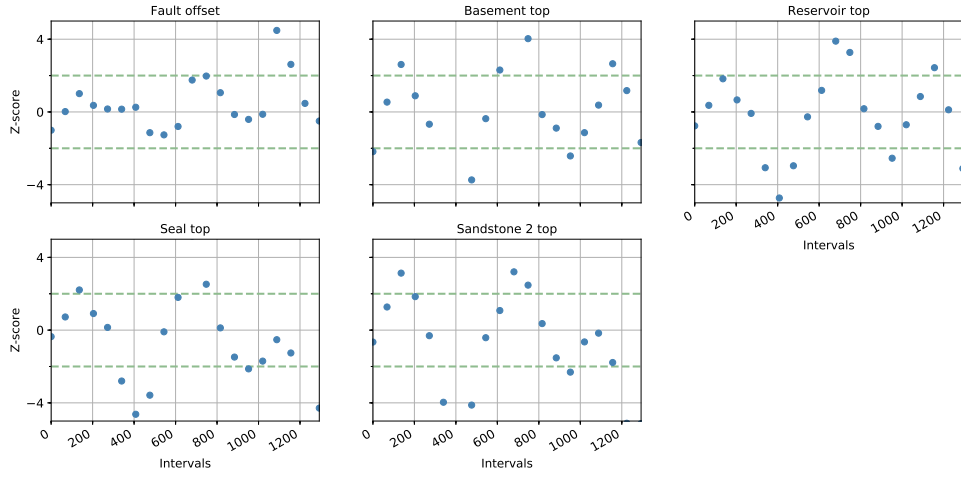


(a) Geweke plots for uncertain priors.

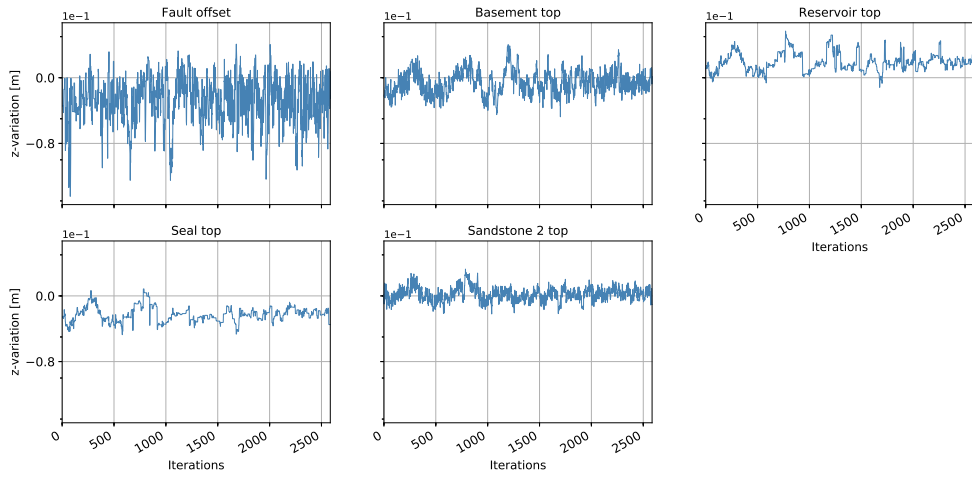


(b) Traces for uncertain priors.

**Figure A-8:** 3D posterior model II: Geweke convergence analysis (a) and plotted traces (b) for uncertain priors. In (a), the standard deviation between the mean value of one trace interval and the following is represented by the Z-score. Scores in the range between -2 and 2 indicate convergence of the MCMC sampling process.

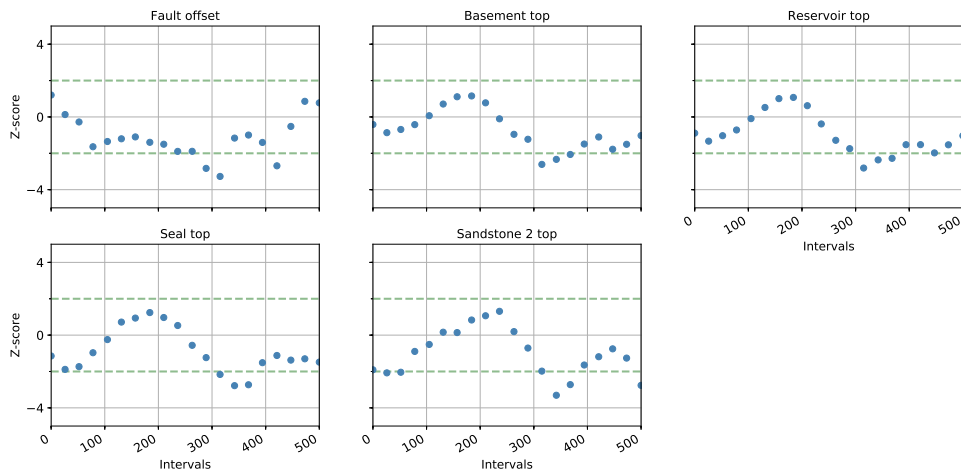


(a) Geweke plots for uncertain priors.

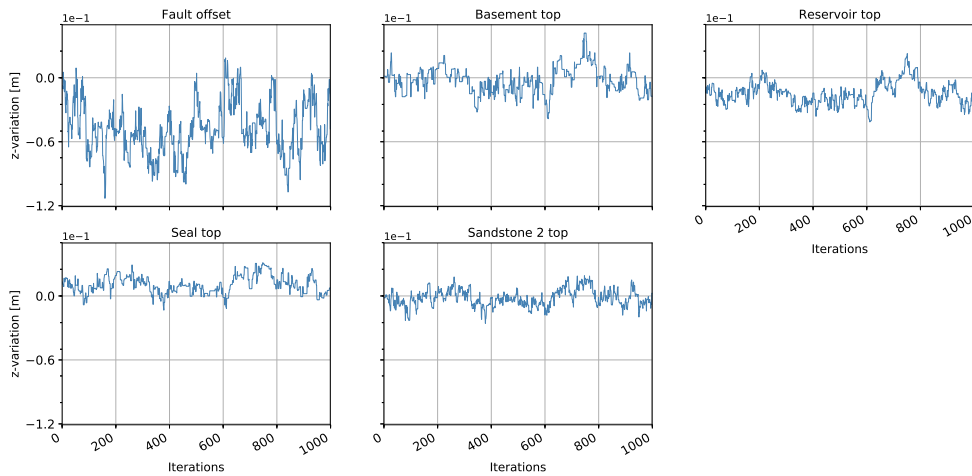


(b) Traces for uncertain priors.

**Figure A-9:** 3D posterior model III: Geweke convergence analysis (a) and plotted traces (b) for uncertain priors. In (a), the standard deviation between the mean value of one trace interval and the following is represented by the Z-score. Scores in the range between -2 and 2 indicate convergence of the MCMC sampling process.

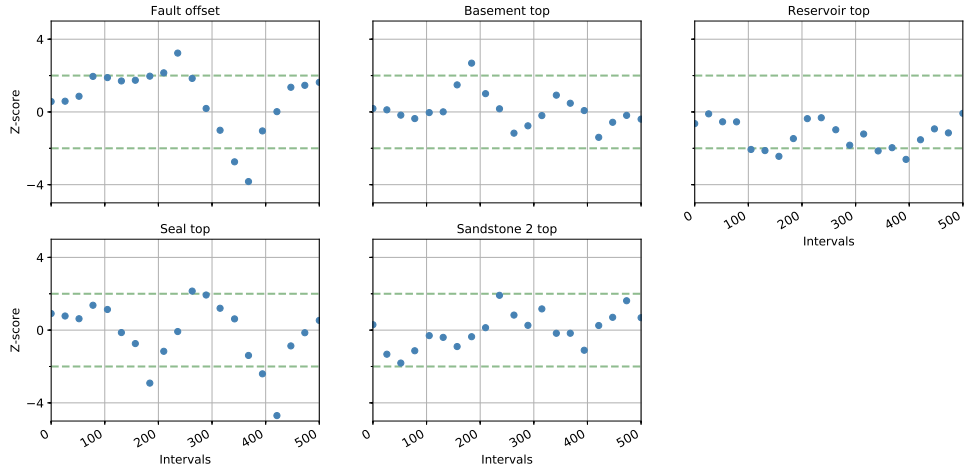


(a) Geweke plots for uncertain priors.

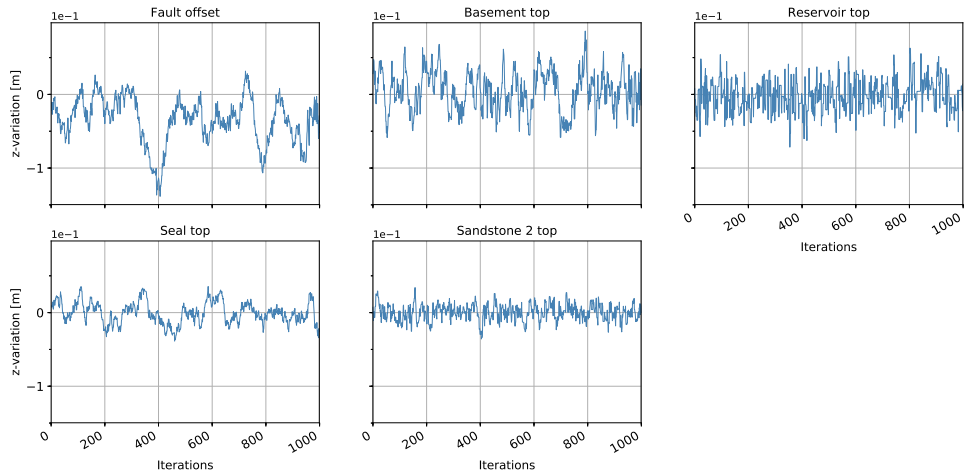


(b) Traces for uncertain priors.

**Figure A-10:** 3D posterior model IV: Geweke convergence analysis (a) and plotted traces (b) for uncertain priors. In (a), the standard deviation between the mean value of one trace interval and the following is represented by the Z-score. Scores in the range between -2 and 2 indicate convergence of the MCMC sampling process.



(a) Geweke plots for uncertain priors.



(b) Traces for uncertain priors.

**Figure A-11:** 3D posterior model V: Geweke convergence analysis (a) and plotted traces (b) for uncertain priors. In (a), the standard deviation between the mean value of one trace interval and the following is represented by the Z-score. Scores in the range between -2 and 2 indicate convergence of the MCMC sampling process.